Ureilite Meteorites and the Unknown Proto-Planet

Using EBSD to construct a geological history.

Image showing two planets colliding and being destroyed. © [Ameer] / Adobe Stock

Hayley Lowe

Supervised by Dr Luke Daly and Prof. Martin Lee

Abstract:

The ureilites are a group of ultramafic achondrite meteorites composed primarily of olivine and pigeonite, with accessory minerals and a high abundance of carbon in the form of graphite and diamond. There are many hypotheses as to how the ureilite group formed, but the majority of authors are now in agreement that they represent a mantle restite of a now destroyed planetesimal that may have been as large as Mercury (Nabiei et al., 2018). This planetesimal was large enough for the ureilites to form through igneous processing, but not large enough to become a full planet. At some point, possibly within the first 10 million years (Rai et al., 2020) of its life the ureilite parent body (UPB) was subjected to a catastrophic impact which destroyed the planetesimal and created daughter asteroids which are the current parent bodies of the ureilites (Goodrich et al., 2015). This study aims to construct a comprehensive geological history of the samples using Electron Backscatter Diffraction (EBSD), Energy Dispersive Spectroscopy (EDS), Raman spectroscopy and geochemical data. Here we show using Raman peak Full Width Half Maximum (FWHM) data that the majority of diamonds present in the ureilite suite are formed through shock related processes. This is combined with the EBSD data and optical microscopy data to discuss a range of shock features present within the ureilites such as mosaicism. Various slip systems are shown to be activated across the samples indicating deformation occurred during a variety of temperature and pressure conditions throughout ureilite formation. Evidence of shear processes affecting the majority of the samples studied is also presented using the EBSD datasets. A proposed geological history is presented to tie shock and shear features together. Our results agree with recent studies about diamond formation (Nestola et al., 2020) on the UPB which goes some way to negating the need for a large planetesimal to be required in order to explain ureilite formation.

Table of Contents

1.Introduction:

Planetary science involves the study of how the Solar System was formed from the original Solar nebula, and how this led to planetary formation. The Solar System is composed of the Sun in the centre; four rocky planets; the Asteroid Belt; two gas giants; two icy giants; and the Kuiper Belt along with hundreds of Moons. The exact number of Moons changes regularly due to new discoveries and classifications happening all the time, but it is currently over 180 (Rauf et al., 2015). The only extra-terrestrial body visited by humans is the Moon during the Apollo missions in the 1960s/1970s (Ringwood and Essene, 1970) and material was returned to Earth for study. Sample return missions so far have successfully collected and returned material from two asteroids, Itokawa (Tsuchiyama et al., 2011) and Ryugu (Okazaki et al., 2017) with a third currently en-route back to Earth with samples from Bennu (Lauretta et al., 2017). The Stardust mission has also returned dust samples from the comet Wild 2 (Brownlee, 2014, 2003).This means material from direct sampling across the Solar System is limited. Thus, in order to answer questions about Solar System evolution and planetary formation additional extraterrestrial samples are required. This is where meteorites are useful: they sample a much wider range of planetary materials from a variety of parent bodies and have the benefit of coming to Earth instead of humans having to go and get them.

Meteorites are defined as solid bodies that have fallen from space through the Earth's atmosphere and come to land at the surface (Rubin and Grossman, 2010). In the current era of space exploration and man-made orbiters the definition has been expanded to include samples that have fallen from space onto other bodies, such as chondritic material found on the Moon which is also described as a meteorite despite not falling through Earth's atmosphere (Rubin and Grossman, 2010). The definition also excludes any man-made material that has fallen back down to Earth after being placed in orbit (Rubin and Grossman, 2010). The planetary body from which a meteorite sample originated is called the parent body. A parent body could be another planet, such as Mars, asteroids (for example Vesta), or from the Moon. The asteroid belt is littered with remnant planetary cores and undifferentiated planetesimals from the early Solar System. During the first billion years after formation (~4.5-3.5 Ga) the Solar System was a significantly more violent place where many early planetesimals were disrupted or destroyed or could not accrete further mass required to become a planet due to large planetesimal-planetesimal collisions (Gomes et al., 2005; Bottke and Norman, 2017). Some meteorites sample the oldest material in the Solar System as well as both the interior and exterior of parent bodies, planetesimals and planets and have remained relatively unaltered since (Lipschutz and Schultz, 2014). Due to their early formation and minimal alteration, meteorites are one of the best sources of information about this early violent period of the Solar Systems development. The parent bodies range from being fully differentiated planets, e.g. Mars, to much smaller undifferentiated (Lipschutz and Schultz, 2014). A single planetesimal is theorized to be the parent body of the ureilite group of meteorites, which are the focus of this thesis.

Meteorites can be categorised based on their geochemical, mineralogical, and textural characteristics. The main groups of meteorites are the iron, stony iron, and stony meteorites. Iron meteorites are composed of Fe-Ni alloys such as kamacite and taenite (Yang et al., 2007), and are further classified based on the presence of any accessory minerals and Ga/Ge content (Rubin, 1997; Scott & Wasson, 1975). They are considered to represent the metallic cores of differentiated planets and planetesimals (Scott and Wasson, 1975). Differentiation occurs when a planetesimal is hot enough to partially melt (at least > 40% (Taylor, 1992))

causing the dense metallic elements to sink to the interior of the planet with the lighter silicates remaining closer to the surface, forming a core, mantle, and crust. Studies of the cooling rates of various groups of iron meteorites suggest the parent bodies were between 5-300 km diameter (Yang et al., 2007). Studying iron meteorites is currently the only way to directly study a planetary core. These metallic asteroids are the focus of future space missions such as Psyche due to the information they may contain about how planets grow, differentiate out into layers, and collide/disrupt (Moura et al., 2019).

1.1 Stony iron meteorites

Stony iron meteorites (e.g. pallasites) contain olivine crystals within an iron-nickel matrix (Bryson et al., 2015). These meteorites were once thought to form at the core-mantle boundary of differentiated bodies (Tarduno et al., 2012). However, studies of the magnetisation of pallasites have shown that their parent body hosted a dynamo, which requires a partially molten outer core in order to generate such dynamo (Tarduno et al., 2012). The same study noted that the pallasites record evidence of a dynamo after the injection of metal into the olivine crystals leaving inclusions which cooled below the Curie temperature of taenite around ~360 °C (Tarduno et al., 2012). A dynamo affecting the pallasites whilst they were this cool would mean they could not have been close to a molten outer core, and instead the metal-silicate composition is interpreted to record a collision between a differentiated proto-planet and a remnant iron core from a previously destroyed proto-planet (Tarduno et al., 2012). Stony-iron meteorites can be very beneficial to studying planetary scale collisions, as they may record some very early large collisions between differentiating planets and iron rich cores.

1.2 Stony meteorites

Stony meteorites are composed predominantly of of silicate minerals with variable amounts of metal. Stony meteorites can be subdivided further into chondrites, and achondrites. A classification diagram is shown in fig.1.

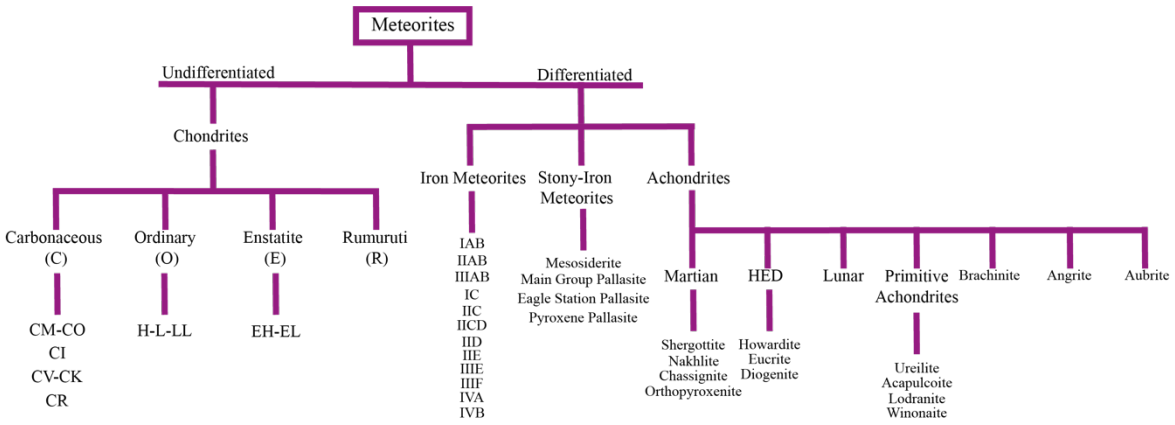

Figure 1: Classification diagram of stony meteorites. Adapted from NASA. (https://curator.jsc.nasa.gov/education/classification.cfm accessed 19/12/22 using information from (Weisberg et al., 2006))

1.2.1 Chondrites

1.2.1.1 Chondrite overview

Chondrites represent the majority of all meteorite falls and finds and are some of the oldest material in the Solar System, forming within the first 5-15 Ma of Solar System history (Scott & Krot, 2007). They are ultramafic and contain chondrules embedded in a fine grained matrix. Chondrules are spherical olivine and pyroxene that was once molten and cooled very rapidly (Scott & Krot, 2007). They also contains calcium- and aluminium-rich inclusions (CAIs) and pre-solar grains. Chondrites have survived relatively unaltered since their formation, and some have experienced almost no alteration, they are classified as undifferentiated meteorites in fig 1. However some chondrites have been altered through fluids or thermal processes, which is measured on a petrographic scale 1-6. On this scale 3 is unaltered, 4-6 represents increasing thermal alteration whereas 2-1 is increasing aqueous alteration (van Schmus and Wood, 1967). Chondrites are further separated into ordinary, enstatite and carbonaceous chondrites, shown in fig 1. At the time of formation for the primitive meteorites, including chondrites, the solar nebula was heterogeneous with respect to O isotopes (Clayton et al., 1991). This allows for the groups to be distinguished from each other using their distinct oxygen isotope ratios. Carbonaceous and non-carbonaceous chondrites sample two distinct oxygen isotopic reservoirs known from bulk O-isotope measurements (Krot, 2019). One proposed theory to explain this dichotomy is due to the early formation of Jupiter during evolution of the Solar System. This theory suggests proto-Jupiter cleared out a region of the proto-planetary disk whilst the planet was accreting, and this gap separated the two reservoirs so carbonaceous and non-carbonaceous formed separately in separate regions of the early Solar System (Krot, 2019). Carbonaceous chondrites are thought to have formed in the outer Solar System beyond Jupiter, and non carbonaceous chondrites formed in the inner Solar System (Krot, 2019).

Chondrites are useful meteorites to study as they contain a wealth of information about the solar nebula and initial stages of the Solar System formation. Carbonaceous chondrites in particular are studied as a possible mechanism for delivering water and organic compounds to Earth (Glavin et al., 2010).

1.2.1.2 Ordinary Chondrites

Ordinary chondrites are the most common type of meteorite (Nesvorný et al., 2009). This group is subdivided into H (high Fe), L (low Fe) and LL (low Fe and low metal) groups (Nesvorný et al., 2009).

1.2.1.3 Carbonaceous Chondrites

Carbonaceous chondrites are subdivided into a variety of groups (shown in fig. 1). Carbonaceous chondrites are much darker in colour than ordinary chondrites, and have little to no native iron (Mason, 1963). Carbonaceous chondrites are identified due to the appreciable amount of free carbon, that is carbon not contained in graphite or diamond, which can be as high as 3.5wt% (Mason, 1963). Carbonaceous chondrites also contain a higher abundance of CAIs (0.1-3 area% compared to <0.1 area% for other chondrites) (Krot, 2019). In general the non-volatile element abundances across the chondrites are similar to those measured for the sun's photosphere, CI chondrites have a truly solar elemental abundance whereas other chondrite groups (except for some CM chondrites) have a volatile depletion compared to the sun (Scott and Krot, 2007), suggesting that almost all Solar System materials have been thermally processed to some degree and a volatile component has been lost from the Solar System (Scott and Krot, 2007). Te-Cr isotope correlation studies have shown this volatile depletion is likely due to early Solar System mixing between a CI-like matrix

material and volatile depleted chondrules to form the depleted material (Hellmann et al., 2020). The only exception to this trend is the CR chondrites which did not plot along the same Te-Cr trend so likely had a different precursor material from a greater heliocentric formation distace, or a later formation time (Hellmann et al., 2020).

1.2.2 Calcium- and Aluminium-Rich Inclusions

Chondrites contain CAIs which are refractory aggregates and the oldest solids formed in the Solar System (Krot, 2019). CAI's are used as a way of dating the Solar System as they are considered the first solids to condense out of the solar nebula when the Sun was forming, their formation marks the beginning of several radiogenic clocks which are then able to be measured to get a formation age (Bouvier and Wadhwa, 2010), which is 4.567Ga (MacPherson et al., 2012). Most, if not all, CAIs formed within <~0.5 Myr after Solar System formation measured through radiogenic aluminium ratios (Wood, 2004). Both CAIs and chondrules formed within a temperature range of ~1900K to ~1400K (Wood, 2004). The presence of ^{10}Be is clear evidence that CAIs initially formed in a high temperature region close to the proto-sun (Schiller et al., 2015; Wood, 2004).

1.2.3 Achondrites

Whilst chondrites sample relatively unaltered parent bodies that accreted from dust present in the protoplanetary disk, achondrites have experienced significant geological processing. Achondrites are a subdivision of differentiated meteorites, shown in fig 1. Achondrites may have experienced planetary differentiation, or have been recrystallised and altered through impacts (Clayton and Mayeda, 1996). The driving force of this geological processing and melting divides the group into primitive and differentiated achondrites. Differentiated achondrites are those that have been fully molten and subjected to planetary scale differentiation and homogenisation of nebular chemical and textural features, such as those meteorites that come from Mars or Vesta. The samples from this group usually represent igneous samples from either the mantle or the crust of their parent body, many of these differentiated parent bodies have since been destroyed through catastrophic impacts (McSween et al., 2013).

Primitive achondrites are meteorites that have been thermally altered and in some cases melted since formation but not to the extent of being fully molten and differentiated and isotopically homogenised (Schrader et al., 2017). This means they preserve some primordial geochemical (e.g. near-chondritic bulk compositions (Greenwood et al., 2012a)), textural (some groups contain relict chondrules (Schrader et al., 2017)) and isotopic signatures (e.g.heterogeneous oxygen isotope reservoirs (Collinet and Grove, 2020a)) inherited from precursor materials and thus record the initial stages of planetary formation. Primitive achondrites include the acapulcoites-lodranites; brachinites; brachinite-like achondrites; winonaites; and the ureilites (Collinet and Grove, 2020a). They have experienced high-grade metamorphism (Greenwood et al., 2012b), and may have experienced incomplete segregation of metals into a core but not to the extent of a fully differentiated planetary body (Weiss and Elkins-Tanton, 2013). They retain the geochemical, isotopic, and bulk composition of chondrites, but have different textures caused by the various types of processing that they may have experienced e.g. thermal alteration/melting (differentiation), or impact bombardment (Greenwood et al., 2012b).

Ureilites are a group of primitive achondrite meteorites with a close resemblence to carbonaceous chondrites, especially in terms of the ultramafic, carbon-rich composition. However, the ureilites have experienced some melting and differentiation resulting in the loss of metal. The parent body differentiated enough to begin to segregate metals into a core and mantle but was disrupted before the mantle could fully homogenise as evidenced by heterogeneous oxygen isotopes (Sanders et al., 2017). Ureilites are the focus of this thesis as there is currently several debates regarding how the ureilites formed, as discussed below. This thesis aims to provide additional constraints onto these mysteries within the ureilite meteorite group to provide new insights into planetary formation and growth and the evolution of the ureilite parent body (UPB).

1.3 Aims of this thesis

This thesis aims to investigate the origin and geological history of the ureilite group. Specifically, the origin of diamonds within the ureilites, through microstructural analysis. This will be achieved through combining electron backscatter diffraction (EBSD); scanning electron microscopy and energy dispersive X-ray spectroscopy (SEM-EDS); Raman spectroscopy; electron probe microanalysis (EPMA) data; and optical microscopy studies to analyse the textures and fabrics of the samples (Appendix 1), the relationships between the graphite and diamond as well as their geochemistry.

1.4 Ureilites Overview

Ureilites were first discovered in India in 1868 when the sample Goalpara was found (Vdovykin, 1970), however they were not grouped and named until 1888 (Jerofeev and Lachinov, 1888). The ureilites take their name from Novo Urei, a sample which fell in Russia in 1886 (Vdovykin, 1970). They are classed as achondrites due to the lack of chondrules in their structure, but there was some initial ambiguity as some olivine and pyroxene aggregates within ureilites resemble chondrule-like textures (Vdovykin, 1970). These aggregates, particularly in Goalpara, have been noted to be similar to the inclusions seen in a carbonaceous chondrite called Cold Bokkeveld (Vdovykin, 1970). Cold Bokkeveld is a CM2 carbonaceous chondrite (Farsang et al., 2021). CM carbonaceous chondrites contain microchondrules of olivine and nickel-iron embedded within pyroxenes and other silicates in the bulk matrix (Mueller, 1969). Occasionally within Cold Bokkveld the pyroxene and the microchondrules are observed to separate which forms texture similar to that of ureilites like Goalpara, specifically single-crystal clinopyroxene with globular patches of olivine and troilite with carbonaceous matter at the grain boundaries (Mueller, 1966).

Other features of the ureilites include: heterogeneous oxygen isotopic compositions, cumulate textures and planetary-type noble gas abundances (Goodrich, 1992).‘Planetary-type’ noble gases refers to enrichment of heavy i.e., heavier than neon, noble gases and depletion of lighter noble gases (Goodrich, 1992; Ott, 2014). This is the opposite of ‘Solar-type’ noble gases which are enriched in helium and neon (Ott, 2014).) and trace element compositions are similar to that of carbonaceous chondrites which has led to some authors to propose that carbonaceous chondrites are the precursor material to the ureilites (Rubin, 1988).

1.4.1 Types of ureilites

According to the Meteoritical Bulletin database hosted by the Meteoritical Society there are currently 641 accepted ureilite meteorites (as of April 2022). The majority of these are

monomict ureilites, which means they are composed of a single lithology and are unbrecciated (Delaney et al., 1983). Around 10% of confirmed ureilites are what are known as polymict ureilites. Polymict ureilites are breccias composed of more than one lithology that represent near surface compositions of the ureilite parent body (Downes et al., 2008). Both types are beneficial to the overall study of ureilites. Monomict ultramafic ureilites sample the UPB interior whereas polymict ureilites sample the UPB surface. Some have been reported to contain lithologies that are indigenous to the UPB but not seen in other ureilite samples, for example andesite clasts in ureilite polymict breccias that have been linked to the UPB through oxygen isotope studies (Bischoff et al., 2014; Goodrich et al., 2015).

Ureilites also can be categorized into two end-member groups based on chemical compositions, specifically the Fo content of the olivine (Rai et al., 2020). Ureilite meteorites with $Fo_{<85}$ are more prevalent than olivine with $Fo_{>85}$ which means FeO rich ureilites are more common than MgO rich ureilites (Rai et al., 2020). Experimental work on the equilibration temperatures reached for these compositions show that the Fo content of olivine decreases with decreasing temperatures (Singletary and Grove, 2006). This means the FeO rich ureilites formed at lower temperatures (~1190°C (Rai et al., 2020)) than MgO rich ureilites (~1320°C (Rai et al., 2020)).

1.4.2 Mineralogy of the Ureilites

As the ureilites are ultramafic rocks they are primarily composed of olivine and pyroxene with a matrix that contains accessory minerals and the carbon (up to 8.5wt% (Goodrich, 1992)) component (Goodrich, 1992; Vdovykin, 1970). The olivine has reaction rims composed of very MgO rich olivine with inclusions of low-Ni iron metal (Goodrich, 1992). Olivine composition is described using the two end-member compositions, forsterite (Fo) is the Mg-rich end-member and fayalite (Fa) is the Fe-rich end-member. Olivine compositions can sit anywhere between these two end members. Here we express olivine compositions based on their forsterite content: Fo_{72} which means 72% of the (Fe,Mg) atoms are Mg and 28% are Fe. The core composition of the olivine in ureilites varies from Fo_{75} to Fo_{97} (Rai et al., 2020). Olivine crystals with compositions of $Fo_{<85}$ are more abundant than compositions of $Fo_{>85}$ and are described as iron rich in the context of ureilites (Rai et al., 2020), especially when compared to terrestrial mantle rocks which are around $Fo_{85\text{-}95}$ (Gaul, 2000).

Pyroxene is usually pigeonite in most samples, which is a high-Mg low-Ca clinopyroxene. Other pyroxene types have been recorded for some samples, including augite (Goodrich, 1992), orthopyroxene (Goodrich et al., 2001) and, in the Haverö meteorite, clinobronzite which is a form of enstatite (Berkley et al., 1980). Pigeonite grains also have reduction rims, composed of enstatite which is a very low-Ca pyroxene (Goodrich, 1992). Large augite grains have been interpreted as a primary mineral, especially in Mg-rich and Fe-rich end member ureilites but not in the intermediate samples (Takeda, 1987). Smaller augite grains are present as lamellae and blebby inclusions in large poikilitic pigeonite grains, which could be explained as a product of high temperature exsolution from the pigeonite (Goodrich, 1992). Some authors propose this mechanism is unlikely as the Wo (wollastonite: calcium content) is too low in the pigeonite to produce this (Goodrich, 1992). However more recent TEM-EDS analysis the pigeonite contains high-Ca and low-Ca regions with the high-Ca areas producing the lamellae (Mikouchi et al., 2010).

The accessory minerals within ureilites include cohenite ($(Fe, Ni, Co)_3C$)) (Nabiei et al., 2018), kamacite (Fe, Ni alloy) (Berkley et al., 1980), troilite (FeS) (Nabiei et al., 2018),

schreibersite ($(Fe, Ni)_3P$) and suessite (Fe_3Si) (Berkley et al., 1980). Cohenite is an iron carbide mineral which occurs within spherule inclusions in the silicate minerals (olivine and pyroxene), alongside Fe-Ni metal, sulphides, and phosphorous-bearing minerals (Goodrich, 1992). Kamacite, troilite and schreibersite are the prominent iron and nickel minerals within the ureilites. Kamacite is the most abundant of these three and can be found as spherical inclusions in silicate minerals; within veins; within diamond-graphite aggregates and forms part of the olivine reduction rims (Vdovykin, 1970). Kamacite, troilite and schreibersite are rarely found as mono-mineralic phases and more commonly form a polyhedral arrangement together (Nabiei et al., 2018). The low-Cr troilite is similar in composition to sulphides found in other meteorite groups such as aubrites (enstatite pyroxenite achondrites (Keil, 2010)) and enstatite-rich chondrites (Berkley et al., 1980). Suessite has been reported in very few ureilite samples and is interpreted as a secondary mineral formed through shock heating (Berkley et al., 1980).

Diamonds, graphite, chaoite (hexagonal carbon allotrope, lamellar habit), lonsdaleite (hexagonal diamond) and organic carbon are also present (Goodrich, 1992). However, it should be noted that lonsdaleite has since been discredited as a distinct mineral and is instead faulted and twinned cubic diamond (Németh et al., 2014). The carbon component of ureilites is up to 8.5 wt% (Nestola et al., 2020). These phases are found as aggregates within the matrix (Vdovykin, 1970), and some large (up to 1 mm) euhedral graphite and diamond has been reported (Goodrich, 1992). The organic matter luminesces in UV light and absorption spectra indicates presence of $-CH_3$, $=CH_2$, and C-N-H groups consistent with hydrocarbons of the paraffin series (Vdovykin, 1970). Hydrocarbons are only a small percentage of the carbon matter, average 2-5% (Vdovykin, 1970), and instead graphite is the most common form of carbon (Goodrich, 1992).

1.4.3 Textures of the Ureilites

Both monomict and polymict ureilites have been identified, the most notable of the polymict ureilites being Almahata Sitta (Goodrich et al., 2015). Monomict ureilites have two ‘end-member’ textures, the first being called typical ureilite texture and the second is poikilitic (Goodrich, 1992). Typical ureilites are characterised by large (~1 mm average (Goodrich, 1992)) silicate crystals which meet at 120° triple junctions (Goodrich, 1992), an example of the typical ureilite texture is shown in fig 2 which is an optical image of the Kenna sample used in this study. Carbon rich veins and interstitial matrix is present (Berkley et al., 1980) as well as elongation within grains reflecting a lineation and foliation (Goodrich, 1992). A characteristic feature of the pigeonite in typical ureilites is the lack of any exsolution features (Goodrich, 1992).

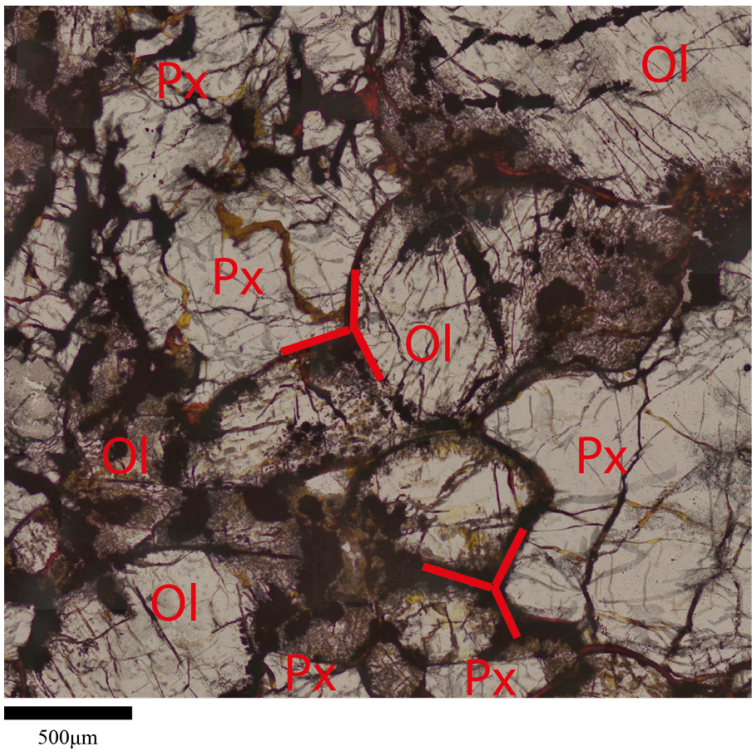

Figure 2: Optical image of the Kenna ureilite in plane polarised transmitted light. Kenna is considered to show typical ureilite texture. Annotations of the main minerals have been added using approved mineral abbreviations from (Whitney and Evans, 2010), ol is olivine and px is pyroxene. Further annotations have been added to highlight the triple junctions between silicate minerals that are nearly all over 1mm in size.

Poikilitic ureilites contain a more diverse range of pyroxene types, including pigeonite, augite and orthopyroxene (Goodrich et al., 2001). Augite may contain small, rounded inclusions of pigeonite (Goodrich, 1992), and any large (~15mm (Goodrich, 1992)) pigeonite or orthopyroxene grains will poikilitically enclose olivine or augite (Goodrich, 1992). Pigeonite in poikilitic ureilites has been reported to contain exsolution textures not seen in typical ureilites, such as augite lamellae (Goodrich, 1992). Poikilitic ureilite textures are strongly reminiscent of terrestrial igneous cumulate rocks and thus have been interpreted as likely to form through a cumulate process (Downes et al., 2008).

These are endmember textures, so some samples may contain features of both textures and are transitional (Goodrich, 1992). Some silicates, most prominently in the sample Kenna (Berkley et al., 1976) display a texture defined by elongations and alignments in the long shape axis. The strain-state of the silicates observed as dislocations and translational gliding along the (100) crystal plane in pyroxene suggests some form of tectonic deformation may have occurred (Berkley et al., 1980).

Silicate darkening is a feature identified through metallic grains of Fe-Ni metal that decorate or cut across silicate grain boundaries or traverse through the interior of silicate grains (Rubin, 1992). Observations of silicate darkening in ordinary and carbonaceous chondrites show that the higher the shock state of a sample the greater the degree of silicate darkening, indicating this is a feature that forms through shock processes (Rubin, 1992). This could be due to the relatively low Fe-FeS eutectic temperature of 998°C makes iron and troilite susceptible to migration during shock (Rubin, 1992). The ureilite Almahata Sitta contains graphite that has been measured through micro-Raman to have an average formation

temperature of 1314°C ± 120°C (Barbaro et al., 2022, 2020) which significantly exceeds the Fe-FeS eutectic temperature allowing for the iron and iron sulphides to melt during shock (Rubin, 1992). The curvilinear trails of metallic grains within silicates are a common feature noted for both olivine and pigeonite within ureilites (Rubin, 2006). Some of these trails are surrounded by olivine of lower FeO content, which is a feature of reduction (Rubin, 2006), however the trails that are not associated with reduction contain Fe sulphide which is a phase not caused by reduction and is instead characteristic of silicate darkening (Rubin, 2006). Silicate darkening in olivine has been attributed to shock stage S3 and above in the designation created by (Rubin, 1992).

The olivine grains are surrounded by a rim that is richer in MgO than the cores, these are a product or a reduction reaction taking place likely between core-composition silicates and the interstitial graphite matrix (Goodrich et al., 1987). Intergranular metals are enriched in Cr which was potentially derived from the reduction of the olivine (Goodrich et al., 1987). Reduced rim compositions have been observed to be consistent with a solid-state reaction formation as they plot along the trend for Fe/X-Fe/Mg for core olivine compositions (Goodrich et al., 1987). The rims observed in the sample Kenna have been reported with a width of ≤ 200 μm (Berkley et al., 1976). The average width across a range ureilite samples is ~40 μm (Berkley et al., 1976; Miyamoto et al., 1985; Takeda, 1987; Warren and Kallemeyn, 1992; Wlotzka, 1972).

1.4.4 Geochemistry and isotope ages of the Ureilites

1.4.4.1 Isotope ages

The ureilites Sm-Nd isotope age systematics (Goodrich et al., 1991) and lithophile element bulk geochemistry (Goodrich, 1992) suggests that they are highly fractionated igneous rocks.

Ureilites are dated to have formed ~1.6 Myr after CAIs based on thermal models of ^{26}Al planetesimal heating combined with Hf-W isotope systematics (Budde et al., 2015). This age places them at an intermediate point between iron meteorite parent bodies (~0.1-0.3 Myr after CAIs (Budde et al., 2015; Kruijer et al., 2014)) and non-differentiated (Chondrites >2 Myr after CAIs (Budde et al., 2015)) meteorite parent bodies (Broadley et al., 2020).

Samarium and neodymium isotope studies have shown several ages of either formation or significant events occurring across the ureilite group. MET 78008 is a calcic ureilite that has the highest REE abundance across the group generated two ages through Sm-Nd dating (4.09±0.08 Ga) and Rb-Sr dating (3.97±0.07 Ga) (Takahashi and Masuda, 1990). Kenna has model ages falling on an isochron of 3.74±0.02 Ga (also attained using Sm-Nd isotope systematics) (Goodrich et al., 1991). The Kenna ages were acquired when studying the LREE rich component (Goodrich et al., 1991; Goodrich and Lugmair, 1995) which can be isolated using a HNO_3 acid to form a leachate (Boynton et al., 1976). Whole rock Sm-Nd ages of ureilites have been reported to fall on a 4.55 Ga chondritic isochron (Goodrich et al., 1991; Torigoye-Kita et al., 1995). This data has been interpreted as the ureilites having a likely formation age closer to 4.55 Ga and then the LREE component was introduced, possibly as a metasomatic fluid, causing some samples to re-equilibrate (Goodrich et al., 1991). The Rb-Sr age difference between MET78008 (4.09±0.08 Ga and 3.97±0.07 Ga) (Takahashi and Masuda, 1990) and Kenna (3.74±0.02 Ga) could indicate that a metasomatic event occurred at least twice across the ureilite parent body (Goodrich et al., 1991).

1.4.4.2 Bulk geochemistry and Lithophile elements

The ureilites have two main endmembers in terms of bulk sample geochemistry, a 92 wt% FeO rich and at the opposite end 67 wt% MgO rich (Rai et al., 2020). The least shocked samples also contain the highest abundance of Fe (Takeda, 1987).

The lithophile element chemistry of ureilites closely resembles that of terrestrial and lunar ultramafic rocks (Goodrich, 1992). Alkali lithophile elements are depleted in ureilites with respect to chondrites (Vdovykin, 1970 ; Goodrich, 1992), this is thought to be due to removal of Al-rich melts in the early stages of ureilite formation as a partial melt residue (Collinet and Grove, 2020b). Lithophiles are primarily hosted within the silicate minerals (Vdovykin, 1970).

1.4.4.3 Refractory Elements

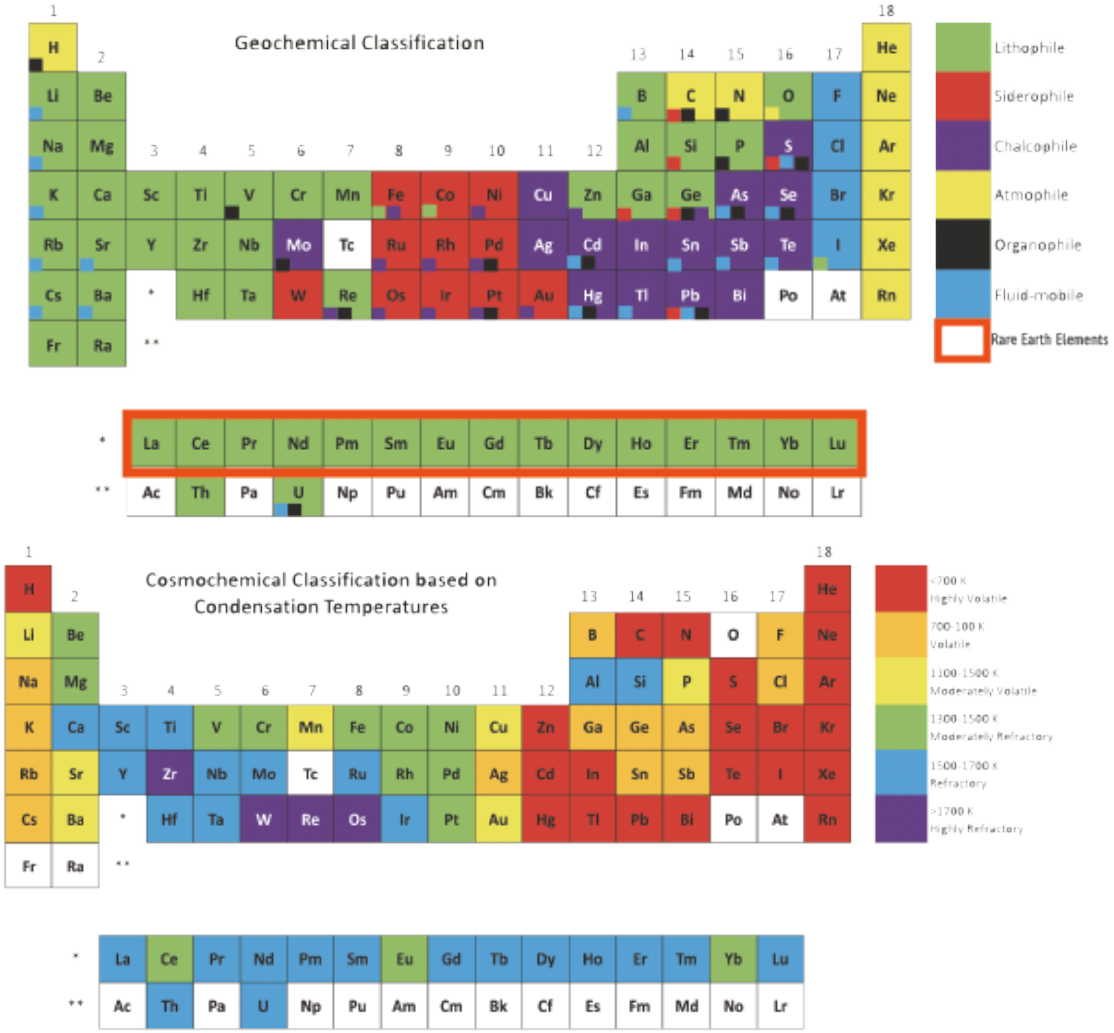

Figure 3: Geochemical and cosmochemical classification of the elements. Edited to include the Rare Earth Elements category.
Reprinted/adapted by permission from Springer Nature, Geochemical Classification of the Elements by Cin-Ty Lee. COPYRIGHT (Jan 1 2018)

Refractory elements are the elements that would have condensed out of the cooling solar nebula gas first (Jochum et al., 1986), this is due to the high solid condensation temperature (Lodders, 2003). Within the ureilites refractory elements are enriched in variable quantities within the interstitial vein metals (Goodrich, 1992). Refractory siderophile element (W, Re, Ir and Pt, siderophiles are highlighted in red in fig. 3) abundances are high whereas Pd and Au abundances are low which is a pattern similar to early condensates like CAIs, in particular those within the Allende carbonaceous chondrite (Goodrich, 1992; Wänke et al., 1972). Other refractory element abundances, e.g. Ti and Co also approach carbonaceous chondrite abundances (Vdovykin, 1970). There is also a refractory-poor phase within ureilites represented in geochemical analyses, this has yet to be explicitly identified petrographically but is thought to be a part of the ultramafic assemblage (Goodrich, 1992).

1.4.4.4 Rare Earth Elements

The Rare Earth Element (REE) chemistry of ureilites shows a v shaped trend between Light Rare Earth Elements (LREE) to Heavy Rare Earth Elements (HREE) with a large negative Eu anomaly in the middle, seen in fig. 4 (Goodrich, 1992). The REE are indentified in fig 3. This 'V' shape is due to relative enrichment in LREE and HREE but a depletion in middle rare earth elements (Goodrich, 1992). This pattern closely resembles terrestrial and lunar ultramafic rocks that have formed through partial melting of ultramafic rocks with a carbonate component in the mantle, and thus is non-chondritic (Goodrich, 1992). Is it unknown as to which phase contains the rare earth elements, but the LREE enrichment in particular resembles the imprint of metasomatic fluids seen in terrestrial ultramafic rocks (Dupuy et al., 1986; Goodrich, 1992; Stosch and Seck, 1980).

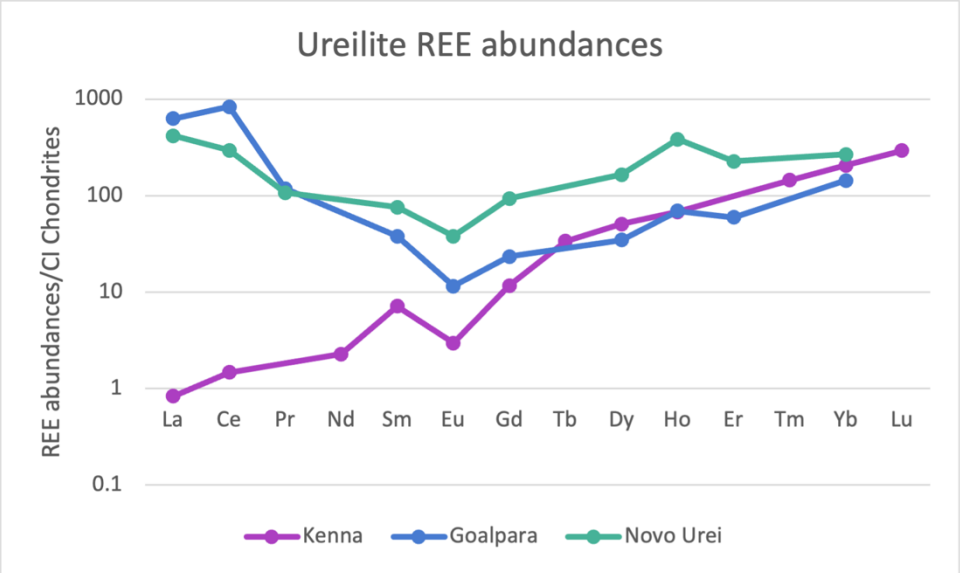

Figure 4: REE abundance graph showing data from Kenna (Spitz and Boynton, 1991), Goalpara and Novo Urei (Boynton et al., 1976). REE figures normalised to CI chondrites using data from (Evensen et al., 1978).

REE enrichment can also be attained by the partial melting of carbonates (Walters et al., 2013), if the precursor material of the ureilite parent body was carbonaceous chondrite this could provide the carbonates, however the enrichment appears to not be a uniform feature across all ureilites (shown in fig 4 where Goalpara and Novo Urei appear enriched whereas Kenna does not). A possible explanation may be due to the higher shock stage of Novo Urei

and Goalpara compared to Kenna (based on features identified in the results section using the shock classification system outlined in (Stöffler et al., 2018)), indicating the LREE may have occurred due to impact.

1.4.4.5 Siderophile Elements

Siderophile elements are enriched in ureilites when compared to terrestrial ultramafic rocks which are usually depleted in siderophile elements due to core segregation (Goodrich, 1992). Iron and sulphur (Berkley et al., 1980) are both depleted with respect to chondrites (Vdovykin, 1970). This could suggest some degree of core segregation has taken place, but not to the same extent as the Earth. The ureilite accretion age of ~1.6 Myr after CAI formation is within the time frame where the short-lived radioactive isotope ^{26}Al was still active, which could have provided enough heat for melting of the planetesimal and core segregation to begin (Broadley et al., 2020). This process did not reach completion, due to the ureilites not being fully homogenised with respect to their oxygen isotopes (Broadley et al., 2020). This isotopic heterogeneity suggests differentiation may have been halted by a significant impact/disruption event (Broadley et al., 2020). Re, Os, W and Ir have approximately chondritic relative abundances across the ureilite group ranging from ~0.1-1 times CI (Goodrich et al., 1987). Ni, Co, Au, Pd, Ga and Ge also have approximately chondritic relative abundances ranging from 0.1-0.2 times CI (Goodrich et al., 1987). The grouping of these elements is due to their compatibility in S-rich metallic systems (Goodrich et al., 1987). Group 1 (Re, Os, W and Ir) have high solid metal/ liquid metal distribution coefficients whereas group 2 (Ni, Co, Au, Pd, Ga and Ge) have low solid metal/liquid metal distribution/partition coefficients (Goodrich et al., 1987).

1.4.4.6 Noble Gases

Noble gases are closely associated with the carbonaceous phases, in particular diamonds, so may be co-genetic (Goodrich, 1992). Ureilites are enriched in primary Ar and Ne when compared to carbonaceous chondrites (Vdovykin, 1970), the relative abundances are close to 'planetary-type' or fractionated noble gas abundances (Goodrich, 1992), meaning enrichment in heavy noble gases (heavier than neon) and depletion in light noble gases (He and Ne) (Ott, 2014). Argon ($^{40}Ar/^{36}Ar$) ratios are very low which suggests little radiogenic argon is present and low helium ($^{4}He/^{3}He$) ratios also suggest little radioactive material in the original composition (Goodrich, 1992). Noble gas signatures in the ureilites are similar to those observed in chondrites so it is interpreted that ureilites either accreted some chondritic material or obtained noble gases in a similar way (Broadley et al., 2020). The mechanism for concentrating this noble gas signature has been tested experimentally and shows that gases of a nebular-like composition can form carbon-rich molecules with a noble gas signature similar to chondrites under ionising conditions (Broadley et al., 2020). This is then the mechanism that is proposed for introducing noble gases into the diamonds and amorphous carbon phases of ureilites (Broadley et al., 2020).

1.4.4.7 Oxygen Isotopes

The oxygen isotopes of the ureilites are the strongest indication that the rocks are primitive, and they fall close to the Carbonaceous Chondrite Anhydrous Mineral (CCAM) line (Goodrich, 1992). In particular, the oxygen bears a resemblance to carbonaceous chondrite types II and III (Vdovykin, 1970). There is a strong negative correlation between oxygen isotopes and Fo content of the olivine crystals, which indicates there may have been at least

two and possibly up to six separate oxygen reservoirs required for formation of these trends (Rai et al., 2020).

1.4.4.8 Carbon

Carbon abundance within ureilites (up to 8.5 wt% (Goodrich, 1992), average 3 % (Day et al., 2017)) approaches or exceeds the carbon abundance for carbonaceous chondrites (up to 5 wt% (Mason, 1963; Vdovykin, 1970). However there also appears to be a requirement for at least two separate reservoirs, one with high $\Delta^{13}C$ and a low MgO abundance; and a separate one with low $\Delta^{13}C$ and high MgO abundance (Rai et al., 2020). The location of the carbon adjacent to reduced olivine rims has led some to hypothesise carbon was introduced at a later stage to the ureilite parent body (Boynton et al., 1976; Wasson et al., 1976; Wlotzka, 1972) and was not originally part of the mineral assemblage. Carbon being introduced to the ureilite system would produce a reducing environment, this would create the disequilibrium textures including the reduction rims seen on olivine crystals composed of Mg-rich olivine and reduced Fe-metal (Rai et al., 2020). If carbon was present from the beginning of UPB evolution an equilibrium assemblage would be expected. However the association between the reduction rims and carbon indicates it was not an equilibrium phase, however the reduction reaction did not go to completion as it is only a rim (Miyamoto et al., 1985). The geochemistry of the carbon component, such as the concentration of noble gases and association with the LREE component (Wasson et al., 1976), correlates to an injection of carbon at the same time as the onset of rapid cooling (Berkley et al., 1980) likely due to impact (Boynton et al., 1976; Wasson et al., 1976). This is due to the concentration of planetary type noble gases contained in the carbon rich material, which indicates this material cannot have been hot for a long period of time otherwise the noble gases would have been lost (Wasson et al., 1976). Textural TEM studies of the ureilite Y74123 showed alternating lamellae of pigeonite and augite within the interstitial material between olivine-pyroxene grain boundaries (Ogata and Takeda, 1991). Textures like these within the interstitial rim material suggests the rims had crystallised prior to parent body break up (Ogata and Takeda, 1991) which would mean the carbon was potentially injected by a separate impact to the one that catastrophically disrupted the UPB.

However, the existence of carbon-rich metallic spherical inclusions within the olivine grains suggests the carbon was present in the ureilite material prior to impact (Singletary and Grove, 2003). A carbon injection also does not explain large (mm sized (Nestola et al., 2020)) graphite crystals present in ureilite samples that do not exhibit shock deformation, thus would not have been close to the injection site (Singletary and Grove, 2003).

1.4.5 Parent body size and ureilite formation

As the UPB is currently unidentified and potentially destroyed, the original size of the asteroid on which the ureilites formed is unknown. This has led to a range of sizes being suggested from a small partially differentiated planetesimal to a planetesimal that could have been as large as Mercury-Mars.

The observational evidence that suggests a large Mercury-Mars sized parent body for the ureilites include the potential requirement of high static pressures needed to form diamonds, in a comparable way to those diamonds found on Earth (Nabiei et al., 2018). Chromite, phosphate and iron-nickel metal inclusions have been reported in diamonds from the Almahata Sitta meteorite provide strong evidence for formation pressures of 20 GPa or above

(Nabiei et al., 2018). This observation has led to the conclusion the UPB had to be around Mercury or Mars sized (Nabiei et al., 2018). In addition, nitrogen isotopic studies of diamonds in Almahata Sitta show sector zoning, which implies isothermic growth at a 'sluggish' pace (Miyahara et al., 2015). Similar nitrogen zoning textures are observed in terrestrial diamonds that grew through static high pressures in Earth's mantle (Miyahara et al., 2015), the presence of nitrogen in terrestrial diamonds is attributed to mantle residence times and high temperatures (Kaminsky and Khachatryan, 2004). Slow growth of diamonds requires at least 2 GPa of pressure, and if the UPB had a small metallic core and silicate mantle as expected for a partially differentiated body, it would have to be ~1000 km in diameter to have high enough pressures at the core-mantle boundary to produce diamonds (Miyahara et al., 2015). If this size was the case then temperatures of at least 976 ℃ (Nabiei et al., 2018) would be required to allow core segregation to take place, leaving heavier Fe isotopes in the mantle (Rai et al., 2020). The ureilites are interpreted to represent this mantle, and formation temperatures range between 1320 ℃ for MgO rich samples down to 1190℃ for FeO rich samples (Rai et al., 2020).

The heterogeneous oxygen isotope composition across all ureilite samples has been considered evidence for a small UPB that could not have had any homogenising processes take place, or that the ureilites are in fact derived from multiple parent asteroids that experienced the same or similar geological histories (Clayton and Mayeda, 1988; Scott et al., 1993).

Size constraints on the UPB can also be provided by the oxygen fugacity. The oxygen fugacity (fO_2) can be calculated using the FeO content of the silicate minerals, assuming the fugacity is controlled by C-CO-CO_2 reactions (Berkley and Jones, 1982). Depending on the temperature of silicate-metal equilibration the pressures required range from 5 bars to 125 bars (Berkley and Jones, 1982). Models of ureilite formation involving reduction via carbon-redox smelting assumes smelting occurs over a range of depths, based on the pressure range given from fO_2 (Goodrich et al., 2004). These pressures correspond to a UPB of at least ~125 km radius (Goodrich et al., 2004). Smelting reactions indicate that for every 1 mole of olivine reduced, 1 mole of solid carbon must be consumed, and 1 mole of CO gas is formed (alongside 1 mole each of enstatitic pyroxene and iron metal) (Warren et al., 2006). Any significant smelting occurring on the UPB would result in large amounts of iron metal and considerable CO gas. A proportion of CO gas to rock above 10% would be unable to remain in the interior of any known asteroid (Warren et al., 2006). Smelting reactions measured for the most ferroan ureilites (Fo_{75}) the internal pressures correspond to a parent body of at least 690 km in diameter (Warren, 2012).

Several theories have been proposed to explain the primitive and processed textures within ureilites, including magmatic cumulate (Goodrich et al., 1987), residual partial melts (Boynton et al., 1976) and primitive solar nebula processes (Takeda, 1987). More recently the ureilites have been interpreted as the remaining material from a mantle that had experienced the extraction and depletion of some melt (Broadley et al., 2020), specifically S-rich metallic melts (Barrat et al., 2017). Originally the ureilites were viewed as igneous cumulates, but the discovery of heterogeneous oxygen isotopes resulted in a change in popular viewpoint to a mantle residue/restite model instead (Clayton and Mayeda, 1988; Warren et al., 2006).

1.4.5.1 Igneous models for ureilite petrogenesis

1.4.5.1.1 Residues vs cumulates

A cumulate, in terrestrial terms, is described as an accumulation of primary precipitate (liquidus) crystals close to the margin of a magma (Warren et al., 2006), essentially accumulations of crystals that form as minerals crystallise out of a magma and separate out of the magma chamber (Wager, Brown and Wadsworth, 1960). The cumulus crystals displace any trapped melt through compaction or continue to grow in chemical equilibrium with the main melt through adcumulus growth (Warren et al., 2006). Conventional cumulate models involve significant melting of the original parent material (Warren et al., 2006), which would be inconsistent with heterogeneous oxygen isotopes as reported for ureilites (Clayton and Mayeda, 1988). However, formation of ultrabasic rocks including lithologies such as dunites has been explained through crystal accumulation at high temperatures without remelting (Wager, Brown and Wadsworth, 1960).

Cumulate rocks may show some flow banding textures and mineral banding due to the physical processes of being in a magma chamber, such as crystal settling and convection (Hunter, 1996). However, a main argument in support of this theory are lineations and foliations defined by the shape of olivine and pyroxene crystals that are typical of terrestrial cumulates (Berkley et al., 1980).

Bowen's reaction series generally dictates the order of crystallisation from a magma, but this can be affected by external factors such as magma replenishment or the water content. In scenarios where water content is extremely limited/not present then olivine and plagioclase tend to crystallise first whereas in wet setting then olivine and pyroxene will crystallise first. This usually means that the ultramafic assemblage is concentrated at the bottom or the sides of the magma chamber (Walker and Agee, 1988).

If the ureilites formed as a cumulate rock then the carbon component is a primary phase alongside the ultramafic silicate assemblage (Berkley et al., 1980). However, the graphite crystals that have a low-density, seen in ureilites would be expected to float to the top of the magma chamber rather than settling out with the ultramafic assemblage at the bottom (Walker and Agee, 1988), this would mean that graphite would be expected to be extracted alongside the plagioclase component. Some ureilites contain euhedral graphite crystals which intrude into the silicate minerals, such as those reported for the paired ureilites Nova 001 and Nullarbor 010 (Treiman and Berkley, 1994). Paired meteorites refer to samples that are two fragments of the same meteoroid which separated during entry into the atmosphere or upon impact (Treiman and Berkley, 1994). Euhedral graphite crystals are interpreted as evidence of fluid-rock processes, which would suggest an igneous origin forming through magma chamber interactions (Treiman and Berkley, 1994). Their location within silicate grains and crossing grain boundaries in Nova 001 and Nullarbor 010 requires a silicate melt phase present whilst the euhredral graphite was forming from high pressure carbonic fluids, suggesting the silicate minerals and graphite could have formed as primary phases together (Treiman and Berkley, 1994). However, euhedral graphite flakes have also been reported in metamorphic rocks associated with high pressure fluid formation and subsequent precipitation (Sobolev and Shatsky, 1990).

Textural elongation of the silicate minerals could suggest some diffusional migration took place during growth, which has been experimentally tested to show how this could occur

alongside adcumulus growth (Walker and Agee, 1988) but may also form due to recrystallisation of minerals under stress (Takeda, 1987 ; Walker and Agee, 1988). Some lineations, foliations and mineral grading have been reported in ureilite samples such as Dingo Pup Donga, which are all characteristic features of cumulate rocks (Berkley et al., 1980). A mineral elongation lineation has been considered characteristic of how tabular minerals behave in a laminar fluid flow regime (Berkley et al., 1980; Goodrich et al., 1987; Goodrich et al., 1987). A laminar flow regime is difficult to reconcile with an asteroid parent body as this would require a very large magma chamber, and these have not been observed on known large parent bodies such as Vesta, the parent body of the HED group which has a mean radius of ~266 km (Ruzicka, Snyder and Taylor, 1997), this regime would also be expected to homogenise the oxygen isotopes (Takeda et al., 1988). However, it may also be possible to achieve these features through sedimentation and compaction in the solar nebula (Takeda, 1987). It is debated as to whether the sedimentation method would trap noble gases in the abundances that they are reported (Takeda, 1987).

The Multi-Stage Igneous Cumulate Model suggests the ureilites formed through internal differentiation processes, and are magmatic cumulates (Goodrich, 1992). The cumulate model gives a chondritic starting composition that undergoes 10-20% partial melt (Goodrich *et al.*, 1987) (Goodrich et al., 1987b). This produces the mafic cumulates (the ureilite parent material) this is then reduced which causes equilibrium crystallisation of metals 2-5% of which is trapped in the cumulates (Goodrich et al., 1987). The feldspar rich component would also be removed during this partial melting process (Goodrich, 1992). A crust would also be formed on the UPB that would likely be basaltic containing the majority of the plagioclase rich lithology, this creates a spatial separation between the plagioclase cumulates and the mafic cumulates (Goodrich et al., 1987). The mafic cumulates are then remelted, creating the ureilite parent material (Goodrich, 1992). If the first stage melting occurred at high enough pressures (at least 0.5-1kb (Goodrich et al., 1987)), then this would also explain the retained noble gases and the trace siderophile patterns as metallic iron would not be stable (Goodrich, 1992) and instead iron oxide would be the stable phase (Goodrich et al., 1987). The pressure in the source region would have to be above the iron-wüstite buffer, this is the oxygen fugacity buffer where Fe-rich silicates and metallic iron can coexist (Hirschmann, 2021), which at magmatic temperatures (1200-1400°C) would be 0.5-1 kbar (Goodrich et al., 1987). A typical chondritic body would have to have a radius of 235km to have pressures this high in the interior (Goodrich et al., 1987), which constrains the minimum size of the UPB. Pressures this high also allows for graphite to co-exist with metallic iron (Goodrich et al., 1987). Thus, this model predicts a UPB of at least 235km radius with a differentiated crust and no core (Goodrich et al., 1987).

One issue that has been raised with the cumulate model involves the volume of material produced. This model would be expected to produce only small volumes of ureilitic material, however, the existence of regolith breccias containing a large percentage of ureilite material infers that the ureilites are volumetrically abundant in the Solar System and thus must represent the main rock type of their parent body (Scott et al., 1993). This model also requires several different types of differentiated material with the ureilites as an ‘end-member’ so these other products would be expected to be represented in polymict ureilites (Takeda et al., 1988). Except for some andesitic clasts in Almahata Sitta (Bischoff et al., 2014) very few of these materials have been identified.

The ureilite suite lacks any complementary rock types that could represent a wall-rock composition, e.g., pyroxenites (Scott et al., 1993). If the ureilites were formed in small

magma chambers on their parent body then there would have to be a wall-rock to contain the magma chamber and prevent homogenisation (Scott et al., 1993) however no such samples have yet been found.

Another issue with the cumulate model is that it has been unable to successfully reproduce the HREE patterns, Eu anomaly, Mn/Mg and Ca/Al ratios, it also does not successfully account for the lack of plagioclase (Goodrich, 1992). This model also does not reconcile the oxygen isotope data, as the large-scale planetary differentiation required would result in equilibrium so the six different isolated oxygen reservoirs proposed as a cause for the variable oxygen isotope data would not be present (Goodrich, 1992).

1.4.5.1.2 Explosive Volcanism

The Explosive Volcanism Model also assumes the ureilites are products of differentiated chondritic material, but they are instead partial melt residues rather than cumulates (Goodrich, 1992). The source material would already be graphite rich and deep enough within the asteroid for graphite to be stable at magmatic temperatures (Warren and Kallemeyn, 1992). Partial melt residues are the remaining melt left behind after a substantial portion has been removed, for example with the ureilites the plagioclase component would have to be removed to leave an ultramafic residue (Keil and Bischoff, 2008). The ratios of olivine/pyroxene are generally consistent throughout the group and are as would be expected for a partial melt residue rather than a cumulate (Warren and Kallemeyn, 1989). A key argument for this theory is the composition of the pyroxene phase, in order to produce pigeonite as a stable phase the Ca/Al ratios in the precursor ureilite material must have been superchondritic, otherwise orthopyroxene would have been the stable pyroxene phase (Goodrich et al., 2007). As the currently observed Ca and Al abundances in ureilites are depleted with respect to chondrites (Goodrich, 1992; Vdovykin, 1970), the Ca and Al rich component (i.e. the basaltic lithologies) must have been extracted through partial melting (Collinet and Grove, 2020b).

Batch partial melting has also been experimentally shown to produce the CI-normalised siderophile element patterns for the ureilites (Goodrich et al., 1987). During the removal of silicate melts a portion of metallic (Fe) melt would also be extracted. The Fe-FeS eutectic temperature is ~100 °C which is likely to be lower than the silicate solidus, so to model the siderophile behaviour only the metal was melted (Goodrich et al., 1987). The model assumed chondritic starting composition with 25 wt% sulphur (Goodrich et al., 1987). The siderophile abundances measured for Kenna were matched at 90% melting, whereas the siderophile abundances for ALHA81101 were matched at only 10% melting (Goodrich et al., 1987). The amount of metal also varied, to match Kenna 30-40% of the original material had to be metal, but ALHA 81101 only required 3-4% (Goodrich et al., 1987). In order to reconcile this there would have to be a heterogeneous source material, or that the source material underwent various degrees of reduction in order to produce the metal some time prior to melting (Goodrich et al., 1987; Takeda, 1987). The source material could have been heterogeneous, as this would also go some way towards explaining the oxygen isotopes, but for reduction to be the cause of this there would also be expected to be a correlation between Mg/[Mg+Fe] (sometimes known as Mg#) ratios and siderophile abundances but this has not been reported (Goodrich et al., 1987).

The heat source for the partial melting could come from the decay of ^{26}Al (Scott et al., 1993). The REE abundances require up to 25% partial melting of the UPB (Goodrich, 1992), 25%

partial melting could be accommodated by the radioactive heat source. The lack of aluminium in the current ureilite samples indicate that the plagioclase (Al source) was removed in these initial melts (Goodrich, 1992; Scott et al., 1993). If the aluminium is removed, then there is no longer a heat source, so the UPB is never fully molten to homogenise and instead partial melting halts at 25% (Scott et al., 1993). The REE profiles displayed in fig 4 show an Eu anomaly which is consistent with the removal of plagioclase (Barrat et al., 2016; Goodrich, 1992).

Explosive volcanism is the culprit for loss of basaltic component, as volatiles present in basalts when approaching the surface of an asteroid <100 km in radius will enable the melt to reach or exceed escape velocity and be lost from the UPB (Goodrich, 1992). The volatiles could have been CO_2 and CO which would have been provided in abundance due to the high proportion of carbon (Goodrich, 1992), the volatile content in the magma must exceed 5000 ppm for a parent body ≥100 km in radius (Scott et al., 1993). The graphite that is within ascending magmas would be oxidised in a pressure sensitive reaction into CO/CO_2 compounds (Warren and Kallemeyn, 1992). The graphite would expand whilst being oxidised and this would happen rapidly, in excess of the asteroids escape velocity thus allowing for the material to leave the asteroid completely (Warren and Kallemeyn, 1992). It is important to note that proponents of this theory discount a possibility of impacts stripping the basaltic component, as an impact large enough would be likely to cause mixing between the interior ureilites and the exterior basaltic component (Scott et al., 1993). The ureilites would then be formed through batch melting on the parent asteroid followed by removal of the plagioclase rich component leaving behind the ultramafic assemblage (Warren and Kallemeyn, 1992). Following this, the ureilites were disrupted by a large impact that converts some graphite into diamond and subsequently causes a drop in pressure and temperature (Warren and Kallemeyn, 1992).

This Explosive Volcanism model may also explain the oxygen isotopes, as diffusion of O can be slow enough to not equilibrate between regions of an isotopically heterogeneous body during partial melt extraction (Goodrich, 1992). Over a timescale of 10 Ma oxygen atoms can diffuse ~3 mm when in olivine crystals, 200 mm in pyroxenes and 143 mm in basalts so reservoirs could be far enough apart to never mix (Goodrich, 1992). However, this would have to occur at pressures of over 100-200 bar to explain the correlation with Mg ratios (Goodrich, 1992). The Mg may be partly nebular in origin, if the UPB was carbonaceous and equilibrium between carbon-metal-olivine-CO/CO_2 was maintained then the Mg ratio would be determined by depth which would destroy any inherited correlation with oxygen (Goodrich, 1992). This model incurs problems with the noble gases, as if pressure drops to allow oxidation of carbon to CO/CO_2 to produce explosive volcanism then noble gases would also be expected to be lost (Goodrich, 1992). The stripped component would spiral away rather than re-accreting (shown in fig. 5), but some may have remained, which is seen in andesite clasts in ureilite breccias (Bischoff et al., 2014). Some authors proposing this model favour a multiple parent body approach and suggests that this explosive volcanism was common on C-rich asteroids that had some level of melting at depth (Warren and Kallemeyn, 1992). An example schematic of this theory is provided in fig. 5.

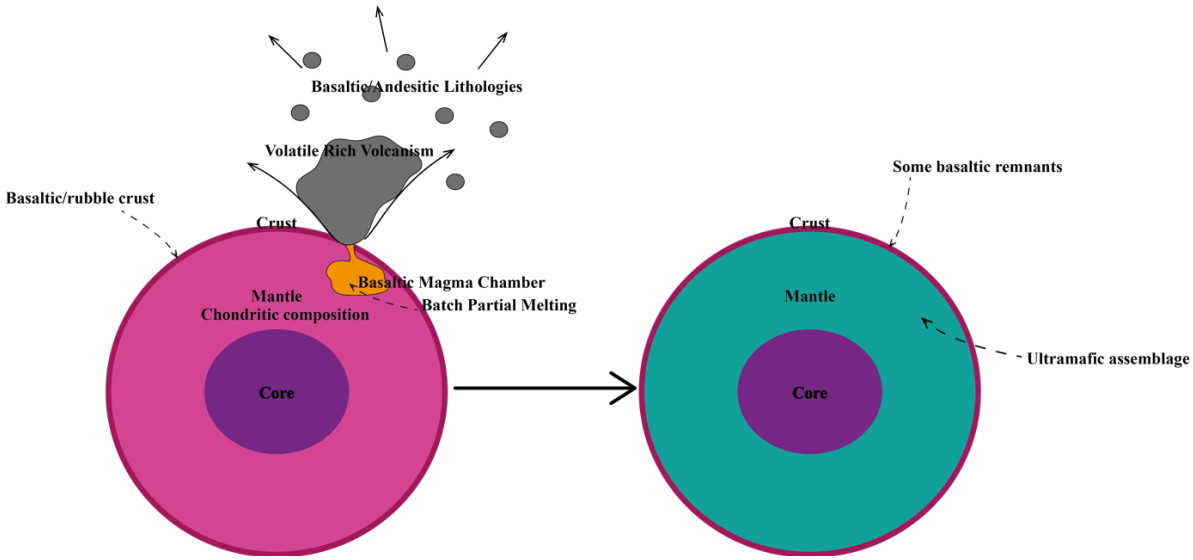

Figure 5: Simplified schematic of the Explosive Volcanism model. Created using information from (Warren and Kallemeyn, 1992, 1989)

1.4.5.1.3 Partially Disruptive Impact

Another igneous model for ureilite petrogenesis is the Partially Disruptive Impact Model hypothesises that a large carbon and noble-gas rich projectile impacted the UPB whilst it was still largely molten from primordial heating (Goodrich, 1992). This model is built from studies on a polymict ureilite called EET83309 (Warren and Kallemeyn, 1989). Assuming the parent material for the ureilites was chondritic in composition, a closed system differentiation mechanism should have produced an Al-rich basalt alongside the ultramafic ureilite material (Warren and Kallemeyn, 1989). At the near surface there would be a magma ocean, but below this would be a 'magmifer' or 'paracumulate' which is essentially a mix of crystals and melt that would have the properties of both cumulates and residue melts (Warren and Kallemeyn, 1989). Whilst still molten, this model suggests the UPB was severely disrupted by a carbon-rich impactor resulting in large cumulate crystals suspended within a C-rich magma (Warren and Kallemeyn, 1989). The impact would be between the partially molten UPB and a separate, also partially molten asteroid (Warren and Kallemeyn, 1989). These two asteroids would have similar $^{17}O/^{18}O$ ratios but the impactor would differ by at least 4‰ in $\delta^{18}O$ (Scott et al., 1993; Warren and Kallemeyn, 1989). This would create the textural properties of crystallisation from a C-rich magma alongside the geochemical properties of processed chondritic material (Goodrich, 1992). The impactor material is proposed to mix with the paracumulate introducing the C-rich, noble gas rich and $\delta^{16}O$ rich component (Warren and Kallemeyn, 1989). The result of this would be the paracumulate silicate crystals with a C-rich matrix, now known as the ureilite material (Warren and Kallemeyn, 1989). This formation would be consistent with a separate refractory-rich metal component and refractory-poor ultramafic assemblage (Goodrich, 1992). This model accounts for the missing plagioclase component by suggesting the impact blows the basaltic material off the body and is largely lost to space (Warren and Kallemeyn, 1989). This excavates the ureilite material from depth which causes a period of rapid cooling, seen in the 2-stage cooling interpreted by the rocks seen today (Goodrich, 1992). This model also has issues explaining the oxygen isotopes, but it attempts to reconcile the data through mixing of the 'magmifer' and impactor (Goodrich, 1992). A potential carbon-rich impactor could be a carbonaceous chondrite parent body impacting the UPB, studies of the ureilite DaG 319 found pristine dark clasts and variations of $\epsilon^{54}Cr$ that did not correspond to a mixing line (van Kooten et al., 2017). This has

been interpreted as being caused by admixing between ureilite matter and carbonaceous chondrite matter during a catastrophic impact, with the dark pristine clasts representing the impactor material (van Kooten et al., 2017).

1.4.5.1.4 Important Constraints

An important constraint on UPB petrogenesis is the evidence of a two-stage cooling history. Initially there was a period of very slow cooling, which allowed for the crystals to grow, at temperatures of 1200-1250℃ (Goodrich, 1992). This was followed by very rapid cooling, which formed the reduction rims around the silicates, this could have taken place at rates of 3-20 ℃/hr for the range of 1250-800 ℃ (Goodrich, 1992). The cause of this rapid cooling phase could be impact excavation, which would then expose the ureilites at the surface of the planet rather than sitting in the interior (Goodrich, 1992). If the residue theory is correct then this impact could also introduce carbon material to the ureilites causing disequilibrium (Berkley et al., 1980), which would exacerbate the formation of reduction rims due to reactions between the silicates and carbon (Rai et al., 2020).

The lack of an aluminous phase, e.g., plagioclase, is also one of the most important constraints on UPB petrogenesis, especially if the planetesimal theory is correct (Goodrich, 1992). If the bulk composition of the original material was largely chondritic, then at least 25% partial melting would be required to remove the plagioclase completely (Goodrich, 1992). However, if the ureilites are partial melt residues then the melt that was extracted must have been feldspar-rich and the ureilites must have been formed from a 2nd-stage melt (Goodrich, 1992). The sample Almahata Sitta is a brecciated meteorite which contained clasts of ureilitic material, and a wide variety of material from other meteorite types (Goodrich, 1992). One of the clasts was determined to be an andesitic clast (Goodrich et al., 2015), which has a genetic link to the ureilites through oxygen isotopes (Bischoff et al., 2014). This clast could represent the earlier melts extracted from the UPB and may have formed the crust of the UPB before impact (Bischoff et al., 2014).

Most authors have generally accepted a mantle restite origin where basaltic melt has been extracted from the original material, leaving behind the ureilites (Bischoff et al., 2014; Broadley et al., 2020; Goodrich et al., 2015). A mantle restite differs from a mantle partial melt as it is the remnant material that was not melted when partial melting occurred (Pitcher, 1997). Some evidence for the restite theory is the mineral composition itself. Ultramafic magnesium-rich olivine with primary pigeonite is typical of mantle restites that have lost trachyandesite melts (Broadley et al., 2020). The ureilites all have siderophile element abundances, specifically Ir, Os, Au and Ni that are too high to be explained through cumulate processes. If the UPB was sufficiently molten to cause a cumulate to form then the Ir content would be expected to be significantly depleted compared to a chondritic composition as all but ~1% would be removed into a S-rich melt, however this is not seen in ureilite samples (Warren et al., 2006). Most ureilites are only depleted in Ir by a factor of 5 compared to CI chondrites, survival of such near-chondritic abundances of Ir would be unexpected during all the processing required to form a cumulate (Warren et al., 2006). Another key observation that has led many authors to accept a restite origin is the low abundances of light REE and negative Eu anomalies, which have been explained through the removal of at least two partial melts the first being alkali-rich removing the plagioclase and producing the trachyandesitic material observed in relation to Almahata Sitta (Bischoff et al., 2014), and the second being alkali poor (Barrat et al., 2017).

1.4.5.2 Primitive Models for Ureilite Petrogenesis

Despite a large amount of ureilite scholars agreeing on a restite origin, there are other theories as to how the ureilites may have formed that involve minimal igneous processing on a large parent body.

1.4.5.2.1 Planetesimal Scale Collision

The Planetesimal Scale Collision Model assumes parent material is similar to carbonaceous chondrites containing troilite, metal and carbon (Takeda, 1987). The noble gases are also assumed to be present in the original material (Takeda, 1987). This then experiences a large impact, such as the collision of two planetesimals (Takeda, 1987) 10 km or larger (Takeda et al., 1988), causing compaction and preferred orientation of grains with shock heating (Goodrich, 1992). Extensive shock heating would allow for the silicates to grow larger whilst retaining the orientation that has been imprinted during the compaction through a mechanism called Ostwald Ripening (Takeda, 1987). The effects of this collision may be healed through annealing processes and dislocations rather than manifesting as highly shocked rocks (Takeda et al., 1988). A Ca-Al-Fe-rich silicate liquid and an Fe-Ni-S eutectic melt is extracted along the grain boundaries and squeezed out of the sample through the spin of the planetesimal or residual pressure from impact (Goodrich, 1992; Takeda, 1987). Only a small amount of melt may be present at any given time, but the total amount produced overall may be large (Goodrich, 1992). Estimates for the volume were calculated to be twice the modal abundance of plagioclase (2.5%) found in a polymict sample called Nilpena (Takeda, 1987). This process has both aspects of cumulates and partial melting (Goodrich, 1992) which could account for the textures present. A heterogeneous parent body would be required to reconcile oxygen isotope data, similar to the Explosive Volcanism Model, as if only small amounts of melt are present at any one time, then there would be no mixing between areas with a different isotopic signature (Goodrich, 1992). If the phases containing noble gases were never melted then this would explain their retention (Goodrich, 1992). The siderophile elements show evidence for solid metal fractionation, so either the UPB was heterogeneous in metal concentrations or metal was formed through reduction before melting (Goodrich, 1992). However, if reduction was involved then there would be a correlation between Mg ratios in silicates and siderophile abundances but there is not (Goodrich, 1992). Another issue with this model is the lack of explanation for loss of plagioclase, it remains necessary to remove a basaltic component through a minimum of 25% partial melting so for this model to work plagioclase would have to be preferentially melted due to low impedance to shock compression (Goodrich, 1992).

1.4.5.2.2 Nebular Sedimentation

The Nebular Sedimentation Model starts with a chemically non-chondritic UPB, so it is already depleted in plagioclase (Goodrich, 1992). This builds on the suggestion that the heterogeneous oxygen isotopes were established within the solar nebula (Clayton and Mayeda, 1988, 1996; Takeda, 1989). Early grown refractory magnesium rich silicates such as olivine and pyroxene were preferentially sedimented due to gravity at what would have been the midplane of the solar nebula and would have gained a preferred orientation (Takeda, 1989). Carbonaceous material would then have condensed and layered on the mafic material, this all then fragmented into planetesimals (Goodrich, 1992). Compaction of the UPB would have enhanced the preferred orientation of mafic grains and minor amounts of melting and thermal processes accounts for the metamorphic textures (Goodrich, 1992). Fragmentation of

the UPB due to a collision with another planetesimal would then cause rapid cooling (Goodrich, 1992). However, there is no evidence to suggest olivine and pyroxene were ever preferentially sedimented out of the solar nebula, and there are no other meteorites in any collection that are as fractionated as ureilites (whilst remaining primitive) and require a plagioclase depleted parent material (Goodrich, 1992). Although angrites, another group of achondrites, also may require a non-chondritic parent (Goodrich, 1992). If accretion of plagioclase-depleted material is possible then this negates the need for 25% partial melting, but it is not known if this model can reproduce the fabrics (specifically lineation) of the ureilites or if magmatic processes are required (Goodrich, 1992).

1.4.5.2.3 Unified Primitive Meteorite

The Unified Primitive Meteorite Model was not developed to specifically explain the formation of the ureilites, but instead to explain the formation of all primitive meteorites of which ureilites are one group (Goodrich, 1992). This model, like the Nebular Sedimentation Model, does not require a chondritic parent and instead discusses a set of processes that take place within the solar nebula common to all primitive meteorites. Primitive meteorites in this study include the chondrites (ordinary and carbonaceous), the enstatite meteorites (enstatite chondrites and aubrites), and the ureilites (Kurat, 1988). Initially there is a high temperature event causing the presolar matter to evaporate, this is followed by recondensation of this matter which is first deposited as olivine (Kurat, 1988). These condensates then aggregate into mm sized objects which get compacted whilst condensation is still taking place simultaneously (Kurat, 1988). A second heating event causes the aggregates to sinter and experience partial melting forming chondrules, followed by a vapour-solid exchange between Fe^{2+} and Mn^{3+} ions and sulphur metasomatism (Kurat, 1988). The aggregates then continue to accrete at low temperatures and form centimetre to decimetre sized aggregates (Kurat, 1988). The ureilites would have formed as aggregates of olivine with a primary orientation preserved as a fabric, the second heating event is proposed to be responsible for the metamorphic features observed in samples (Goodrich, 1992). Some geochemical features such as the depletion in Al, LREE, Ca and Ti is due to these elements being lost in the second heating event (Goodrich, 1992). Pyroxene crystals would have also been deposited from the vapour in the same way as olivine, and reactions between the vapour and the olivines would produce pyroxene with poikilitic textures (Goodrich, 1992). Metasomatism, if under oxidising conditions, would result in the range of FeO and correlated MnO (Goodrich, 1992). The aggregates would then collect dust from the remaining nebula, and this would provide the refractory siderophiles and carbon content (Goodrich, 1992). The plagioclase component would never be accreted, so would not then need to be lost (Goodrich, 1992). This model can explain the geochemistry fairly successfully, but it is inconclusive as to whether the fabrics and textures can actually be produced this way (Goodrich, 1992).

1.4.5.2.4 Impact-Melt

The Impact-Melt Model involves an impact on the UPB, similar to the Planetesimal Scale Collision model, which induced melt sheets within the resulting crater (Rubin, 1988). The UPB is proposed to have had a similar composition to CV-Chondrites (Examples: Allende, Vigarano) (Goodrich, 1992). Short lived igneous activity is proposed as a mechanism for trapping the noble gases and to preserve the Mg-O correlation that was established in the solar nebula, as the cooling was rapid enough to prevent equilibrium from being achieved (Rubin, 1988). Rapid cooling prevents complete separation of metallic melts, which accounts for the siderophile element patterns seen in the ureilites (Rubin, 1988). The depletion of

plagioclase is proposed to have occurred through a series of smaller impacts pre-dating the ureilite forming impact, which removed plagioclase melts accompanied with Fe-Ni-S eutectic melts (Goodrich, 1992). Smaller impacts would also account for the lack of zoning in the silicates and they would be removed due to metamorphic overprinting (Rubin, 1988). This model can explain the textural properties which indicate crystallisation from melts, and crystal settling or magmatic currents within the melts could account for the fabrics and lineations (Goodrich, 1992). Fabrics like the ones seen in ureilites have not been observed in terrestrial melt sheets, so this theory is not fully backed by observational evidence of similar structures (Goodrich, 1992). Another issue with this model is the evidence within the silicates that suggests they had long equilibrium times at high temperature which is inconsistent with rapid cooling (Goodrich, 1992).

1.4.6 Parent body disruption

It is generally agreed that the UPB experienced a catastrophic impact within the first 10 million years of its life (Nabiei et al., 2018) an example schematic of this is shown in fig. 6, this stunted the planetesimals growth so it never became a fully-fledged planet (Rai et al., 2020). With such an early impact, the planet was still hot from formation and radioactive heating which allowed for easier atomic diffusion causing reactions between silicates and the matrix (Rai et al., 2020). The olivine distribution shows that Fe-rich ($Fo_{<85}$ (Rai et al., 2020)) olivine is more abundant, suggesting the impact disturbed only the upper layers of the planetesimal which would have been more Fe-rich (Rai et al., 2020). The primitive silicates, carbon, and igneous phases all reflect the material that would be expected if an icy, carbon rich Kuiper belt object was flung into the inner Solar System and collided with a chondritic rocky planetesimal (Lisse et al., 2012).

All monomict ureilites show reduction rims on the olivines, and occasionally also the pyroxenes, which have been suggested to represent rapid cooling (10 °C/hour for the range 1100-650 °C (Goodrich et al., 2004). This shared pressure-temperature history across all known ureilites indicates a single original parent body that was catastrophically disrupted by a single major impact (Goodrich et al., 2004). This impact is unlikely to be responsible for the delivery of the ureilites to Earth as they show cosmic ray exposure ages of only <35 Ma (Goodrich et al., 2004). Thus, it is likely that following the catastrophic impact the disrupted material re-accreted into daughter rubble-pile asteroids (shown in fig. 6) or formed a rubble layer on the original UPB if any large pieces remained intact (Goodrich et al., 2004).

Observations of ureilites LEW 88774 (Goodrich and Harlow, 2001) and NWA 766 (Sikirdji and Warren, 2001) showed Cr-rich garnet surrounding the chromite appears to have crystallised at temperatures in excess of 1700°C (Goodrich et al., 2004). If the ureilites had previously cooled to temperatures of ~600°C then shock pressures of >80GPa would be required to heat the UPB to >1700°C (Goodrich et al., 2004). Shock pressures and temperatures this high would have caused melting of the olivine and subsequent recrystallisation, which are not observed (Goodrich et al., 2004). This means the UPB must have been hotter prior to impact which would allow lower temperatures than 1700°C (Goodrich et al., 2004).

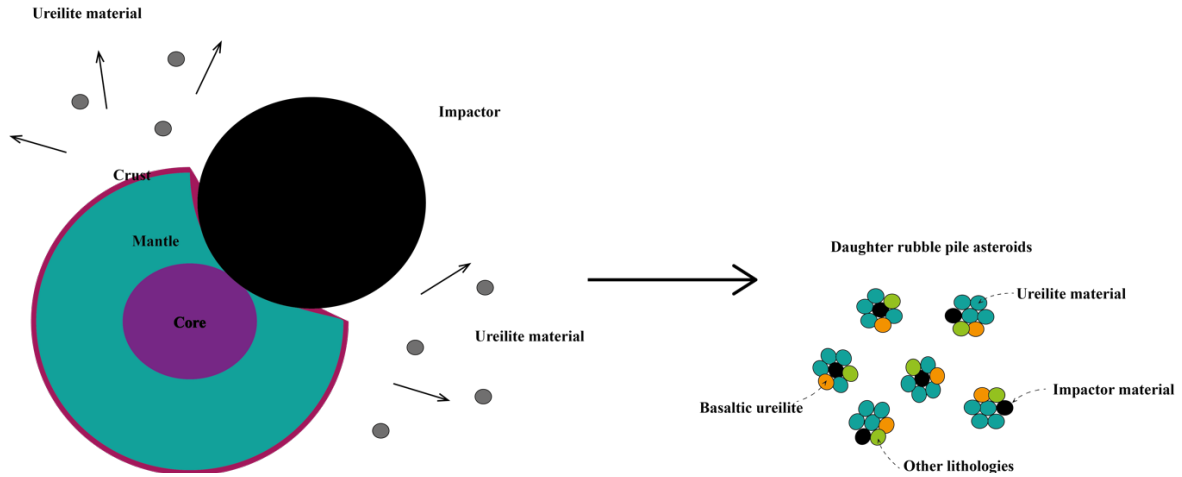

Figure 6: Simplified schematic showing ureilite disruption and re-accretion into daughter rubble pile asteroids. Created using information from (Goodrich et al., 2004)

1.4.7 Evidence for shock deformation

Monomict ureilites show varying shock states, however they are not consistently quantified (Goodrich et al., 2004). Ureilites discovered post-1991 have been classified based on Stöffler, Keil and Scott's shock scale S1-S6 (Stöffler et al., 1991), but those discovered and quantified beforehand have only been described as low, medium or high shock (Goodrich et al., 2004).

The lowest shock ureilites are described as shock stage S2-S3 (Rubin, 2006), which correspond to shock pressures of ~1-5 GPa and the main features would be fractured silicate minerals and mechanical twinning in pyroxene (Stöffler et al., 2018). Some samples have olivine that displays mosaicism and undulatory extinction, both of which are examples of how olivine changes due to shock metamorphism (Stöffler et al., 2018). Mosaicism of olivine occurs at pressures of 15-20 to 60-65 GPa (Stöffler et al., 2018) and as these samples also show undulatory extinction that can be constrained. Undulatory extinction occurs at 4-5 to 15-20 GPa (Stöffler et al., 2018) so as there is undulatory extinction and mosaicism it is likely the olivine experienced shock of 15-20 GPa. No high-pressure polymorphs such as wadsleyite, ringwoodite or ahrensite have been reported for ureilites even the highest shock samples (Nestola et al., 2020). Olivine transitions to high pressure polymorphs is well known and is proposed to be responsible for seismic discontinuities within the mantle at 400km and 670km depth (Suzuki et al., 2000). Olivine first transitions to wadsleyite and this is attributed to the seismic discontinuity at 400km, this then becomes ringwoodite at higher pressures and is responsible for the discontinuity at 670km (Suzuki et al., 2000). Ringwoodite is listed as a feature of S6 shock metamorphism equating to shock pressures of 45-55GPa or greater (Stöffler et al., 1991; Xie and Sharp, 2004). However, in static high pressure geological environments (e.g. the mantle of Earth) ringwoodite can be stable at pressures of 18-22GPa (Katsura and Ito, 1989; Xie and Sharp, 2004).

The highest shocked ureilite samples are at least shock stage S5 but some samples (ALHA 81101 (Bischoff et al., 1999; Li et al., 2021)) could possibly be as high as S6, due to the extreme recrystallisation of the olivine (Li et al., 2021). A shock stage of S5 corresponds to ~42-45 GPa (Stöffler et al., 2018) in shock pressure with the main textural changes being the loss of pleochroism in mafic minerals; presence of melt veins and pockets; planar

deformation features (PDFs) in pyroxene; and mosaicism, although mosaicism can occur at shock stage S4 (Stöffler et al., 2018).

1.4.8 The diamond problem

The abundance of diamonds within the ureilites has sparked several theories about their origin and formation. There are three main competing theories. One hypothesises the diamonds have a shock origin and were converted from graphite through catalysis evidenced by blade shaped morphologies of carbon masses containing diamonds embedded along with graphite (Nestola et al., 2020). This shape resembles that of euhedral laminate graphite in low shock ureilites argued to represent the primary state of carbon in the ureilite group (Nestola et al., 2020). The blade morphologies of the diamonds are interpreted as evidence they pseudomorphed from euhedral graphite crystals, and they could have grown so large (up to 100 μm) due to catalysis of the reaction (Nestola et al., 2020). In industrial production of diamonds the reaction to form diamond from graphite is catalysed by (Fe, Ni, Co)-C liquids (Nestola et al., 2020). In these conditions hexagonal graphite can pseudomorph to cubic diamond *in situ*, thus negating the need for atomic diffusion (Erskine and Nellis, 1991), which preserves the layered structure and morphology of graphite (Isobe et al., 2013). The iron and nickel phases are present as spherules which suggest they were molten at magmatic temperatures, which could have provided the necessary liquids for catalysis (Nestola et al., 2020).

The shock theory hypothesises that graphite is primary and is the unshocked state of ureilitic carbon (Goodrich et al., 1987) demonstrated in fig. 7, and was converted to diamond through a combination of shock pressure and catalysis (Nestola et al., 2020). Diamonds within other meteorites, such as Canyon Diablo, appear to be formed through shock so the same could be true for the ureilites (Vdovykin, 1970).

Carbon isotope studies show that the $\delta^{13}C$ values are the same between the diamonds and graphite, which suggests formation of both phases in a way that did not fractionate the C isotopes (Grady et al., 1985). This theory hypothesises that if the planetesimal was Mercury-sized, then in the conditions 4.5 Ga ago, the temperature of the interior of this planetary body would exceed 1275 ºC (Nestola et al., 2020). At this temperature and pressure $(Fe, Ni)_3(S,P)$ phases would melt so could catalyse a transition from graphite to diamond (Nestola *et al.*, 2020). In meteorites such as Elga (Iron, not Ureilite) this same phase is reported as shock melt veins (Litasov et al., 2019 ; Nestola et al., 2020) so it is possible to produce a molten version during shock. The mosaicism of olivine in some ureilites indicates the ureilites experienced shock pressures of at least 15 GPa (Stöffler et al., 2018), which is sufficient to also form the diamonds (Nestola et al., 2020).

A study of three ureilites (Dyalpur, Goalpara and Novo Urei) indicated the diamonds formed in a preferred crystallographic orientation, which was interpreted as proof of shock formation (Lipschutz, 1964). Other studies have also concluded shock is a likely formation mechanism for ureilitic diamonds including a cathodoluminescence (CL) study comparing ureilites to the Ries Crater (Grund and Bischoff, 1999). The diamonds found at the Ries crater are shock diamonds formed at the time of impact when an asteroid struck the Earth (Hough et al., 1995) several other impact craters on Earth also have shock diamonds forming where the impact occurred into carbon-rich rocks, e.g., the Popigai Crater (Masaitis, 1998). The CL study found the spectra to be similar between the Ries Crater and the ureilite samples and concluded they were both formed in a comparable way (Grund and Bischoff, 1999). Several

authors have concluded the Ries crater diamonds are shock generated however there is a potential alternative (Goresy et al., 2001; Langenhorst et al., 1998). The reported finding of silicon carbide (SiC) within the diamond host rocks of the Ries crater is considered inconsistent with a shock origin as this phase has not been reported for any experimental diamonds (Hough et al., 1995). Instead, diamond is well-known to form on silicon-rich substrates during chemical vapour deposition (CVD) growth (Hough et al., 1995). This study concluded that the impact forming the Ries crater created a carbon-silicon rich vapour, or potentially plasma, that the diamonds and SiC condensed out from (Hough et al., 1995). The diamonds found in the Popigai impact crater are interpreted as shock generated diamonds that grew through a martensitic transition from graphite to diamond as they retained the shape of the graphite within aggregates (Kenkmann et al., 2005).

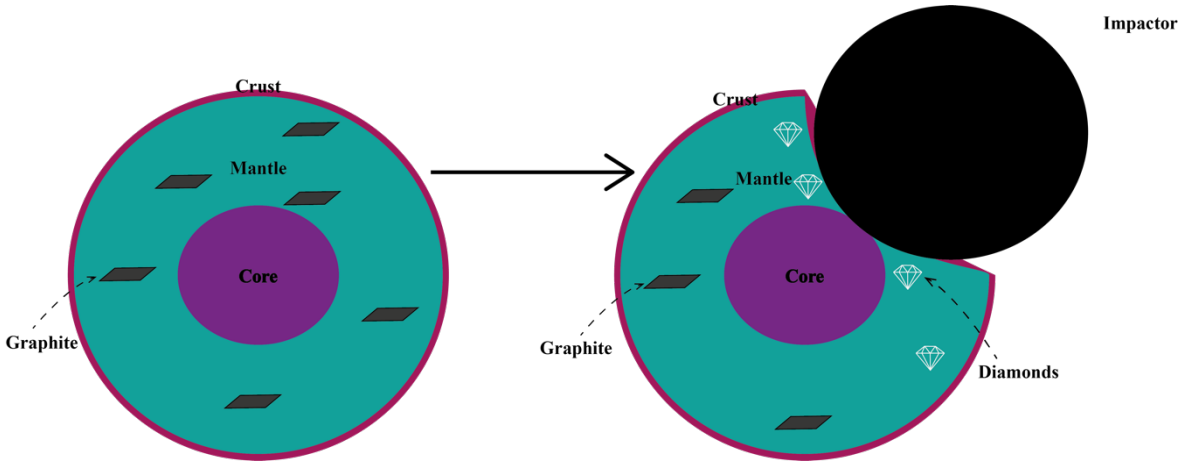

Figure 7: Simplified schematic of diamonds formed through shock. Created using information from (Nestola et al., 2020)

The second theory suggests the diamonds formed through high static pressures within a large planetesimal evidenced by cohenite, iron-nickel metal and phosphate inclusions within diamond, and graphite formed from the diamonds through graphitisation (Nabiei et al., 2018). Graphitisation is a process where diamond dissolution and subsequent graphite precipitation occurs (Korsakov et al., 2015). Combined with this evidence, there are segmented diamonds where two segments of the same or similar crystallographic origin are separated by graphite bands (Nabiei et al., 2018). The diamond segments contain inclusion trails which can be traced across segments, but not seen in the middle graphite band (Nabiei et al., 2018). This has been interpreted as evidence that the diamonds were primary, and the graphite formed secondary, likely due to shock heating (Nabiei et al., 2018). The ureilite Almahata Sitta contains large diamonds (~100 μm (Nabiei et al., 2018)). Similar large dimonds are not reported for any other ureilite meteorites. Shock growth on impact with Earth can be ruled out due to the asteroid breaking up considerably in the atmosphere and falling freely based on the individual fragments weight (Goodrich et al., 2015; Jenniskens et al., 2010; Miyahara et al., 2015). One sample that was noted to contain large diamonds, Almahata Sitta MS-170, is classified as shock stage S3 so not a highly shocked sample (Miyahara et al., 2015). The size of the diamonds, and the nitrogen sector zoning mentioned above signifying slow formation, is inconsistent with shock experiments (Nabiei et al., 2018). Shock experiments and natural shock measured in the Solar System occurs in the order of nanoseconds, or a few seconds as a maximum (Nabiei et al., 2018). The grain size of shock produced diamonds is typically nanometres in scale, the only exceptions being the Popigai or Ries craters that had graphitic

precursors and could form aggregates that were several hundred micrometres although the individual crystallites are maximum ~150 nm (Nabiei et al., 2018).

The larger diamonds have been proposed to form at high static pressures within the interior of a large planetary body (shown in fig. 8), similar to terrestrial diamonds (Nabiei et al., 2018). Terrestrial diamonds form through redox reactions of carbonate, or through metasomatism (Stachel and Harris, 2009). They are sourced from eclogite regions of the mantle at depths of at least 140 km, but some diamonds have Fe-Ni metal inclusions which correspond to formation at depths greater than 240 km (Stachel and Harris, 2009). In eclogite xenoliths within kimberlite pipes both graphite and diamond can be found (Berkley et al., 1980). Large ureilite diamonds with inclusions of chromite and Fe-S-P phases are inferred to form at static pressures of 20 GPa or higher within the mantle of a differentiated body, which means the parent body that they formed on must have been at least ~235 km diameter for core formation to start and possibly up to the size of Mercury or Mars (Goodrich, 1992). Metal, sulphide, carbide, and phosphide phases ($(Fe,Ni)_3(S,P)$) being present as inclusions within diamond and in association with diamond has been taken as definitive evidence of formation at ≤20 Gpa due to their stability range (Nabiei et al., 2018; Nestola et al., 2020) These phases are believed to have been originally trapped within the diamonds in an already crystalline form, due to their faceted nature which would not be seen if trapped as a melt (Nabiei et al., 2018).

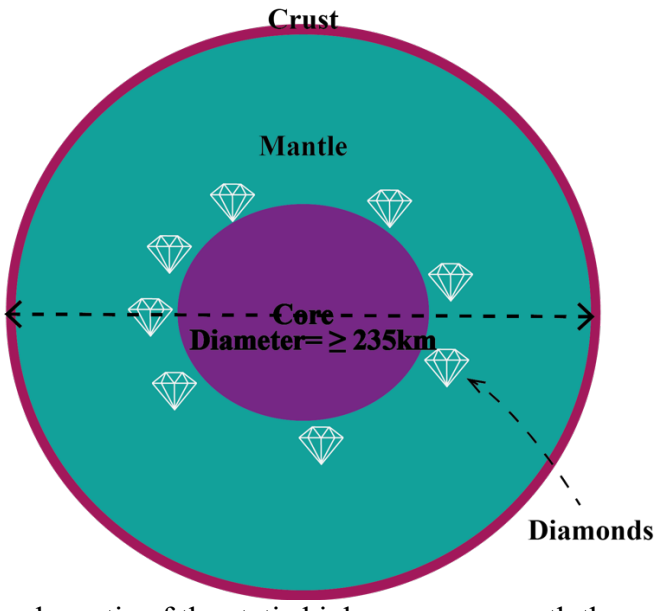

Figure 8: Simplified schematic of the static high pressure growth theory for diamonds. Created using information from (Goodrich, 1992; Nabiei et al., 2018)

The third theory postulates that the diamonds formed through chemical vapour deposition (CVD) in the solar nebula (Goodrich, 1992) due to the abundance of trapped noble gases. This theory hypothesises that the diamonds formed through reactions within the solar nebula involving H_2CH_4 (Goodrich, 1992). This type of diamond growth would be able to trap noble gases, but the graphite would not (Goodrich, 1992). Experimental work synthesising CVD diamonds from H_2 and CH_4 with Ar present showed that Ar was trapped in concentrations 3-4 orders of magnitude smaller than the values measured in ureilites, but still too high to be attributed to other diamond formation mechanisms (Fukunaga et al., 1987). However, the noble gases are only trapped in the diamonds when diamonds are present in the sample, there is no change in abundances between diamond-rich and diamond-poor samples (Goodrich,

1992). Chemical vapour deposition has been ruled out as a potential formation mechanism for the ~100 μm diamonds seen in Almahata Sitta as it is inconsistent with the inclusions and the pressures required to form them (Nabiei et al., 2018).

It is possible that a combination of certain factors from each theory could be correct, for example if the parent material was a troilite-metal bearing carbonaceous chondrite bulk material then diamond and graphite could be produced simultaneously due to a collision with another large body, along with the preferred orientation (Takeda, 1987).

1.4.9 Asteroid 2008 TC_3 and Almahata Sitta meteorite

A significant event surrounding the ureilites is the fall of the Almahata Sitta meteorite. On October 7th 2008 the asteroid 2008 TC_3 was the first asteroid to be detected in space prior to impacting Earth and producing a meteorite sample (Bischoff et al., 2010). The meteorite in question was classified as a polymict ureilite, now named Almahata Sitta (Goodrich *et al.*, 2015) with a wide range of lithologies being represented, including chondritic material as well as fine and coarse grained ureilites (Bischoff et al., 2010). Despite the range of lithologies reflectance spectra of the asteroid prior to entry of Earth's atmosphere the initial parent of 2008 TC_3 is also the immediate parent of the ureilite group (Goodrich et al., 2015). One of the lithologies recovered included an andesitic sample that was reported to be related to the ureilites due to oxygen isotope studies and had a formation age of 6.5 Ma after CAI (Bischoff et al., 2014; Goodrich et al., 2015). This discovery is considered proof that a crust of intermediate Si composition was once present on the UPB and is evidence of magmatic activity taking place on the UPB to at least 6.5Ma after CAIs (Bischoff et al., 2014). The disruption of the UPB could have created daughter asteroids which may still exist in the asteroid belt, one of these would have been the parent of 2008 TC_3 that based on cosmic ray exposure ages is thought to have broken away from the larger asteroid 19.5 ± 2.5 Myr ago (Jenniskens et al., 2010). Ureilites were previously thought to possibly derive from S-type asteroids due to the reflectance spectra of this asteroid group having similarities with dunites or basalt lithologies containing some Fe-Ni metal (Gaffey et al., 1993). However asteroid 2008 TC_3 was detected to have spectra similar to that of B or F-type asteroids. B-type asteroids contain hydrous minerals and an -OH group vibration band in the spectra which was missing for 2008TC_3 (Jenniskens et al., 2009). This leaves the F-type asteroids as the likely candidate for the origin of 2008 TC_3 and furthermore the ureilites. F-type asteroids are known to be rich in carbon, and similar to the reflectance spectra of the carbonaceous chondrites (Hiroi et al., 1993) but were not previously considered to have any direct meteorite analogues as the carbonaceous chondrites have a better match with C-type (Potin et al., 2020)(e.g. Ryugu (Michikami et al., 2019)) or potentially K-type asteroids (Clark et al., 2009; Jenniskens et al., 2010).

2.0 Summary and Project Proposal

The key questions that remain unanswered with the ureilites are the uncertainty of mode of their formation, cumulate or residue, the origin of the diamonds and the size of the parent body. These processes can be determined and distinguished through quantitative textural analysis of minerals such as olivine within ureilites. Olivine is the dominant mineral present in ureilite samples and has been well characterised in a variety of mantle and shock settings. This project will explore the deformation microstructures present within the minerals using EBSD, SEM-EDS and Raman spectroscopy to determine the likely deformation environment. Igneous and metamorphic rocks on Earth develop distinct petrofabrics depending on the environment they formed in, so these can be compared to the ureilites to constrain the conditions that ureilites were subjected to. Applying this approach to ureilites could help distinguish whether a giant impact or lithostatic overburden was the dominant factor in ureilite diamond development. Electron backscatter diffraction (EBSD) is the main technique that will be used, as this is an excellent way of visualising and quantifying microstructural data. The EBSD data will be augmented using optical and geochemical techniques including energy dispersive X-ray spectroscopy (EDS), transmitted and reflected optical microscopy and Raman spectroscopy.

3.0 Methodology

3.1 Sample selection and background

The samples selected for this study are all monomict ureilites. Monomict ureilites were preferred over polymict samples to study ureilite textures, chemistry and microstructures without contamination from other meteorite groups. The samples chosen include a range of shock levels from low-medium shock up to highly shocked, this is to compare textures across shock levels to piece together the geological history. A summary of some key parameters of these samples is provided in Table 1.

All samples were provided as thin sections.

3.1.1 Miller Range 090076 and 090980

Two of the samples studied in this thesis are from Miller Range mountains in Antarctica. These were not observed falls and both were found during the 2009 search by the US Antarctic Search for Meteorites ANSMET program.

3.2.1.1 090076

Miller Range 090076 was approved in September 2010 and classified in the Antarctic Meteorite Newsletter volume 33 issue 2. Following this it was reported in the Meteoritical Bulletin number 99 in April 2012. Hand specimen description reported on the Meteoritical Bulletin describes this sample as having a brown/black fusion crust with evaporites, areas without the fusion crust are described as containing rusty areas, visible metal, and high oxidation of the matrix. The rustiness reflects the terrestrial weathering grade which is classed at B/C meaning moderate to severe rusting likely meaning the meteorite was on Earth and subjected to terrestrial weathering for a while.

Mineralogy listed in the Antarctic Meteorite Newsletter volume 33 issue 2 reports olivine core composition of Fa_{22} (Fo_{78}) and pyroxene composition of $Fs_{11\text{-}18}Wo_{5\text{-}11}$.

3.2.1.2 090980

Miller Range 090980 was approved in February 2012 and was reported in the Antarctic Meteorite Newsletter volume 35 issue 1 in March 2012, following this it was reported in the Meteoritical Bulletin number 100 in June 2014. Hand specimen description from the Meteoritical Bulletin describes this sample as having 80% covered in a black fusion crust that has polygonal fractures. The interior is described as rusty and containing rusty chondrules. The weathering condition is a C grade which means severe rusting and metal particles visibly rusted which suggests this sample had also been subjected to significant terrestrial weathering before being found.

Mineralogy listed in the Antarctic Meteorite Newsletter volume 35 issue 1 in March 2012 reports olivine core composition of Fa_{22} (Fo_{78}) and pyroxene composition of $Fs_{18\text{-}19}Wo_{8}$ (En_{73}).

3.1.2 Goalpara

Goalpara was not an observed fall and was instead found in 1868 in the Province Assam in India (Vdovykin, 1970). This sample was the first ureilite to be found, but not grouped until later (Vdovykin, 1970). It has not been reported in the Meteoritical Bulletin, likely due to the age of the sample. The olivine grains have been described as 'recrystallised (Carter et al., 1968)' and this was later attributed to high shock causing mosaicism (Berkley et al., 1980; Lipschutz, 1964).

Olivine core composition has been reported as Fo_{75} and pyroxene is pigeonite $Fs_{18}Wo_{7.7}$ ($En_{74.3}$) (Bhandari et al., 1981).

3.1.3 Kenna

Kenna was also not an observed fall and was found in February 1972 in New Mexico, USA. It takes its name from the town where it was found (Berkley et al., 1976). At the time of discovery it was the seventh known ureilite worldwide. This sample is reported to contain carbon polymorphs including graphite and diamond (including cubic diamond) (Berkley et al., 1976) and has petrographic evidence for medium shock effects (Goodrich, 1992).

Olivine core composition has been reported as $Fo_{79.2}$ with a pigeonite composition of $En_{73}Wo_{9}Fs_{18}$ (Berkley et al., 1976).

3.1.4 Hajmah

Hajmah was found in Oman during an oil prospecting mission in the area also called Hajmah. There is minimal information about the find with the date being given as 'before 1958 (Graham, 1978)'.

Olivine core composition has been reported as $Fo_{84.5}$ with a pigeonite composition of $En_{85.7}Wo_{9}$ ($Fs_{5.3}$) (Goodrich, 1992).

3.1.5 Novo Urei

Novo-Urei is the type specimen for the ureilite group. This is because it was an observed fall on the 4th of September 1886 in Russia (Vdovykin, 1970). Three stones fell but only one was recovered weighing 1.9 kg (Vdovykin, 1970). This was the first meteorite reported to contain diamonds (Vdovykin, 1970).

Olivine core composition has been reported as $Fo_{78.9}$ with a pigeonite composition of $En_{72}Wo_{10.2}$ ($Fs_{17.8}$) (Goodrich, 1992).

3.1.6 Summary table

Table 1: Summary table of some main parameters of the samples used in this study.

Sample	**Mineralogy**	**Weathering State**	**Carbon Phases**	**Shock stage**	**Fall or Find**
MIL090076	Olivine (Fo_{78}), pigeonite ($Fs_{11-18}Wo_{5-11}$), carbon and metal (Antarctic Meteorite Newsletter volume 33 issue 2).	C grade (severe rusting (Meteoritical Bulletin 100))	Not reported.	Low shock, no shock features reported.	Find (Antarctic Meteorite Newsletter volume 33 issue 2)
MIL090980	Olivine (Fo_{78}), clinopyroxene ($Fs_{18-19}Wo_{8}$), carbon (Antarctic Meteorite Newsletter volume 35 issue 1).	B/C grade (moderate to severe rusting (Meteoritical Bulletin 99))	Graphite, diamond (own results, see below).	Planar fractures (own results) indicating at least shock stage S3 (Stöffler et al., 2018)	Find (Antarctic Meteorite Newsletter volume 35 issue 1)
Goalpara	Olivine (Fo_{75}), Pigeonite ($Fs_{18}Wo_{7.7}$) and Kamacite (Bhandari et al., 1981; Vdovykin, 1970)	No weathering state reported.	Diamond, Lonsdaleite (Vdovykin, 1970)	Mosaicism reported (Vdovykin, 1970), corresponds to shock stage S5-S6 (Stöffler et al., 1991).	Find (Vdovykin, 1970)
Kenna	Olivine ($Fo_{79.2}$), pigeonite ($En_{73}Wo_{9}Fs_{18}$), carbon, troilite	Rusting reported (Berkley et al., 1976)	Graphite, lonsdaleite, Diamond (Berkley et al., 1976)	Pressures of 50-250kbar reported (Berkley et al., 1976),	Find (Berkley et al., 1976)

	and nickel-iron metal (Berkley et al., 1976)			corresponds to shock stage S2-S4 (Stöffler et al., 2018).	
Hajmah	Olivine ($Fo_{84.5}$), clinopyroxene ($En_{85.7}Wo_{9}$ ($Fs_{5.3}$)) and carbon (Goodrich, 1992).	No weathering state reported, evidence of rusting shown in the results section.	Graphite, diamond (Ross et al., 2011).	Reported as high shock (Goodrich, 1992). Based on observations in the results section shock stage appears no higher than S3 (Stöffler et al., 2018).	Find (Graham, 1978)
Novo Urei	Olivine ($Fo_{78.9}$), clinopyroxene ($En_{72}Wo_{10.2}$ ($Fs_{17.8}$)), carbon and metal (Vdovykin, 1970).	No weathering state reported.	Graphite, diamond, lonsdaleite (Vdovykin, 1970).	Twinned clinopyroxene (see results section) indicates shock stage S4-S5 (Stöffler et al., 2018).	Fall (Vdovykin, 1970)

3.2 Sample preparation

In order to undertake microstructural analysis, the samples must be carefully prepared. For samples to be used for EBSD analysis they must be mechanically polished using 1 μm aluminium spheres suspended in glycol for 5 minutes, and then a further 5 minutes polishing via 0.3 μm aluminium spheres in glycol (Daly et al., 2019). After this a chemical polish using an NaOH colloidal silica suspension is used to remove any mechanical damage left behind by polishing, this will leave a surface that is completely free from mechanical damage which is required in order to produce Kikuchi patterns (Halfpenny, 2010). Any remnant mechanical damage will cause the patterns to be faint, and any data retrieved may reflect that damage rather than internal features of the sample. High quality Kikuchi patterns are crucial to minimise any issues with misindexing and misidentifying the mineral phases present (Prior et al., 2009). Prior to any high vacuum EBSD data collection the samples were coated in 7 nm of carbon. This is to reduce an effect called electron charging, which is where there is a build-up of negative charge on samples that have poor electrical conductivity, which would be many mineral samples (Halfpenny, 2010).

3.3 Optical microscopy

Optical microscopy in polarised light allows for quick characterisation of minerals and textural relationships present within samples (Gunter, 2004). This is not done automatically but based on the user comparing optical properties seen in the microscope with those that are

known for certain minerals, e.g. extinction angles and interference colours (Gunter, 2004). This technique is often used as a starting point in petrographic studies and can be very useful in combination with chemical studies as some minerals can have the same chemical composition picked up by other techniques but different optical properties e.g. kyanite and andalusite (Gunter, 2004).

An optical microscope contains a light source, a polariser and a lens. For plane polarised light the polariser is placed between the light source and the sample being analysed (placed on the stage) in order to focus the vibrations of the light into a single plane instead of being scattered in multiple directions (Gribble and Hall, 1985). Cross polarised light is achieved when the polariser concentrates the light into 2 planes at 90° from each other (Gribble and Hall, 1985). The lens is important in microscopy as it is responsible for bending the light into the eye piece and distorting the image into a higher magnification to allow for small details to be seen. The limit for the smallest details an optical microscope can pick out is generally around ~200 nm (Goodhew et al., 2000) depending on the exact microscope, this is due to the effect of diffraction and how the light had to bend to go through the eyepiece aperture. When light gets diffracted in an optical microscope it becomes rings of light and forms circles going through the aperture and the intensity of these light circles decreases with decreasing size, so anything below ~200 nm is not intense enough to be picked up (Goodhew et al., 2000).

Optical images for this study were obtained in both reflected and transmitted light by a Zeiss microscope at the Hunterian Museum research labs and at the University of Glasgow. The Hunterian Museum microscope was an Axioscope 5/7/vario with an Axiocam 208c camera. These images produced transmitted plane polarised and cross polarised light images, as well as reflected light images across all samples. The University of Glasgow microscope was a Zeiss Axio Imager 2 using the software Zen core 3.2.

3.4 Scanning electron microscopy imaging

Scanning Electron Microscopy (SEM) is a technique that is primarily used for obtaining 2D images of a sample at high spatial resolution (Reed, 2005). The SEM works in a similar way to the optical microscope but instead of the sample interacting with light beams, an electron beam is accelerated towards the sample (fig. 9). The sample usually must be held in chamber at high vacuum in order for the electrons to be able to travel as they can easily be scattered by the presence of gases, so the pressure usually has to be at least 10^{-10} Pa (Goodhew et al., 2000). Electromagnetic fields acts as the lens and bend the beam to produce the magnification effect, with negligible diffraction effect like the one seen in optical imagery (Goodhew et al., 2000). SEM images can provide higher magnification and resolution than standard optical imagery due to electrons having a smaller wavelength than visible light, so the diffraction effect is lessened (Goodhew et al., 2000). Due to this, the potential spatial resolution of electron microscopy is ~0.02 nm which is a significant improvement compared to standard optical microscopy (Goodhew et al., 2000). An SEM will capture secondary electrons (SE) which are emitted from a sample following bombardment of primary electrons, SE only come from the surface of the sample so provide information around surface topography based on their diffraction angles that can then be viewed as an image (Seiler, 1983). Backscatter electron (BSE) images are obtained by detecting the scattering of the incident (primary) electrons by the nucleus of the particles in the sample, the amount of electrons getting scattered increases with a higher atomic number so the contrast between light and dark patches in the image represents the distribution of light and heavy elements (Chen et al., 2015). BSE is particularly useful for distinguishing between phases whereas SE

shows the relief and topography (Chen et al., 2015). A diagram showing the interior of an SEM is provided in fig. 9.

The Zeiss Sigma Variable Pressure Field Emission Gun Scanning Electron Microscope (SEM) at the University of Glasgow ISAAC (Imaging Spectroscopy and Analysis Centre) was used to generate BSE and SE images across samples. These show high magnification of the surface features of the samples, such as grain boundaries, veins, and fractures.

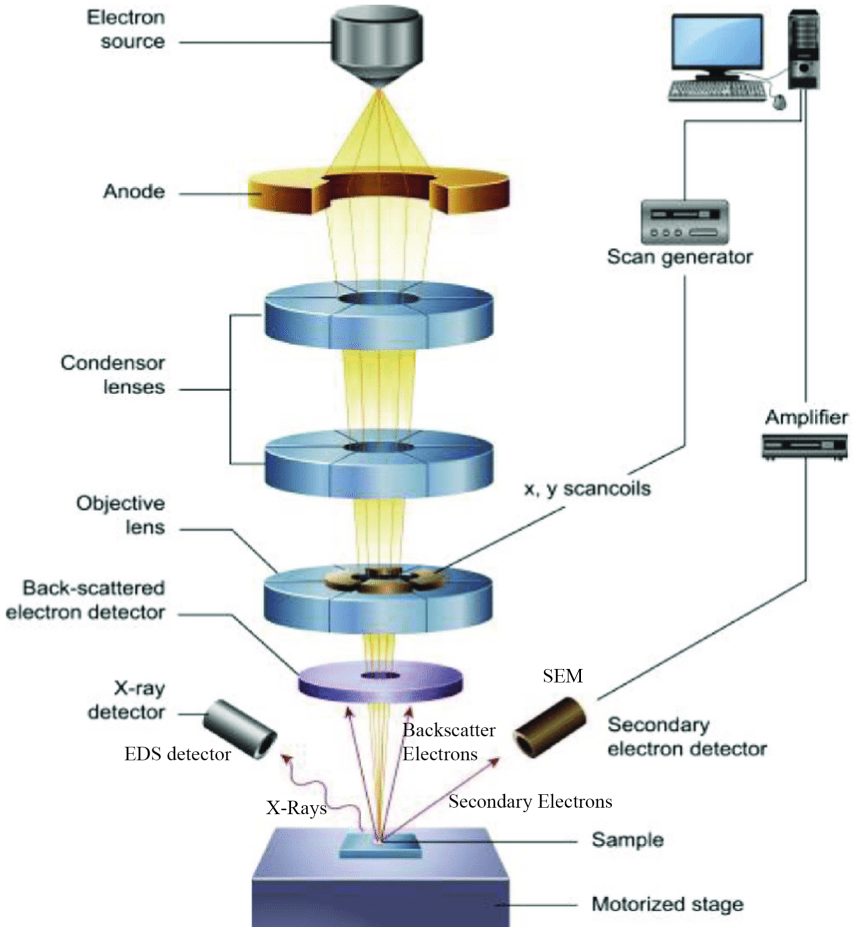

Figure 9: Cartoon schematic of SEM-EDS data acquisition, adapted from (Salman Ali, 2020)

3.5 Energy dispersive X-Ray Spectroscopy

Energy Dispersive X-Ray Spectroscopy (EDS) data can be acquired simultaneously with EBSD. This technique measures the abundance of major and minor elements present in the sample and can be mapped allowing for precise reconciliation between which phases host which elements (Wallis et al., 2019). EDS can support the EBSD data and enhance the data to allow for other analysis, for example EBSD of ureilite olivine crystals will not distinguish between the cores (Fe-rich) and the reduction rims (Fe-Poor) as they have the same crystal structure. Olivine crystals have the chemical formula $(Fe, Mg)_2SiO_4$ (Buening and Buseck, 1973) which arrange in an octahedral crystal lattice where Mg^{2+} and Fe^{2+} can freely substitute in for each other with minimal structural change due to similar ionic radii (de Hoog et al., 2010), so the EBSD detector recognises only the structure and not the chemistry. However, EDS maps will show the distribution of the Fe and Mg (Nolze et al., 2005) and when used in conjunction with EBSD allows the reduction rims to be distinguished from the core.

EDS involves an electron beam being fired at the sample which excites the outer shell electrons of atoms present in the sample (Colpan et al., 2018). These excited electrons move back to their ground state and emit X-rays with diagnostic energies which are then collected by the EDS detector (fig. 9) forming a spectrum that is then matched to a database of known spectra for different elements (Colpan et al., 2018; Ebnesajjad, 2014). Each element contains electrons at unique energy levels within their atomic structure, when electrons get excited, they jump up to a higher energy level and emit X-rays when they drop back down (Friel and Lyman, 2006). The intensity of the X-rays is dependent on how big that 'jump' is which allows for individual elements to be identified (Friel and Lyman, 2006).

EDS data was acquired using a Zeiss sigma variable pressure SEM at the ISAAC facility at the University of Glasgow. This was done to identify the chemical, mineralogical and structural characteristics of the sample. EDS produced false colour element maps across all samples, usually for elements magnesium, iron and carbon but some samples also show sulphur and/or chromium. The EDS false colour element maps were used for ImageJ analysis of the orientation of carbon veins in the sample MIL090980.

For the EDS full sample maps the thin sections were first coated with 10 nm of carbon. BSE images were collected after carbon coating using a Zeiss Sigma VP field emission gun (VP-FEG-SEM) operated at 20kV/2 nA and high vacuum. X-rays were then collected for 100 ms/pixel using an Oxford Instruments 80-mm^2 X-Max silicon drift detector energy dispersive spectrometer to gain the EDS chemical data. Spectra were then processed and analysed using Oxford Instruments Aztec and AztecFlex software.

Table 2: Summary table showing the surface area and resolution of the EDS maps for each sample.

Sample	Surface Area of EDS maps	Pixel Size/resolution
Hajmah	10.6 mm x 11 mm	1.50 μm
Goalpara (1)	5.96 mm x 7.94 mm	1.50 μm
Goalpara (2)	4.81 mm x6.82 mm	1.50 μm
Kenna	9.9 mm x 6.94 mm	1.00 μm
MIL090980	1.23 mm x 924 μm	1.20 μm
MIL090076	8.34 mm x 11.40 mm	1.20 μm

3.6 Electron Backscatter Diffraction (EBSD)

The EBSD data was collected using a Zeiss Sigma VP-FEGSM at high vacuum for two samples (Goalpara and Kenna), which had first been coated with 7nm of carbon in order to avoid charging the sample. Due to the requirement to collect correlated Raman spectra and SEM images, EBSD data from MIL090980 was collected at variable pressure of 49Pa to negate the need to keep applying and removing a carbon coat and additional polishing. During the data collection the samples were tilted to 70° (fig. 10) which is the standard angle for EBSD data collection. EBSD was collected using an Oxford Instruments NordlysMax^2 EBSD detector using an accelerating voltage of 20kV a beam current of 4.1 nA and the automated Large Area Mapping module in Oxford Instruments Aztec software.

The main analytical technique used in this thesis is EBSD. This is done using a SEM. The SEM fires electrons at a sample, tilted to 70° to allow the electron beam to be channelled along crystal lattice planes and not dispersed (Prior et al., 2009). The diffraction of these electrons generates Kikuchi patterns, these are the patterns produced when electrons are channelled along lattice planes and after leaving the crystal surface get detected on a phosphor screen (fig. 10) and produces the pattern (Winkelmann et al., 2020). This can then be matched to a database of known patterns from known minerals or crystalline materials. The beam is then rastered across a sample and analysed to create a map of the sample (Wallis et al., 2019). This technique allows for textural and mineralogical data to be obtained from crystalline portions of a sample.

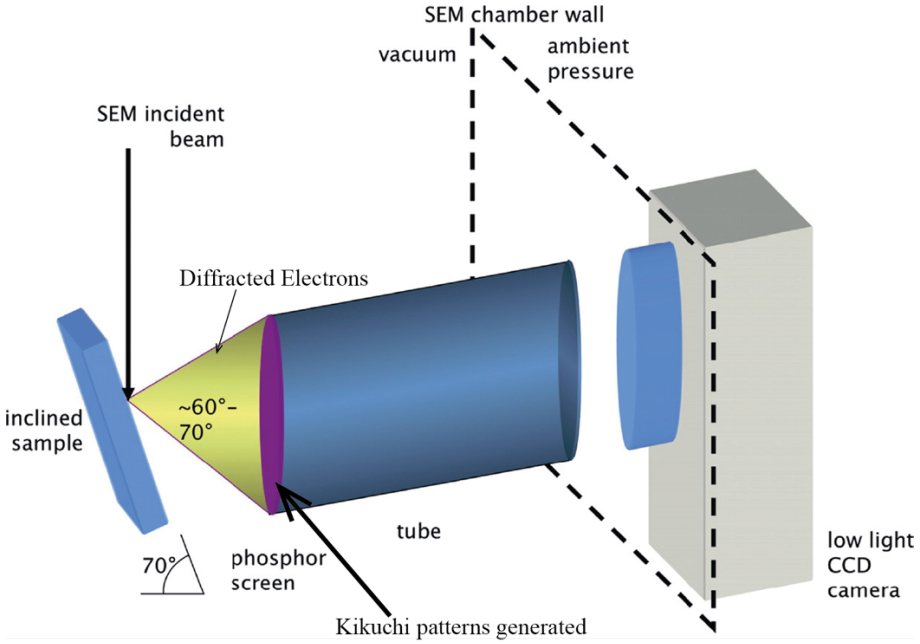

Figure 10: Cartoon schematic of an EBSD detector, adapted from (Wilkinson and Britton, 2012).

EBSD can characterise any crystalline material and record distortions and deformation of the crystal lattice in a way that allows for them to be quantified (Wallis et al., 2019).

Olivine and pyroxene have well-defined microstructural responses to shock that correspond to specific pressures and temperatures (Stöffler et al., 2018). Many of these features, such as mechanical twinning and planar deformation features can be identified using EBSD and then matched to a certain shock pressure to define the conditions of an impact (Stöffler et al., 2018). Olivine has also been studied through EBSD previously to characterise the different creep regimes present throughout the different layers of the Earth, as olivine is the most abundant mineral in the mantle (Prior et al., 2009). Other deformation that can be measured using EBSD includes subgrain rotation during recrystallisation, and models of how this process works are based on measurements taken from olivine (Prior et al., 2009). Another important and useful application of EBSD involves characterising mineral reaction processes and associated microstructures that can occur at distinct metamorphic grades, as well as the thermal histories for meteorites in particular (Prior et al., 2009).

EBSD data was acquired using a Zeiss sigma variable pressure SEM at the ISAAC facility at the University of Glasgow. EBSD data was used to generate Inverse Pole Figure (IPF) maps which show the relationships between crystals and whether there is any preferred alignment.

EBSD data also generated GROD (Grain Reference Orientation Deviation)-angle maps which show the zones of deformation across the samples and the distributed of deformation. Pole figures were generated using the 1 point per crystallite feature in AztecCrystal for anything the software identified as a single crystal that was larger than 100 pixels.

Olivine Crystal Preferred Orientations (CPOs) can be determined from pole figures of EBSD data (Karato et al., 2008). They reflect the density of crystallographic orientations of olivine grains across the sample or for user-defined subsets, this can show whether they have any common preferred orientation and form random, planar or linear fabrics. A random fabric (fig. 11) is one where there is very little preferred orientation or alignment between individual crystals, a linear fabric is one that shows alignment along a line such as a lineation fabric (fig. 11) whereas a planar fabric is an alignment that is dispersed along a great circle such as a foliation (fig, 11). In addition, it is also possible to extract slip system information from crystal rotation axis diagrams. These reveal which specific slip systems in olivine has been activated during deformation, some of which have been paired with specific conditions of deformation (Karato et al., 2008).

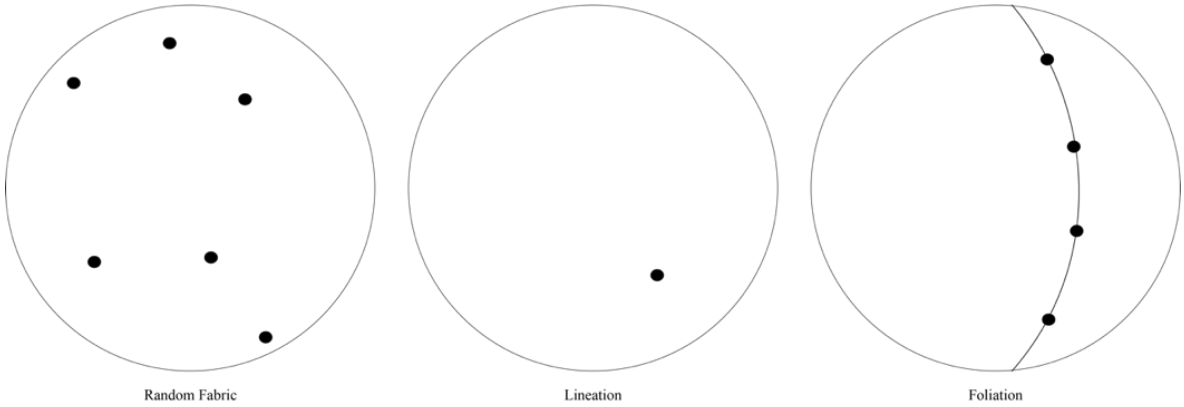

Figure 11: Example schematic of different fabrics displayed on a stereonet. The black dots are example data points and the line is a great circle.

Table 3: Summary table showing some key acquisition settings for the EBSD maps for each sample.

Sample Map	Step Size (μm)	Dwell Time Per Pixel	Kikuchi Pattern Binning
Goalpara USNM 1545-1	2.1	35 μs	4x4
MIL090980 (10,3 NASA Johnson Space Centre)	3	35 μs	4x4
Kenna L6105 NHM Wein	4	35 μs	4x4

3.7 Electron Probe Micro Analysis

Electron Probe Micro Analysis (EPMA) is a technique that enables the chemical composition of chosen points in a sample to be quantified. A fine (<1 μm (Weiss et al., 2008)) electron beam is fired onto the surface of the sample (fig. 12). The area of the sample that is affected then emits X-rays (Weiss et al., 2008), like EDS, which then produce a spectrum on the

detector that can then be analysed and matched to known spectra of different elements and their abundance can also be calculated (Weiss et al., 2008). A diagram of this process is shown in fig. 12.

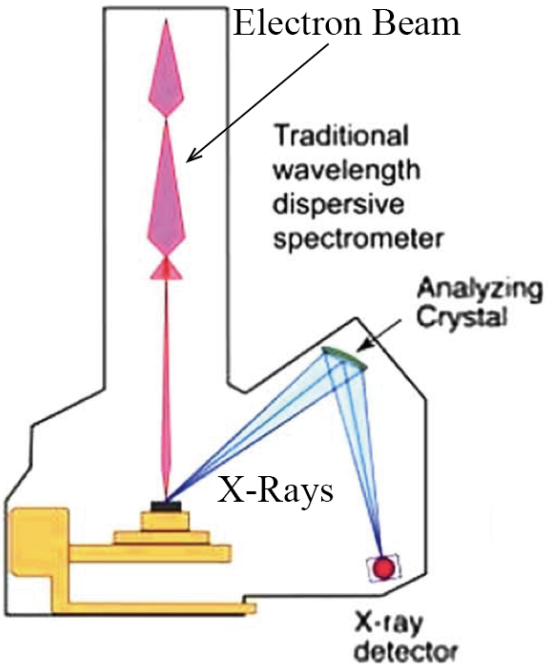

Figure 12: Cartoon schematic of a simplified EPMA detection, adapted from(Rinaldi and Llovet, 2015).

Electron probe microanalysis (EPMA) was conducted on the JEOL-JXA 8530F EPMA at the Smithsonian Institute, Washington, USA. EPMA point spectra were collected with an accelerating voltage of 15kV and a beam current of 69µA. This was a focus beam as such the spot size is a nominal diameter of 0 µm. The interaction volume where the signal was acquired is likely 1 μm^3. Elements collected were Fe, Ca, Ti, Mn, Ni, Cr, Si, Al, Mg, Na, S, P, K and O. Oxygen data was collected via stoichiometry. Detection limits, standards and % error for the elements collected is provided in Table 4.

The EPMA data was used to plot olivine Fe vs Mg composition plots, Ca-Mg-Fe ternary plots for pyroxene composition and Total Alkali Silica plots to show how evolved the composition is.

Table 4: Summary table of the elements collected via EPMA with the collection specifications of detection limits, % error and the minerals used as standards.

Element Collected	Detection Limits (wt %)	Standards Used	% Error
Iron (Fe)	0.03	Troilite	1.89
Calcium (Ca)	0.01	Diopside (NY USNM 11733)	2.57
Titanium (Ti)	0.03	Ilmenite (USNM 96189)	32.11
Manganese (Mn)	0.03	Manganite (USNM 114887)	19.20
Nickel (Ni)	0.03	Nickel Metal	34.86
Chromium (Cr)	0.02	Chromite (USNM 117075)	19.87
Silicon (Si)	0.01	Anorthoclase (Kaknui USNM 133868)	1.28
Aluminium (Al)	0.01	Bytownite (Crystal bay USNM R-2912)	8.24
Magnesium (Mg)	0.01	Olivine Fo90 (USNM 111312/444 San Carlos)	4.77
Sodium (Na)	0.01	Anorthoclase (Kakanui USNM 133868)	13.61
Sulphur (S)	0.01	Troilite	39.21
Phosphorus (P)	0.01	Fluor-apatite (USNM 104021)	39.41
Potassium (K)	0.01	Anorthoclase (Kakanui USNM 133868)	23.12

3.8 Raman Spectroscopy

Raman spectroscopy is a technique that can be used to identify different materials contained within a sample and their molecular structure. This technique gives the vibrational signature of a sample based on the chemistry and bond length (Das and Agrawal, 2011). Raman spectroscopy measures how radiation affects molecular vibrations and the transfer of photon energy between vibrational states (Larkin, 2011). A Raman spectrometer is composed of 4 key parts (shown in fig. 13): the light source, monochromator, sample holder and detector (Das and Agrawal, 2011).

A monochromatic laser is fired at the sample which interacts with the molecular vibrations of the system resulting in a shift in the energy of the photons emitted by the laser. It operates based on the Raman principle, also known as inelastic scattering, which records the scattering of the protons that are fired at the sample. The Raman effect is the shift in the wavelength of radiation scattered by molecules which has a different frequency than the incident beam (Das and Agrawal, 2011). Each molecule, or mineral, has its own distinctive Raman fingerprint which is represented by the vibrational energy levels (Larkin, 2011) that get recorded as

Raman shift peaks. As the Raman frequencies are dependent on the atomic mass, geometric arrangement and strength of the chemical bonds (Larkin, 2011) different allotropes of the same base chemistry can be identified such as graphite and diamond.

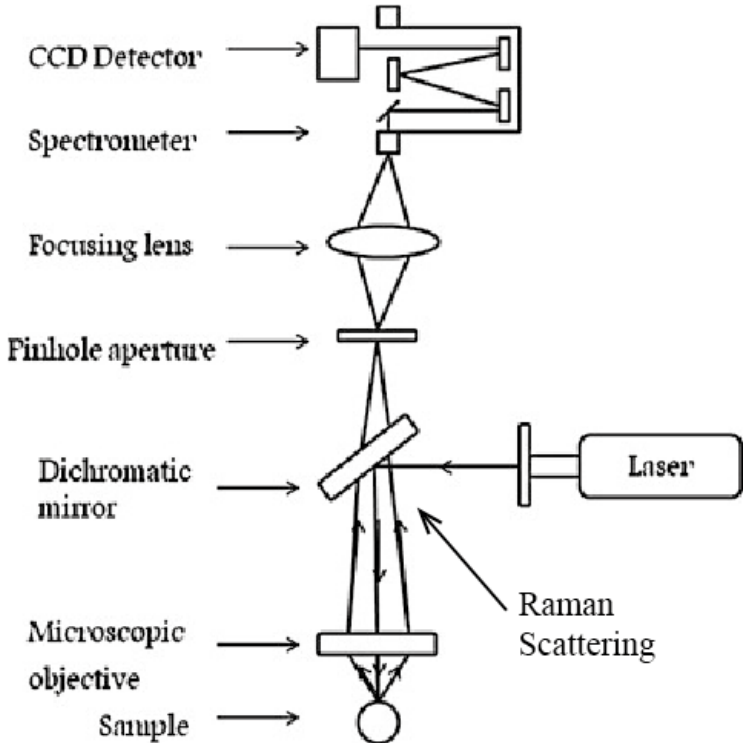

Figure 13: Cartoon schematic of Raman spectroscopy. Adapted from (Das and Agrawal, 2011)

Raman spectroscopy is non-destructive of the material being studied making it a prime technique for analysing precious and rare materials (Das and Agrawal, 2011), such as meteorites.

Raman data was acquired using a Renishaw InVia Raman microscope attached to a 45W (max power), 512 nm laser source and a 2400 mm grating. Mapping analysis was carried out using a laser power of 5% with a 3 second exposure time. The Raman data was then used to map the locations of graphite and diamond across various locations in a carbon rich zone of MIL090980. The data was also used to plot full width half maximum (FWHM) vs Raman shift plots for the diamond. The FWHM value is the width of the Raman peak at half the value, this figure is used to determine the crystallinity of diamonds and graphite (Miyamoto et al., 1993).

3.9 Modal Mineralogy

Modal mineralogy was measured using a 10x10 grid overlay on a RGB false colour image showing magnesium, carbon and iron for each sample. The minerals were counted based on which was dominant in each square to get an estimated percentage of the modal mineralogy.

4.0 Results

This results section is structured in such a way each sample is presented and described individually, before being discussed as a whole suite later. Each sample is split into the

different techniques that were used on each one to fully describe all data that was generated for this study.

Table 5: A table showing the modal mineralogy of each sample where SEM-EDS data was collected.

Sample	Modal Mineralogy			
	Olivine	**Pyroxene**	**Carbon**	**Iron**
Hajmah	62.7%	22.9%	7.2%	7.2%
Goalpara	72.2%	2.5%	12.7%	12.7%
Kenna	59.6%	25.3%	9.1%	6.1%
MIL090980	46.0%	31.6%	14.3%	8.2%
MIL090076	57.1%	17.9%	15.5%	9.5%

4.1 Hajmah

4.1.1 Optical images

Optical images of Hajmah, seen in fig. 14 show a brown colouration to the veins which reflects a degree of terrestrial weathering and alteration of the iron-rich components due to this being a find rather than an observed fall.

The grain size of Hajmah is fairly uniform a medium-coarse grained (0.5 mm to ~4 mm), the XPL image, in particular fig. 14c shows grains up to 4 mm in size. Hajmah also contains 22.9% pyroxene seen as the light blue (low first order birefringence colour) crystals in XPL in fig.14c but the sample overall is olivine dominated with 62.7% Olivine. Hajmah is one of the most olivine dominated of the samples studied as it contains the second highest percentage of olivine, seen in table 5. Both the olivine and the pyroxene crystals are subhedral in habit, the pyroxene tends to be more sub-rounded whereas the olivine is more sub-angular in shape (fig. 14b & c). The black vein material is the carbon dominated matrix which is cutting into the silicate minerals (fig. 14b & c). In some areas the carbon is concentrated into sub-spherical accumulations around grain boundaries, some of these carbon regions also appear to be cutting into the silicate crystals and eating into their outer surfaces, this is especially noticeable in the PPL and XPL optical images shown in fig. 14b and c. Pyroxene grains contain higher density of fractures compared to the olivine crystals seen in fig. 14 a and b.

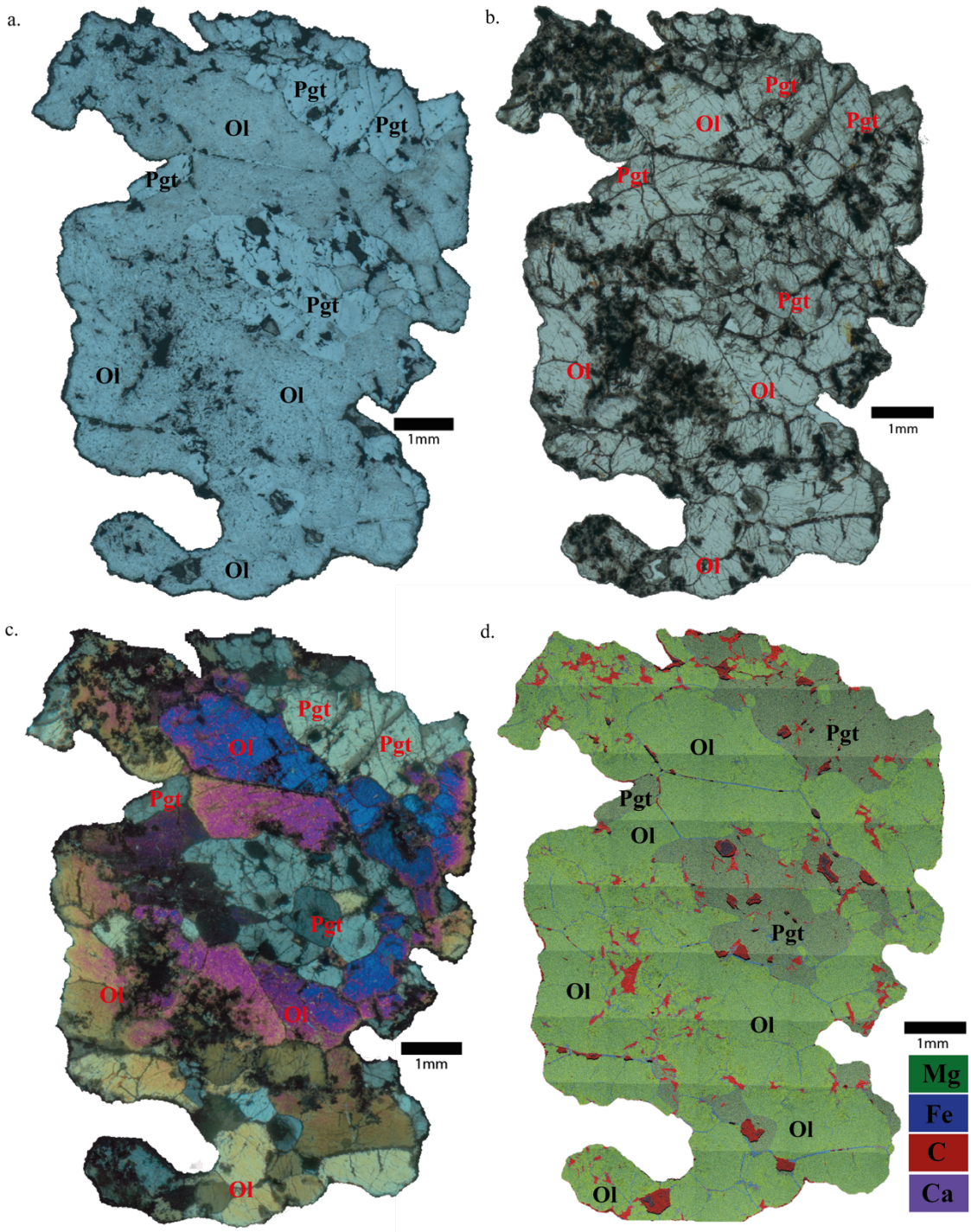

Figure 14: Optical microscopy and SEM-EDS images from Hajmah including a. Reflected light, b. transmitted PPL (Plane Polarised Light) and c. XPL (Cross Polarised Light) and d. A false colour EDS map of Hajmah, this shows magnesium in green; iron in blue; carbon in red; and calcium in purple. Throughout the rest of the results section the false colour images of samples include the electron image in white, however this was removed for Hajmah as the carbon and iron were harder to distinguish with an electron image. Annotations of the main minerals have been added to the images using approved mineral abbreviations from (Whitney and Evans, 2010), ol is olivine and pgt is pigeonite which is the assumed pyroxene mineral for the ureilites based on review from (Goodrich, 1992).

4.1.2 SEM-EDS Data

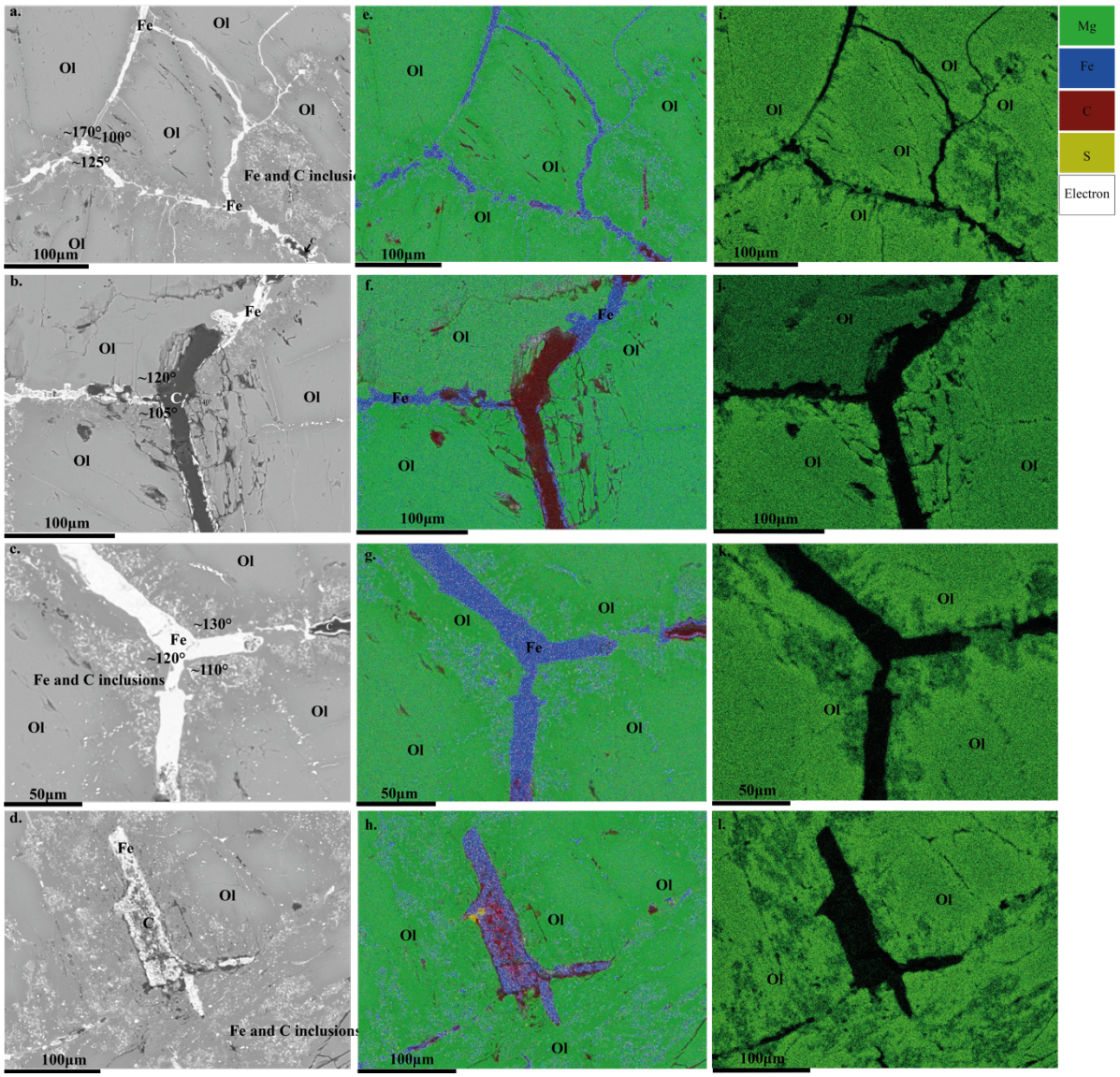

Figure 15: Backscatter Electron images of grain boundaries and vein structures within Hajmah. a. shows a 120° triple junction boundary with some metal inclusions in the rims of the neighbouring olivines, iron metal makes up the majority of the vein emplaced along this boundary; b. shows another 120° triple junction boundary where carbon makes up the majority of the vein; c. shows a 120° triple junction boundary with iron but the vein hasn't permeated fully through the silicate and is cut off; d. shows a concentration of carbon and iron. e-h show false colour EDS maps of the same areas showing carbon in red, magnesium in green, iron in blue and sulphur in yellow. This is to highlight the chemical relationships within the veins. i-l show EDS maps of magnesium content variations around olivine grain boundaries. Reduction rims are observed at olivine grain edges evidenced by an enrichment in Mg and Fe metal blebs closer to the veins/inclusions.

BSE images from Hajmah showed clear granoblastic texture with 120° triple junctions at olivine grain boundaries (fig. 15a-c). Reduction rims are present around olivine, especially in areas where iron is concentrated into veins surrounding the grains (fig. 14d & fig. 15). Within the olivine grains rims in contact with the vein there appear to be some metallic inclusions,

shown in the bright features in BSE images around the main vein (fig. 15, c & d). This is a common occurrence in the majority of grain boundaries (fig. 15 a, c & d).
Every boundary between silicate mineral grains contains iron and/or carbon creating veins seen in fig. 14. The EDS and BSE maps (fig. 15) also show that there are iron metal grains within the silicate crystals that are concentrated at the boundary between the veins and the silicate the concentration of Fe in EDS images matches the bright phases observed in BSE images (fig. 15).

Mg EDS maps of the same areas in fig. 15i-l show a general enrichment in Mg around the grain boundaries of the olivine crystals, seen in the brighter green colour and corresponding depletions in the olivine rim areas where Fe blebs are concentrated. This is noted when comparing fig. 15i-l with the BSE images in fig. 15 a-d which shows the Fe blebs concentrating.

4.2 Goalpara

Two Goalpara samples were used for this study. EDS data and SEM imaging was acquired for both but only USNM 1545-1 was examined with optical and EBSD techniques due to time constraints and access to equipment.

4.2.1 Optical Images

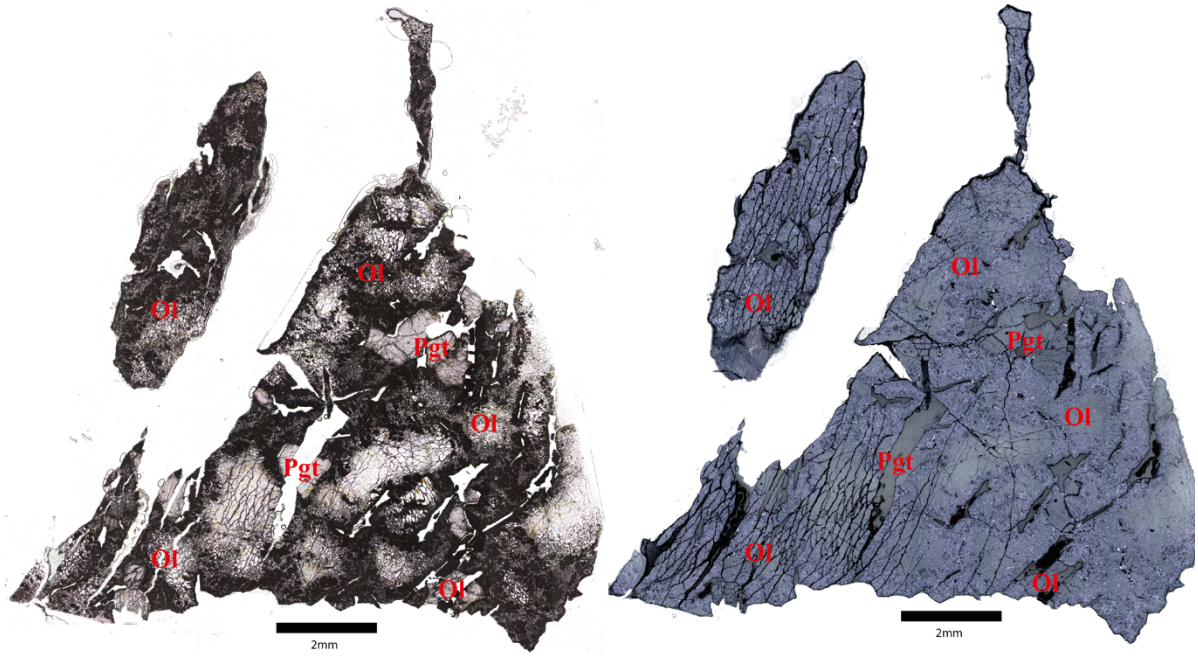

Figure 16: Optical image data of Goalpara 1545 in plane polarised and reflected light. Annotations of the main minerals have been added to the images using approved mineral abbreviations from (Whitney and Evans, 2010), ol is olivine and pgt is pigeonite which is the assumed pyroxene mineral for the ureilites based on review from (Goodrich, 1992).

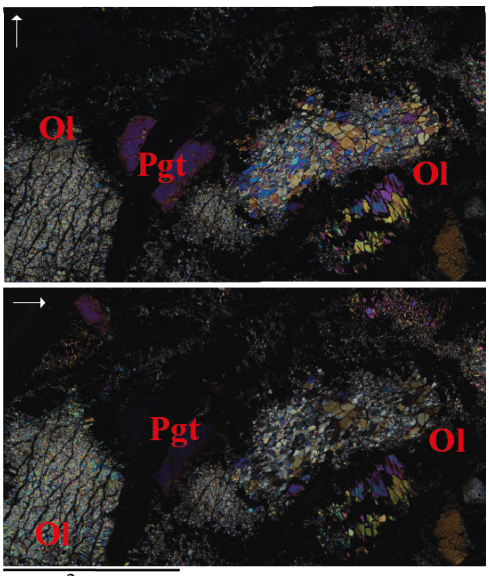

Figure 17: Optical images of Goalpara 1545 in transmitted cross polarised light. The two images show a rotation of 90° relative to each other. Shown in image is the mosaicism present within the olivine grains, shown as different subgrains having different interference colours. Annotations of the main minerals have been added to the images using approved mineral abbreviations from (Whitney and Evans, 2010), ol is olivine and pgt is pigeonite which is the assumed pyroxene mineral for the ureilites based on review from (Goodrich, 1992).

The optical images of Goalpara show multiple small grains of olivine (~0.1 mm maximum) in the cross polarised light in fig. 17, multiple colours are seen which suggests small grains that have slightly different orientations to the polarised light. The subgrains have a mottled appearance, seen especially in the top image of fig. 17 where a single subgrain is showing a range of colours. The small grains are grouped together and surrounded by a thick (~0.5 mm wide) black matrix. This matrix has the same appearance to other grain boundary material seen in other ureilites e.g. Hajmah (fig. 14a), suggesting this was the original grain boundary surrounding a previously coarse grain (up to 4 mm, inferred from the original grain boundary) that has since been subdivided into multiple fine grains that are sub-millimetre in scale (fig. 16 & 17). These small grains are considered individual subgrains as they can be seen in XPL to go extinct individually instead of at the same time as would be expected for one cohesive olivine crystal (fig. 17). The pyroxene crystals are more euhedral than the olivine as they approach the equant shape and are more well-formed than the olivine grains which tend to be elongate and subhedral (fig. 16). The pyroxene shows some fracturing but otherwise very little evidence of deformation in optical images. The pyroxene crystals are of higher relief than the olivine and contain metallic inclusions (fig. 16 & 18). There is also one well developed cleavage seen in the pyroxene, with some crystals showing a weakly developed second cleavage intersecting the first at 90 ° (fig. 18a).

Goalpara is very olivine dominated (72.2% compared to 2.5% (Table 5). Thick carbon veins are present around the silicate minerals up to ~2 mm thick but they are also unevenly distributed and the thickest sections are where they have cut into the minerals.

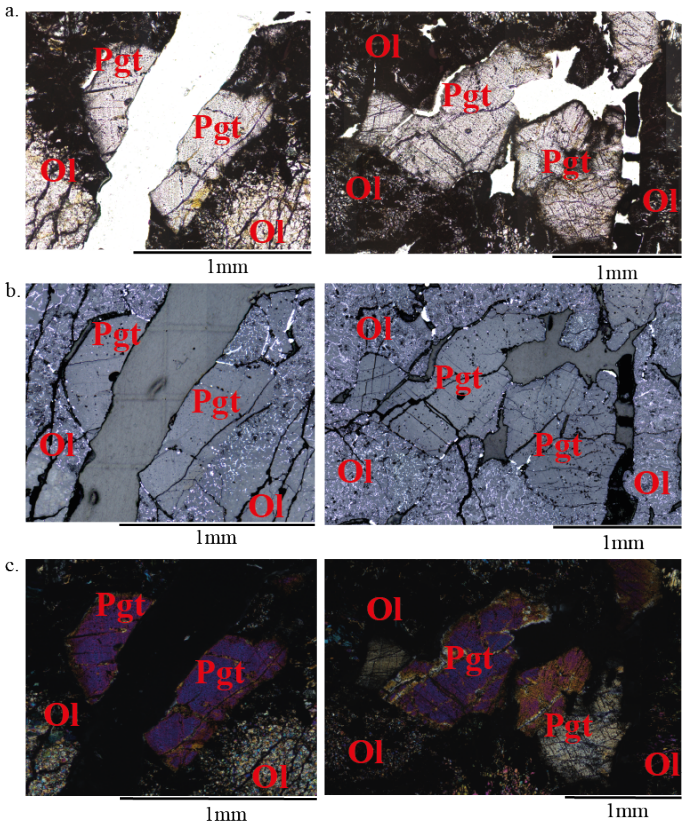

Figure 18: Optical images of two pyroxene grains within Goalpara; a. shows both grains in transmitted plane polarised light; b. shows them in reflected light; and c. shows the two grains in transmitted cross polarised light. These images show the fracturing present in the pyroxene crystals, and the fact that they are not divided into smaller grains like the olivine are. Annotations of the main minerals have been added to the images using approved mineral abbreviations from (Whitney and Evans, 2010), ol is olivine and pgt is pigeonite which is the assumed pyroxene mineral for the ureilites based on review from (Goodrich, 1992).

4.2.2 SEM-EDS Data

EDS data of Goalpara displays dissemination of elements throughout crystals, rather than elements such as iron being restricted to the edges of crystals like in Hajmah. However, the olivine grains are polycrystalline and comprises of many subgrains and subgrain boundaries. These subgrain boundaries are seen to concentrate iron (fig. 19 & 20).

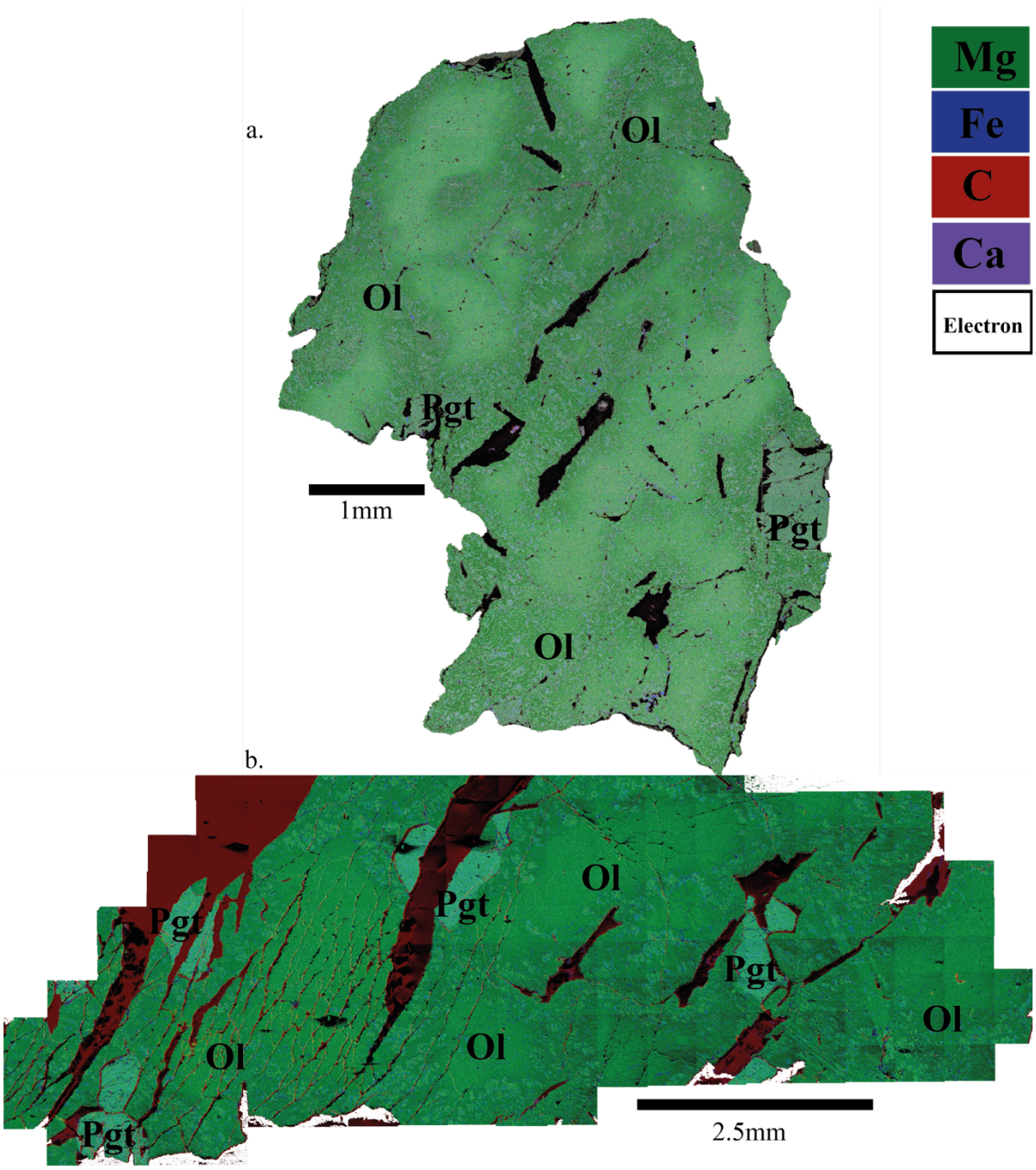

Figure 19: EDS false colour maps of Goalpara. Magnesium green, iron blue, carbon red and calcium in purple. Two sections of Goalpara were analysed through this technique, a. this is the sample referred to in table 2 as Goalpara (1). b. is sample USNM 1545-1, referred to in table 2 as Goalpara (2) which was further analysed by EBSD due to the fractures seen in the bottom left, seen here and in the EBSD figure below (fig. 21). Annotations of the main minerals have been added to the images using approved mineral abbreviations from (Whitney and Evans, 2010), ol is olivine and pgt is pigeonite which is the assumed pyroxene mineral for the ureilites based on review from (Goodrich, 1992).

The iron and chromium is seen in fig. 20 to concentrate in veins along fractures and grain boundaries, but also in metal rich zones creating a mottled appearance to the SEM-EDS images.

The images of the mosaicised grain boundaries, fig. 20c & e, show the iron in particular being concentrated along these boundaries. Fig. 20 b & d show that chromium is also concentrated along these boundaries indicating a variety of metallic grains and oxides present in these areas.

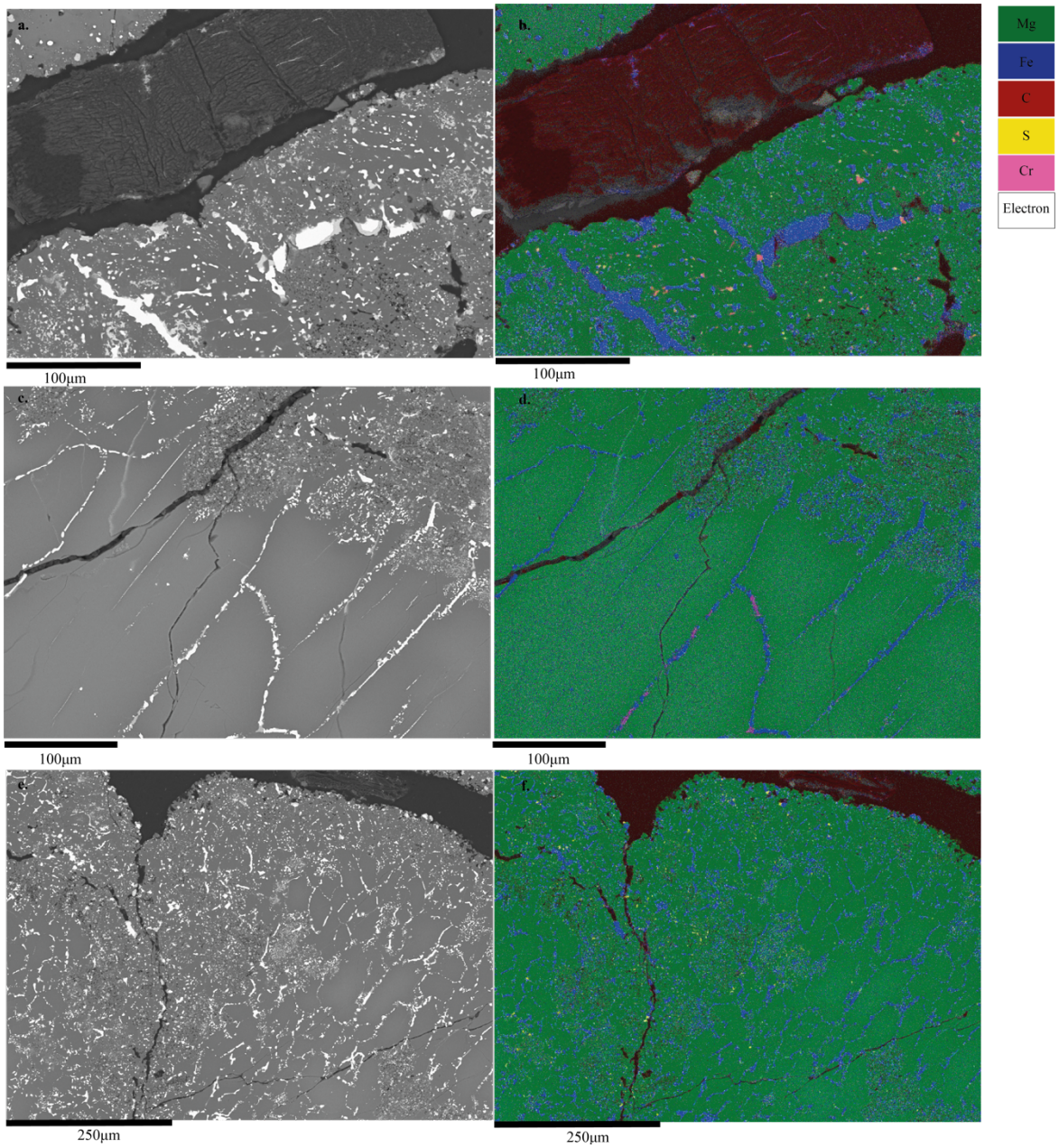

Figure 20: BSE and false colour EDS maps from within Goalpara USNM 1545-1; a. shows the BSE image of a fibrous vein; b. shows the false colour EDS map where magnesium is green, iron is blue, carbon is red, chromium is pink, and sulphur is yellow. This area is located in the bottom left of the section near the fractures. c. shows the BSE image of within an olivine rich section where the subgrains boundaries are decorated by bright white iron-metal blebs; and d. shows the false colour EDS image where magnesium is green, iron is blue, carbon is red and chromium is in pink. e. BSE image of another region showing iron-metal blebs decorating subgrain boundaries f. False colour EDS image of the interior of another mosaicised grain in Goalpara. Magnesium is green, iron is blue, carbon is red and sulphur is yellow.

Fig. 20 a & b show the interior of a vein structure within Goalpara, in the area of the fractures. This shows a platy or fibrous texture to the carbon that has formed a polycrystalline aggregate in this region.

4.2.3 EBSD Data

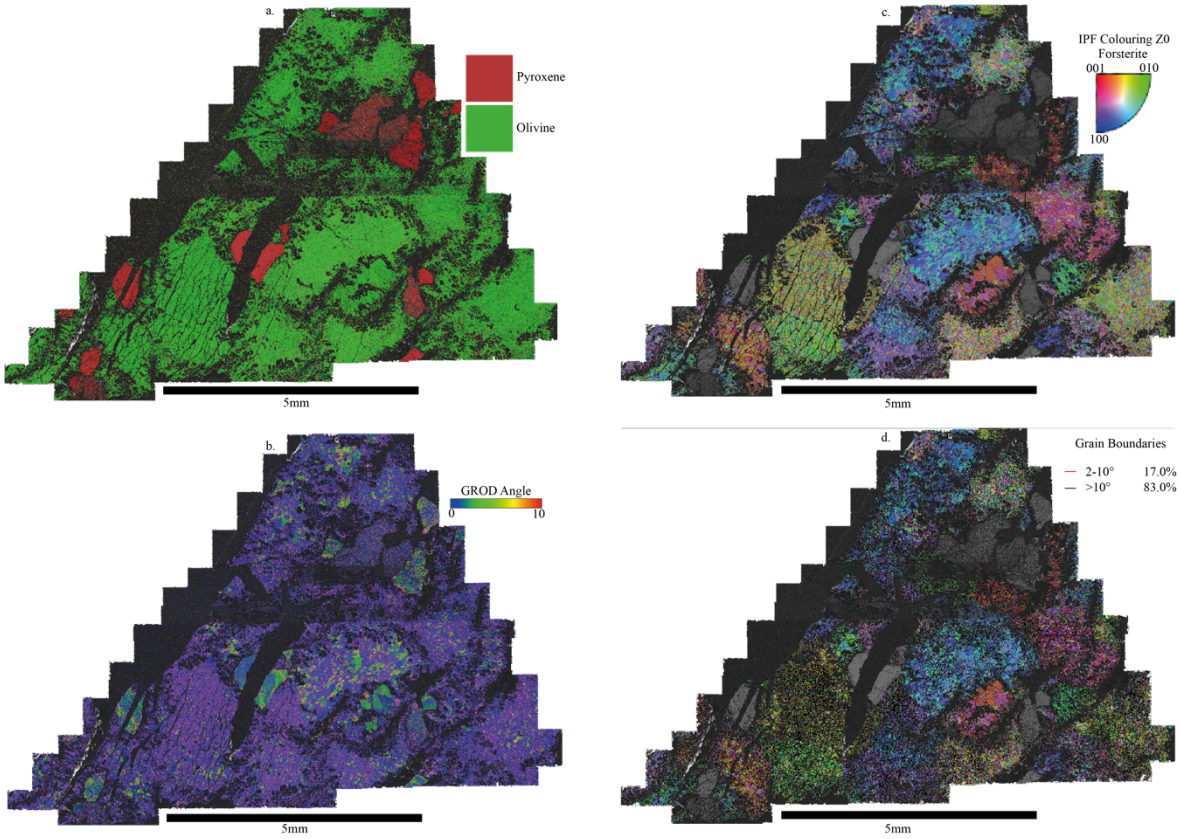

Figure 21: Goalpara. a. EBSD phase map across the sample showing the major phases present. Olivine is green and pyroxene is red, no other major phases were detected by EBSD. b. EBSD GROD-angle map showing deformation across grains. GROD angle maps take the average orientation seen across a whole grain and then highlight which areas deviate from this average (Griffin et al., 2022a). Blue areas show no deviation and therefore no evidence of plastic deformation, whereas red areas show the highest deviation in this figure the highest shown in 10° deviation as any more than this would be considered a grain boundary. c. EBSD image showing the Inverse Pole Figure (IPF) orientations of the crystals, crystals are coloured relative to the maps z-axis. Only the olivine (forsterite) is shown, the grey grains are pyroxene. d. shows the same IPF map but with the grain boundaries overlain. Any boundary over 10° is black and between 2-10° is red.

The phase map seen in fig. 21a shows that Goalpara has a higher proportion of olivine than pyroxene, which is typical of ureilite compositions. Goalpara is listed in table 5 containing 72.2% olivine, 2.5% pyroxene, 12.7% carbon and 12.7% iron which is the lowest amount of pyroxene in any of the samples used in this study.

The Inverse Pole Figure map (IPF) shown in fig. 21c highlights the mosaicism as each larger olivine grain is subdivided into several smaller grains that all have a slightly different

orientation seen through the IPF colouring. Fig. 21d shows the grain boundary angles. The majority of boundaries are over 10° which signifies at least a 10° angle between the crystal structure of each adjoining grain.

Each olivine crystal contains subgrains that exhibit slightly different colours in the IPF map in fig. 21c which indicates whilst each grain was completely recrystallised. The subgrains contained within each crystal oriented towards the same miller indices relative to the Z direction of this section, e.g. the majority blue grains were all oriented to {100} whereas the red grains were all oriented to {001}. There are some overall grains that contain subgrains in different directions but the majority appear to have been deformed as a whole unit due to each whole grain being generally the same colour. However, despite all being the same colour (e.g. blue) the individual subgrains are not all the same shade which shows they are not all exactly oriented the same way within the overall grain. Original grain boundaries are likely preserved despite heavy recrystallisation due to the presence of the same carbon/iron veins (up to 0.5 mm thick) seen in other samples (e.g. Hajmah fig. 14 & 15) which surround overall crystals seen in fig. 20. These veins clearly cut into what was originally a grain boundary and is seen to replace whole subgrains close to the grain boundaries (fig. 20).

The IPF map seen in fig. 21c shows the subgrains can be up to several microns (~3 μm) across but they are on average a lot smaller than this (~0.5-1 μm). The larger subgrains can also be seen to meet other larger subgrains at triple junctions of ~120° reminiscent of 'typical' ureilite texture.

The GROD-angle map in fig. 21b shows the large olivine grains do not tend to show a large degree of deformation, this is contained within each individual subgrain within the larger crystals but is very heterogeneous across the sample. The pyroxene crystals, identified in fig. 21a, tend to record deformation across the grains up to 10° deviation from the average.

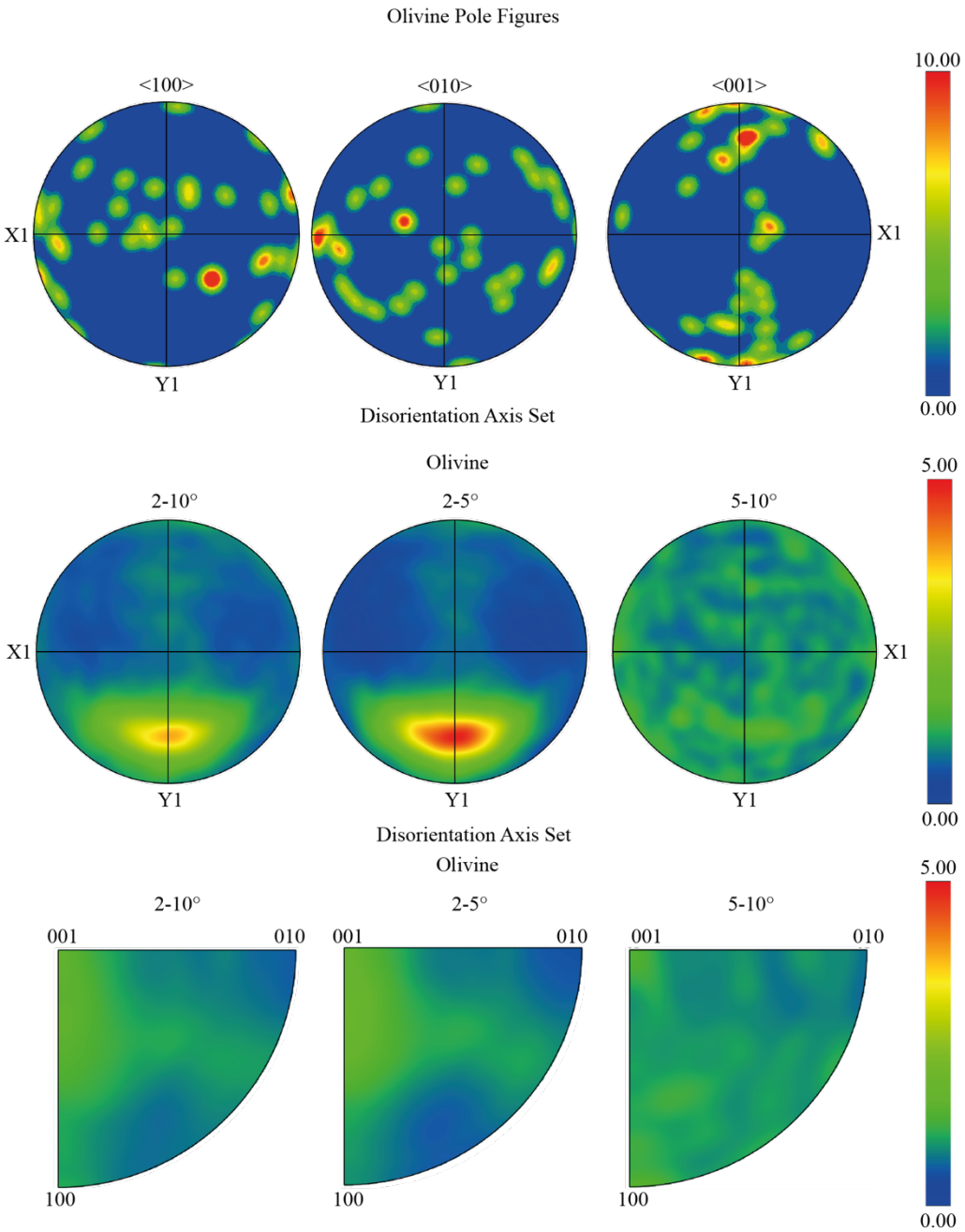

Figure 22: Pole figures of the olivine crystals within Goalpara USNM1545-1 for directions 100, 010 and 001. These figures were plotted with a 10° half width. Disorientation axis plots for the crystal coordinates of the olivine within Goalpara USNM1545-1. These are plotted with a 10° half width. Disorientation axis plot showing the sample coordinates for the sample Goalpara USNM 1545-1. 32 grains were included in this data set.

Evidence of a foliation present within Goalpara is shown in the pole figures in fig. 22 where there is no clear point in any miller indices, but instead a girdle across each of them.

One crystal, seen in fig. 23a, showed a cruciform pattern in the <100> axis of the diagrams which is reminiscent of pole figures reported for high pressure phase changes, similar to those between zircon to baddeleyite (Timms et al., 2017).

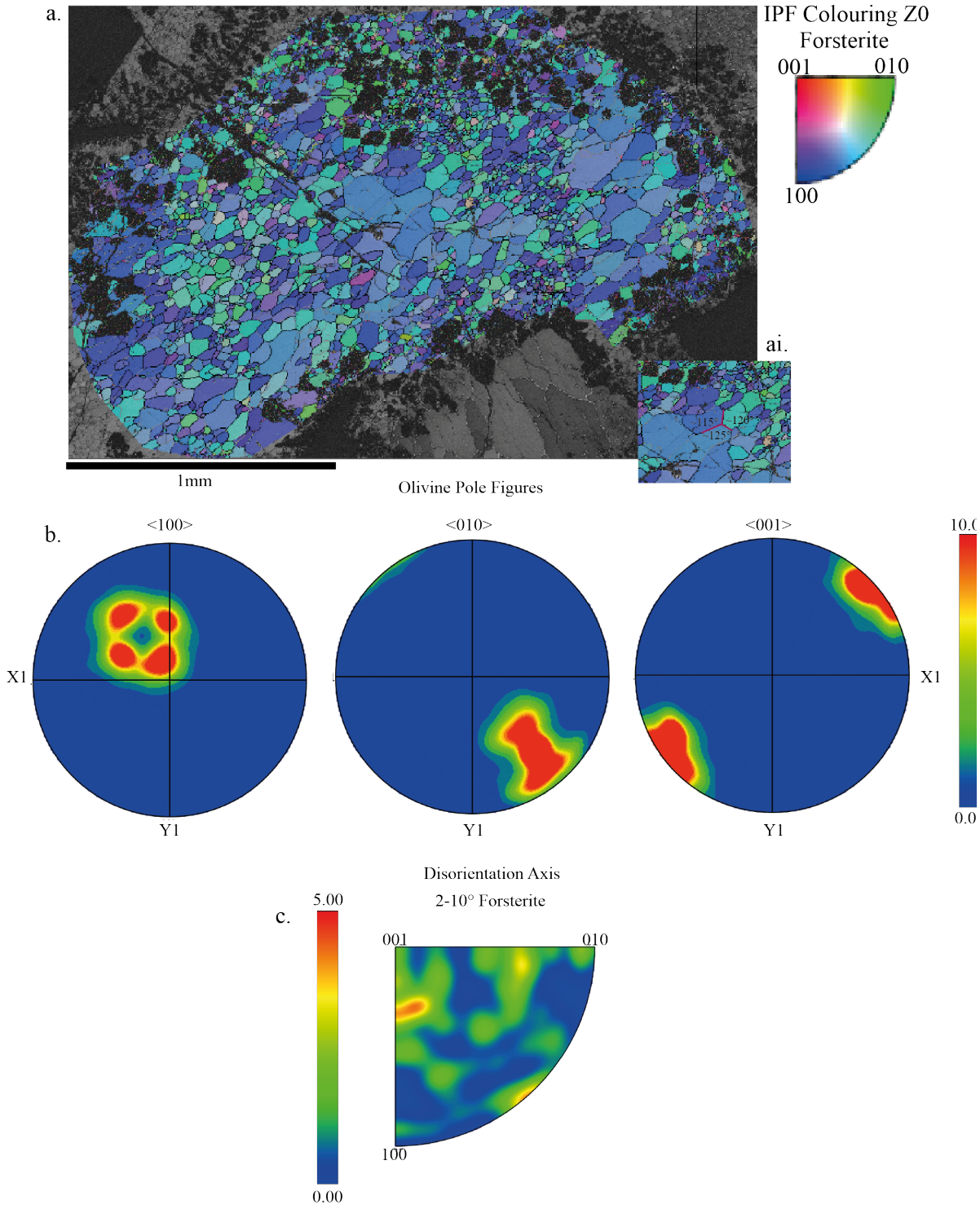

Figure 23: a. An EBSD IPF map of a selected grain within Goalpara USNM1545-1. This shows the different orientations of the subgrains within the mosaicised olivine crystal. Adjacent to this is ai. which shows a cropped version of the same grain at the same scale with annotations highlighting triple boundaries between the grains, b. shows the pole figure plots for the directions 100, 010 and 001 for the subset of the grain. Note the cruciform pattern in <100>, c. shows the disorientation axis and weighted burgess vector plots showing the crystal coordinates for olivine within the mosaicised grain.

4.3 Kenna

4.3.1 Optical Images

Kenna has veins that have a brown/red discolouration like Hajmah in optical microscopy, this is again an effect of terrestrial alteration. This sample is also olivine dominated (59.6%) but has a higher proportion of pyroxene (25.3%) when compared to the other samples in table 5.

The olivine crystals tend to be equant and euhedral to sub-hedral in shape up to 2.5 mm in length (fig. 24b-d). The grain boundaries meet in ~120° triple junctions between olivine crystals with major reduction and alteration in the zones adjacent to carbon veins in particular, fig. 24 a-d.

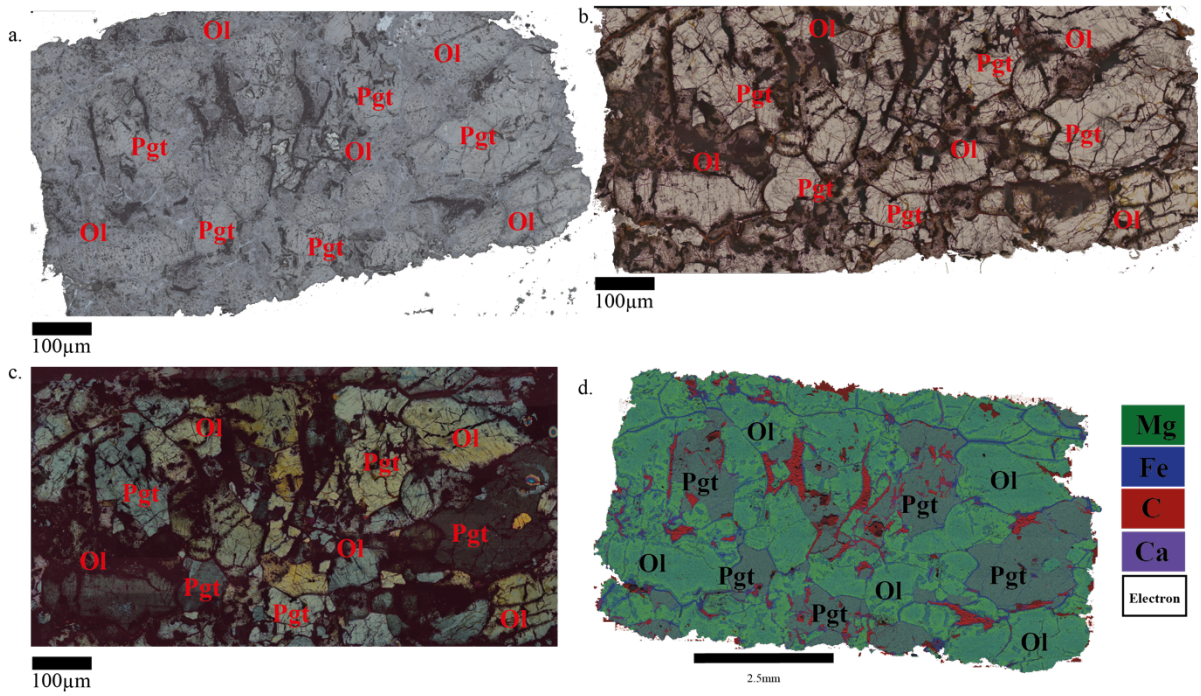

Figure 24: Images of Kenna. a. Reflected light; b. PPL; c. XPL and; d. EDS false colour map where magnesium is green, iron blue, carbon red and calcium purple. Annotations of the main minerals have been added to the images using approved mineral abbreviations from (Whitney and Evans, 2010), ol is olivine and pgt is pigeonite which is the assumed pyroxene mineral for the ureilites based on review from (Goodrich, 1992).

4.3.2 EDS and SEM image data

EDS maps of Kenna show veins throughout the sample that are composed of primarily carbon or iron but tend to contain a mixture. These veins usually define the grain boundaries of the olivine, and usually involve concentrating iron and carbon blebs surrounding the edge of grains, as shown in fig. 24d.

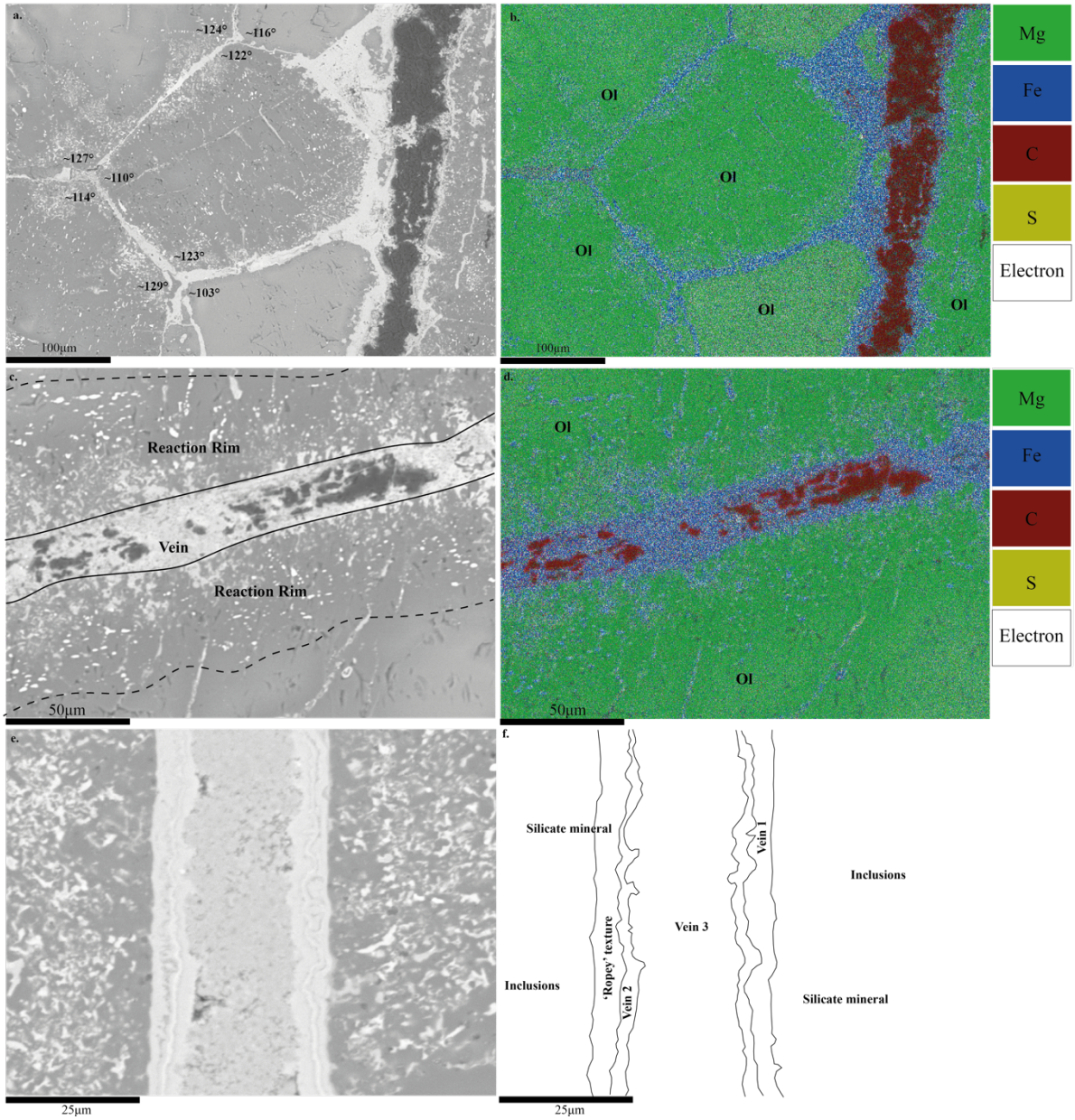

Figure 25: SEM and EDS image of an olivine grain within Kenna - a. BSE image with angles of the grain boundaries annotated. Grain boundary angles were measured using imageJ software, b. False colour EDS image of the distribution of elements Mg (green) Fe (Blue) and C (red) revealing that Fe and C are present as veins that decorate the grain boundaries of the olivine silicates. c. BSE image and d. False colour EDS image of a vein containing iron and carbon, e. shows the SEM image of a vein, f. Trace of the vein to highlight the main features.

The interior of the veins show discrete layering between the carbon and iron components, this is very well picked out through SEM images shown in fig. 25a, c & e. This layered appearance has been simplified in sketch form shown in fig. 25f where there is an interior light grey region in SEM (fig. 25e) which contains some dark and light patches signifying at least 3 distinct phases. Adjacent to this interior region on both sides (identified as vein 2 in fig. 25f) looks to be very cohesive it is a lighter grey massive section with no discernible phases or textures, the outermost portion of the vein shows a complex texture that could arguably be subdivided into two further layers, the lightest one and a similar light grey to the middle section exterior that has been disturbed and contains a ropey texture (fig. 25e) This

layer has been included as one (vein 1) due to what appears to be an interaction between the 2 sublayers causing the ropey texture (fig. 25 e &f).

4.3.3 EBSD data

EBSD was collected from Kenna allowing for analysis of phase, IPF and GROD-angle maps as well as crystal and sample CPO's.

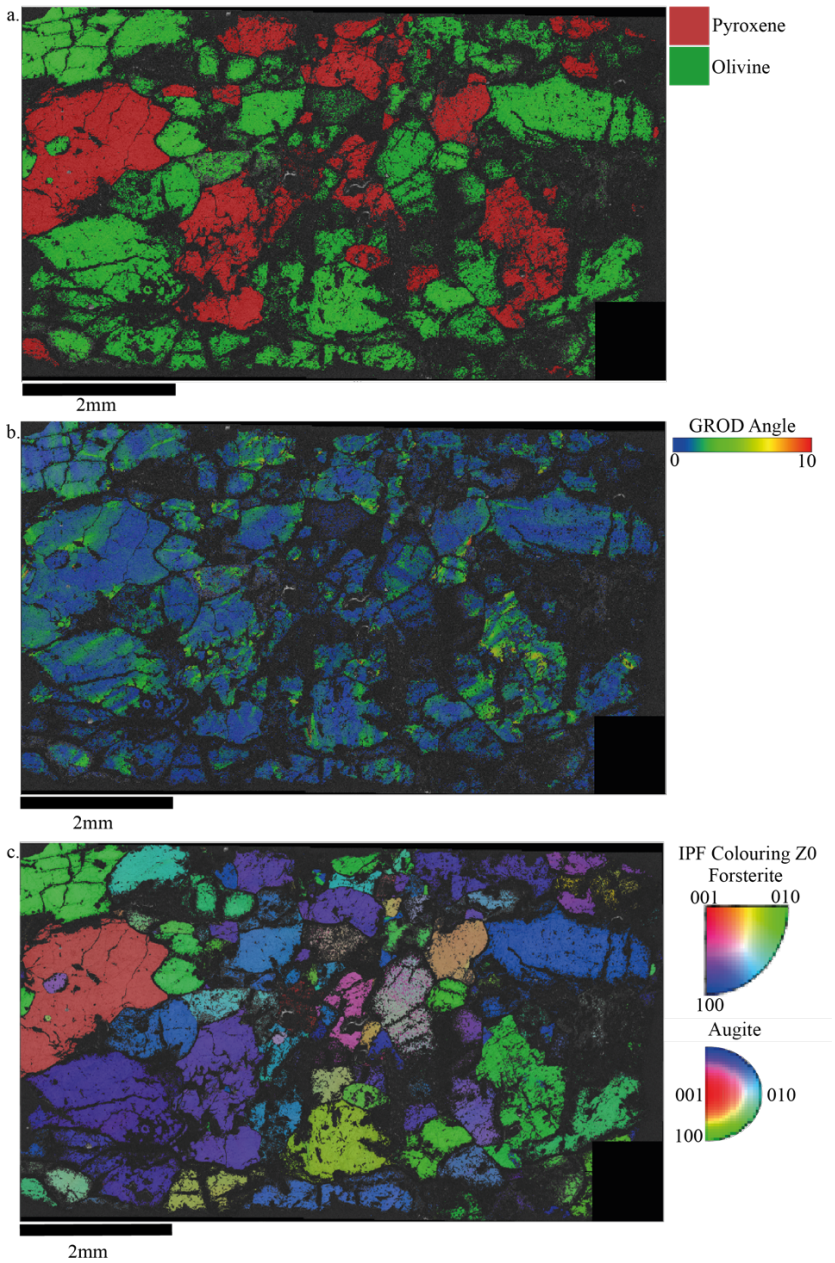

Figure 26: Kenna. a. Phase map showing abundance of olivine vs pyroxene. Olivine is green and pyroxene is red. Poikilitic textures shown through pyroxenes fully enclosing small olivine grains. b. EBSD Inverse Pole Figure map showing the 3D orientations of each grain relative to the Z axis. c. EBSD GROD-angle map showing the deviation from average grain orientation across individual grains. Blue represents 0° deviation from the average whereas red represents 10° of deviation.

The pyroxene grains can be seen in mainly red/green/purple, in the IPF map shown in fig. 26c, which indicates they have no preferred orientation as they are each oriented in different directions. The olivine crystals show more of a crystallographic alignment, as many crystals have similar colours in IPF maps (purple with some also in green/yellow). This shows the olivine is oriented toward the {100} or {010} relative to the Z axis of the sample.

The EBSD phase map, seen in fig. 26a, of Kenna highlights the higher abundance of pyroxene (25.3% (table 5)) compared to other samples. The GROD-angle map shows deformation is concentrated at grain boundaries or veins and very rarely permeates through a whole olivine or pyroxene crystal. This deformation in the GROD angle map, seen in fig. 26b, shows both olivine and pyroxene are deformed equally with no preference for either phase.

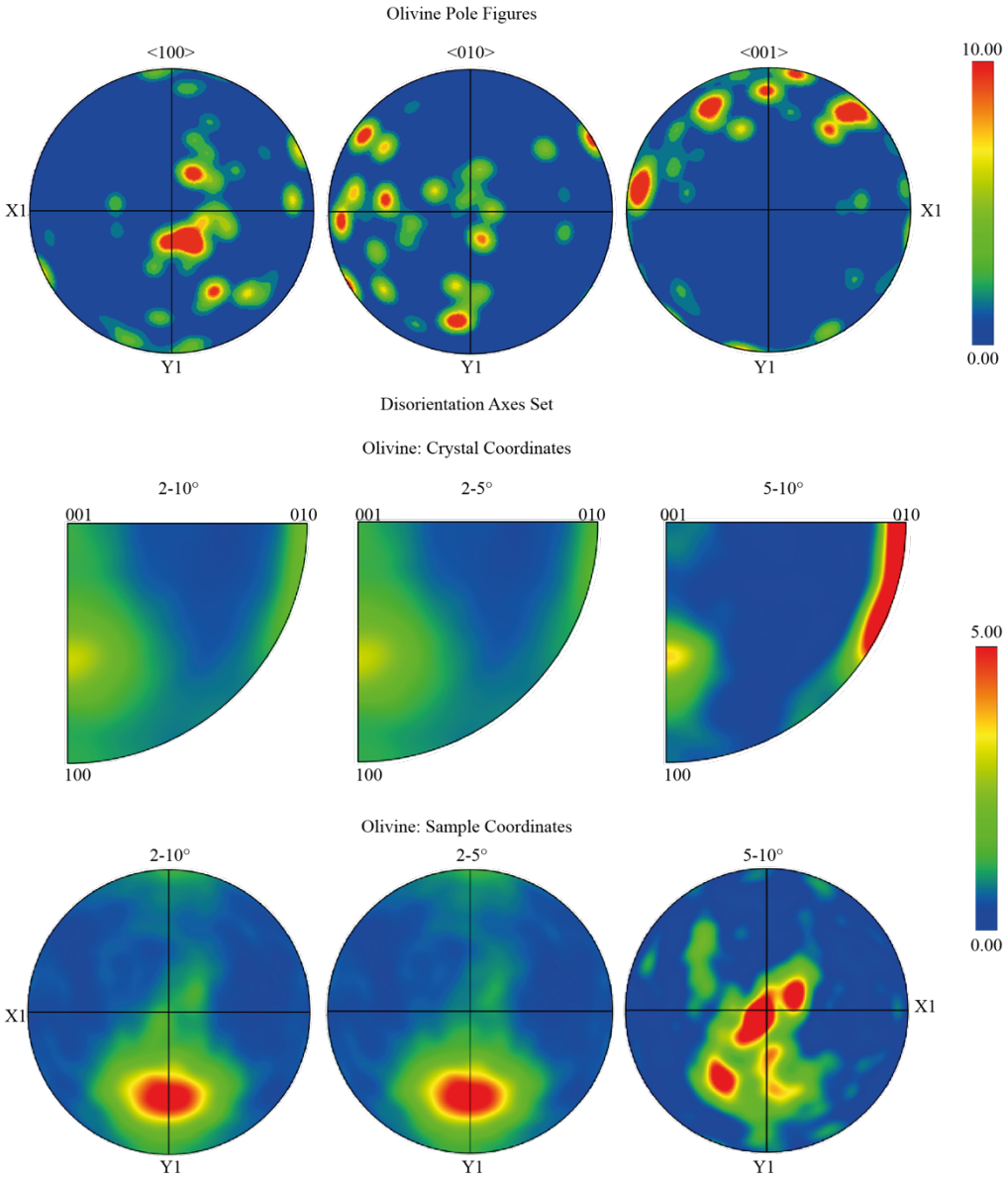

Figure 27: Kenna. Pole figures of the orientation of olivine crystal's 100, 010 and 001 directions relative to the plane of the section, along with disorientation axes plot for the olivine crystals for both sample and crystal coordinates. This shows the dominant slip system activated in 2-10° and then divided further into 2-5° and 5-10°.

Pole figures of olivine crystals in Kenna are shown in fig. 27, showing a concentration of crystal orientations expressed as a point maxima in the <100> axis, the configuration seems spread out across the other miller indices. The <001> shows a girdle or diffuse point maxima, and the <010> could also be argued as a diffuse point maxima however this is much more diffused and spread out than the other miller indices.

The disorientation axes plot showing the sample co-ordinates in fig. 27 shows a significant point in the lower middle section but with a hint of a girdle moving upwards. This point is particularly diffused in the 5-10° plot with a much more spread-out point maxima region.

4.4 MIL090980

MIL090980 was chosen for more in-depth study of the carbon-rich regions due to one particularly large area (~1 mm) that was high in carbon, compared to the other samples, and contained many brittle fractures that were highlighted by displacement along iron and carbon-rich veins.

4.4.1 Optical images

This sample was very olivine dominated. The olivine crystals are subhedral in shape and tend to be more elongate than is usual for olivine. The crystals are large, up to 4mm long axis, and are surrounded by a carbon matrix, seen in fig. 28 & 29. The carbon in this sample has concentrated into rounded aggregates up to 0.5mm width surrounding smaller silicate minerals, seen in fig. 29.

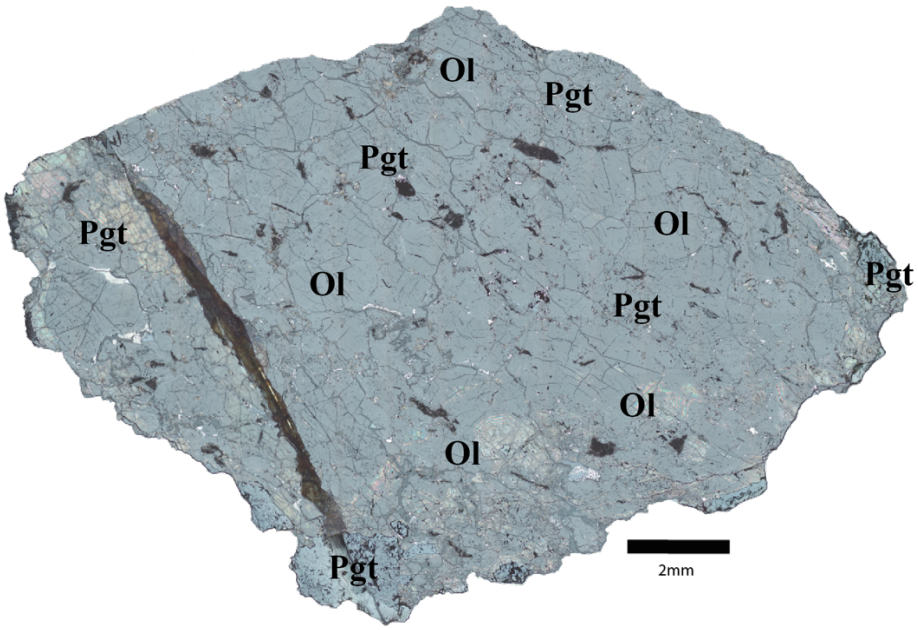

Figure 28: MIL090980. Reflected light image showing the overall texture of the sample including veins and fractures. Note the large fracture to the left of this sample which was generated during sample preparation. Annotations of the main minerals have been added to the images using approved mineral abbreviations from (Whitney and Evans, 2010), ol is olivine and pgt is pigeonite which is the assumed pyroxene mineral for the ureilites based on review from (Goodrich, 1992).

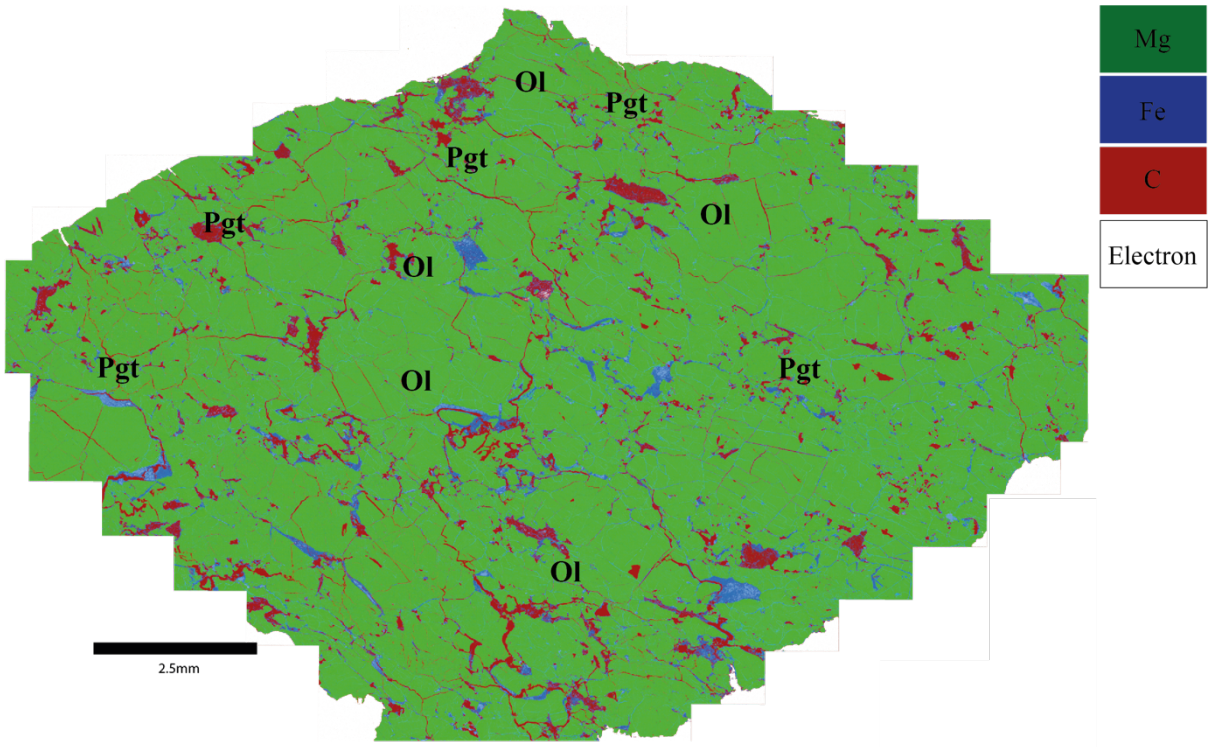

Figure 29: MIL090980. False colour EDS map showing the distribution of three major elements within the sample. Magnesium is in green, iron is in blue and carbon is in red. Calcium was not added to this map due to technical issues with exporting a new map. Annotations of the main minerals have been added to the images using approved mineral abbreviations from (Whitney and Evans, 2010), ol is olivine and pgt is pigeonite which is the assumed pyroxene mineral for the ureilites based on review from (Goodrich, 1992).

4.4.2 SEM-EDS Data

EDS maps of MIL090980 showed a large amount of carbon and iron rich veins running through the sample, and within grains. In the large EDS map shown in fig. 29 there appears to be more carbon veins than iron, and the iron instead prefers to concentrate around veins and grains. The veins appear to have a preferred orientation. Iron and carbon also appear to concentrate into aggregates alongside silicate grains, giving the sample a hummocky texture.

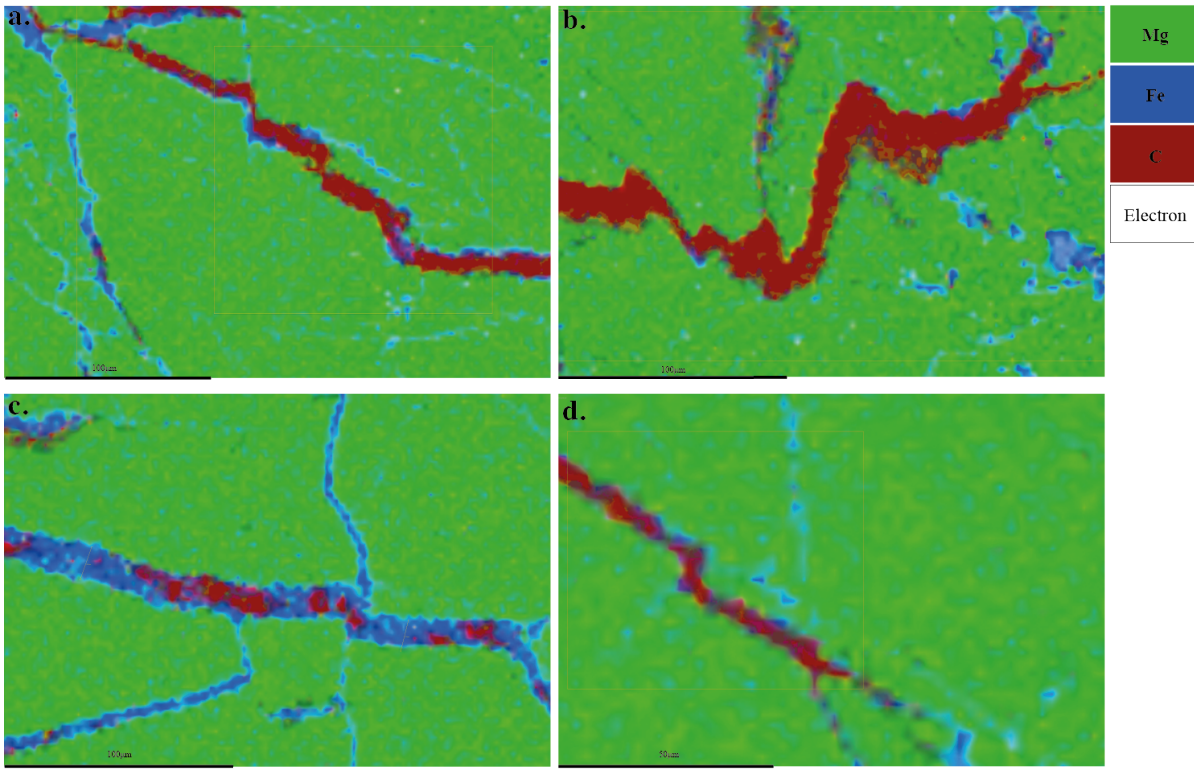

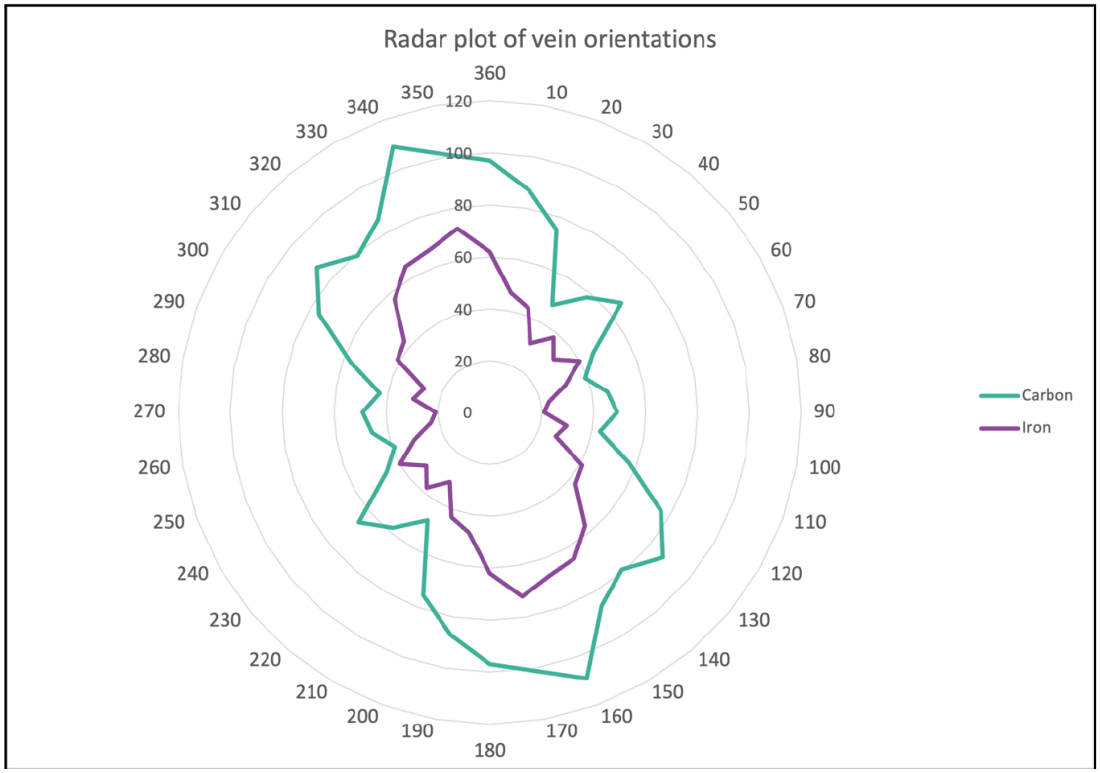

Figure 30: MIL 090980. False colour EDS images showing the veins being dissected by faults. Below are the orientations of the veins. Carbon veins were measured for anything ImageJ recognised as larger than 100 pixels, Iron veins were measured for veins larger than 250 pixels. This is to minimise biased data from fragmented veins being measured multiple times

The veins were measured in ImageJ software to get an orientation figure shown in fig. 30. The iron veins may be more fragmented than the carbon veins as the software initially pulled out ~5000 data points for the Iron veins compared to ~1200 for carbon suggesting that individual iron veins have been broken into many smaller sections thus one iron vein is sampled multiple times. As the EDS image, fig. 29, shows more carbon veins than iron the ImageJ process was run again but discounting any measurements below 250 pixels in order to avoid measuring the same vein multiple times.

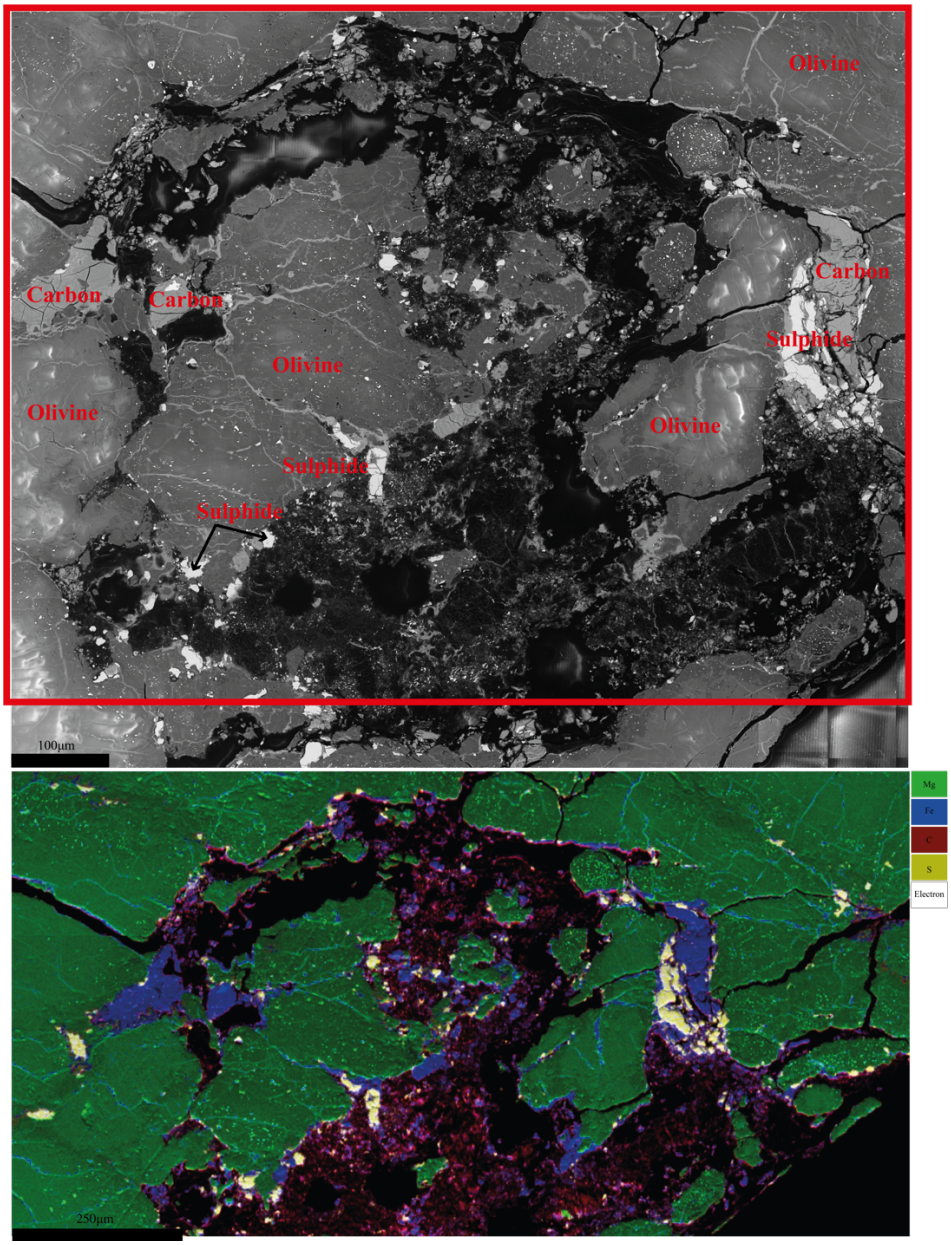

Figure 31: MIL090980. The carbon-rich region that was selected for Raman study. This is a backscatter electron image where the dark/black patches are carbon, the light grey are olivine and the very light patches are sulphides. The red box indicates the field of view for the false colour EDS image of the same carbon rich region. Magnesium is shown in green, iron in blue, carbon in red and sulphur is shown in yellow. This figure shows the association of different elements inside this largely carbon rich region.

EDS data of the specific carbonaceous region shown in fig. 31 shows high concentration of sulphur decorating the margins of this area and is present in smaller quantities within the carbon-rich zone. The sulphur is also closely associated with areas that are rich in iron.

4.4.3 EBSD Data

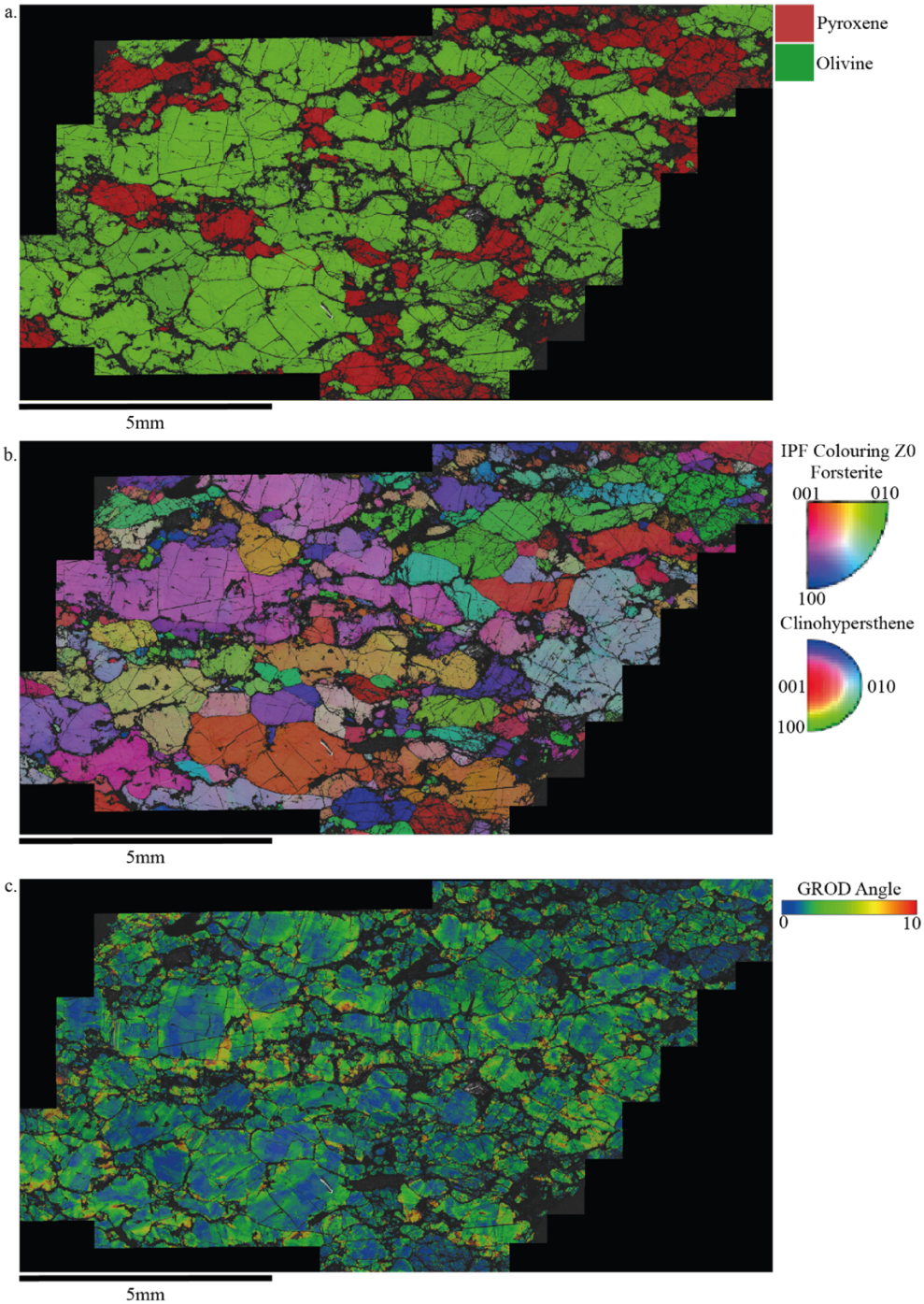

Figure 32: MIL090980. a. EBSD phase map showing the olivine crystals in green and the pyroxene in red. b. EBSD IPF map showing olivine (forsterite) and pyroxene (clinohypersthene). c. EBSD GROD angle map, blue represents 0° deviation from the average whereas red represents 10° of deviation.

The IPF map shown in fig. 32b shows some tendency toward preferred orientation of crystals but there is still significant variety. Pyroxene crystals are often green, indicating they are aligned with the <100> axis pointing up away from the image but there are also a couple of red and purple pyroxene grains indicating the <001> axis is point away from the image in the Z direction (fig. 32b). Olivine grains make up the majority of this sample (46.0% table 5), shown in the phase map (fig. 32a) and a majority of them are seen in the IPF map in pink or red which indicates some preferential orientation with the <001> axis pointing up in the Z direction but again there is some variation with some crystals in purple or blue indicating the <100> axis is facing the Z direction (fig. 32b).

The GROD angle map for MIL090980 seen in fig. 32c shows there is significant uniform deformation across the whole sample. Some larger grains show that the deformation is contained at grain boundaries, and the highest deviation (red colours) is contained close to fractures or veins (fig. 32c).

The pole figure data for MIL090980 shown in fig. 33 shows a girdle in <001> with either a diffuse point maxima or several point maxima in <100> and <010>.

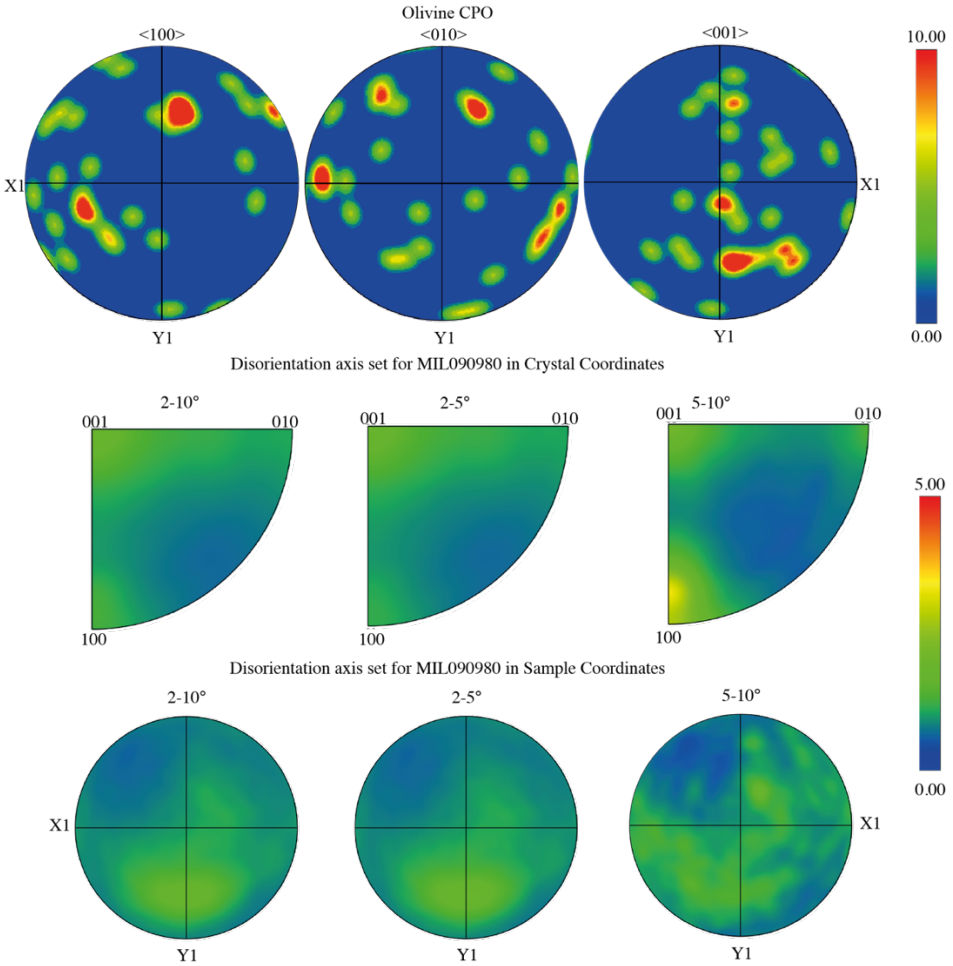

Figure 33: MIL090980 olivine disorientation axis set in crystal and sample co-ordinates for disorientations 2-10°, 2-5° and 5-10°. Range is shown to identify whether certain angles prefer certain slip systems.

The disorientation axes for crystal co-ordinates plot shown in fig. 33 shows one main concentration in the <100> direction, particularly for the range of 5-10°. Disorientation axis plots for sample co-ordinates shows a point maxima for all angle ranges, with some spreading but not enough to consider this a girdle.

4.4.4 Raman Data

Raman analyses were conducted on carbon rich regions within MIL 090980 to establish whether diamonds were present in this sample. The results of which show both diamond and graphite are present within the carbon rich areas.

The sharp peak at 1331-1332 cm^{-1} seen in fig. 34d is characteristic of the first order band for diamonds, as described in (Knight & White, 1989). The 1355cm^{-1} peak and the 1582-1583cm^{-1} peaks are, in combination, considered diagnostic of graphite and represent what is known as the D and G bands of graphite respectively (Knight & White, 1989).

Raman maps shown in fig. 35a-c show diamonds or diamond clusters up to 5 μm in size throughout the carbon-rich region that was studied. These clusters are surrounded by graphite.

Values for the intensity of the graphite D band (I_d) over the intensity of the graphite G band (I_g) are shown overlain each map in fig. 35a-c showing a spread from 0.295501 to 0.448167. This figure is representative of the crystallinity of the graphite, with lower figures indicating more crystalline graphite (Ferrari, 2007).

The Full Width Half Maximum (FWHM) plot (fig. 35d) show considerable spread around the 1331cm^{-1} peak and a spread of values for the width, although it should be noted that some of the diamond peaks are not completely separated from the graphite D band as seen in fig. 34b & c so the FWHM value may be incorporating the graphite peak as well as the diamond one.

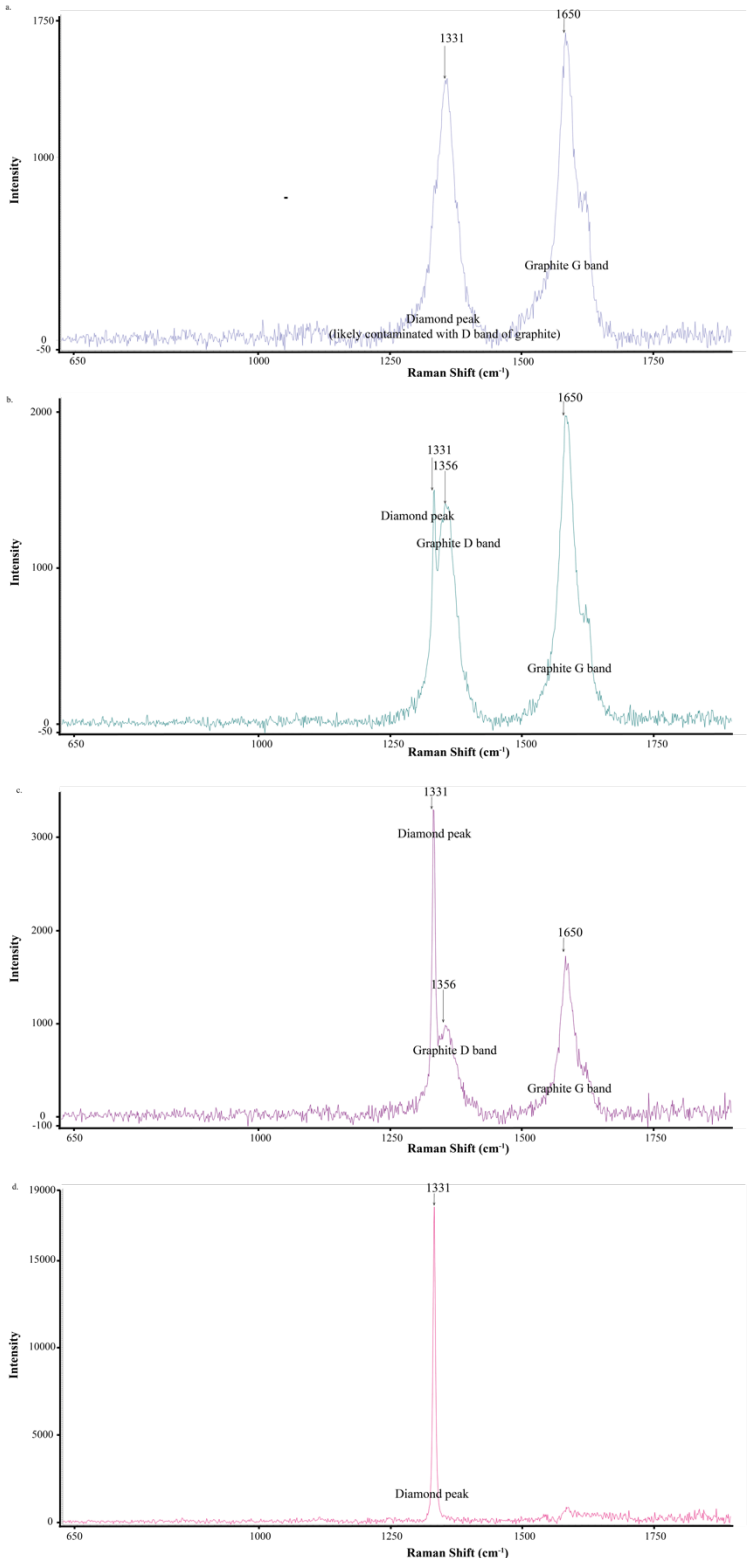

Figure 34: Images show representative Raman spectra from MIL090980 for diamond and graphite. a. shows the spectra of graphite with the characteristic D and G peaks, the D peak is centred at 1356 cm^{-1} and the G peak is centred at 1582 cm^{-1}. b. shows the spectra for graphite and diamond combined. Note the same D and G peaks for graphite as seen in a but with a strong slim peak at 1331 cm^{-1} that appears on the side of the D peak. c. shows the same combination of diamond and graphite with a much stronger diamond peak at 1331 cm^{-1}. d. shows a diamond peak on its own appearing as a very strong sharp peak at 1331 cm^{-1}.

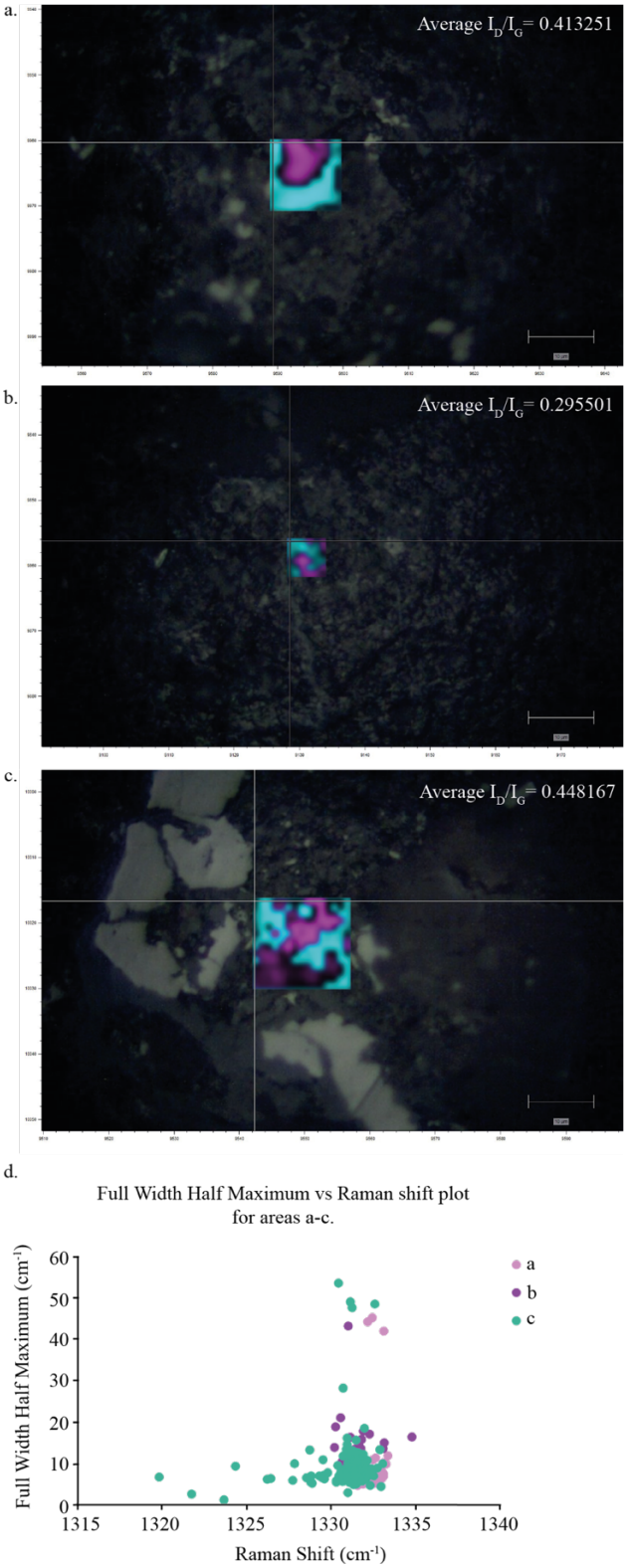

Figure 35: MIL090980. a-c show areas where Raman mapping took place. Purple corresponds to areas where diamonds were identified, blue is the areas containing graphite. Overlain on each is the average I_d/I_g value for each map. d. shows a FWHM vs Raman shift plot combining the diamonds from all 3 areas, the key a-c corresponds to the areas a-c in the figure.

4.5 MIL090076

4.5.1 Optical images

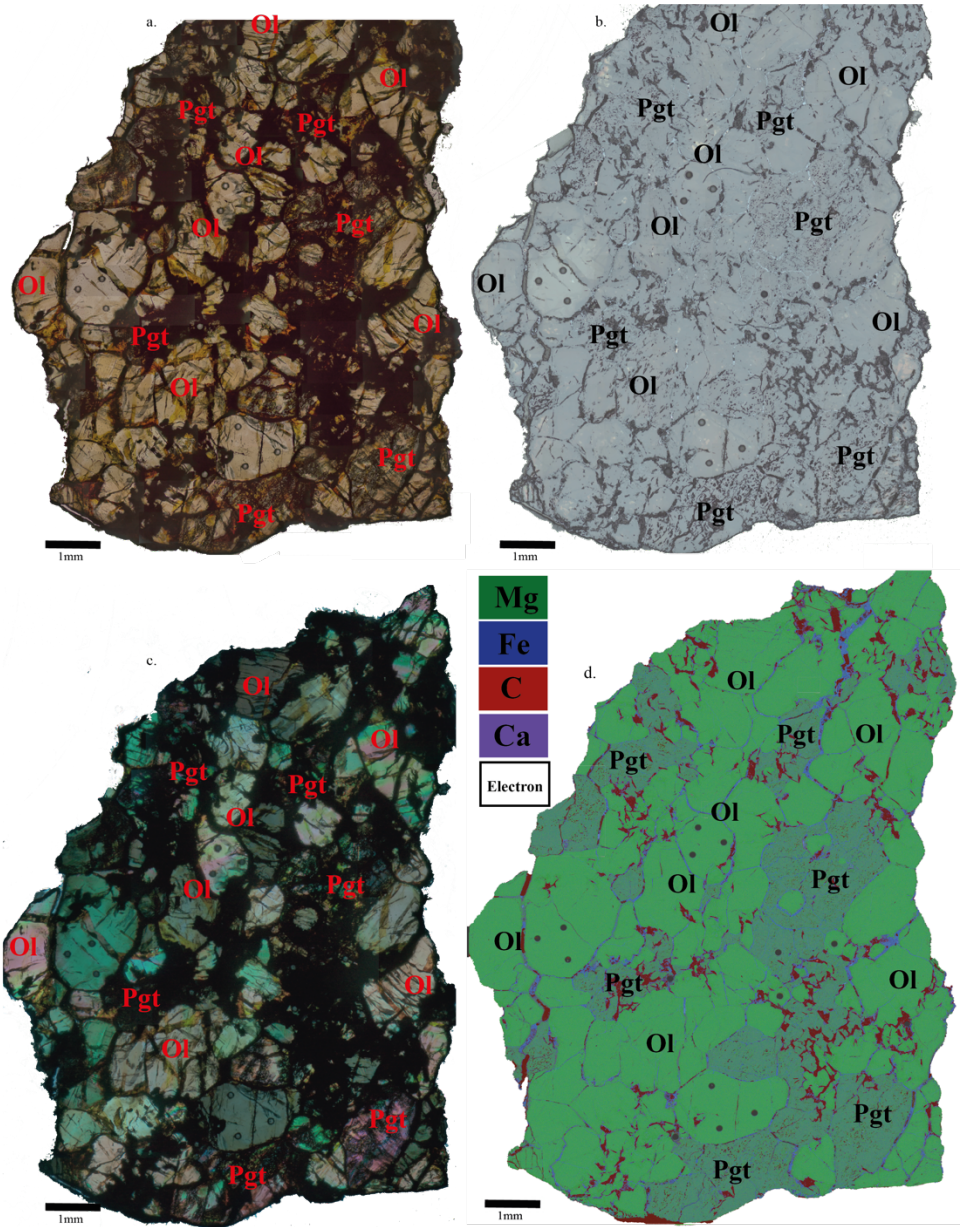

Figure 36: MIL090076. Optical and false colour EDS images; a. Plane polarised transmitted light; b. Reflected light; c. Cross polarised light; d. False colour RGB EDS map showing the distribution of C, Mg, Fe and Ca. Mg is in green, Fe is blue, C is red and Ca is in purple. Annotations of the main minerals have been added to the images using approved mineral abbreviations from (Whitney and Evans, 2010), ol is olivine and pgt is pigeonite which is the assumed pyroxene mineral for the ureilites based on review from (Goodrich, 1992).

4.5.2 SEM-EDS data

BSE images show a weak granoblastic texture, though not as clearly as in Hajmah. Grain boundaries tend to be more curved rather than defined triple junctions (fig. 36). Olivine grains within this sample appear to be more homogeneous in Mg content with less well-defined reaction rims, although they are still present, when compared to other samples (fig.

36d). Carbon and iron are often closely associated within thick veins or disseminated within silicate grains. An iron vein was identified within this sample to have a morphology reminiscent of folding morphologies, seen in fig. 37c.

The sample wide EDS map shows the granoblastic texture of curved boundaries meeting at triple junctions and defined by the carbon and iron rich veins (fig. 36d).

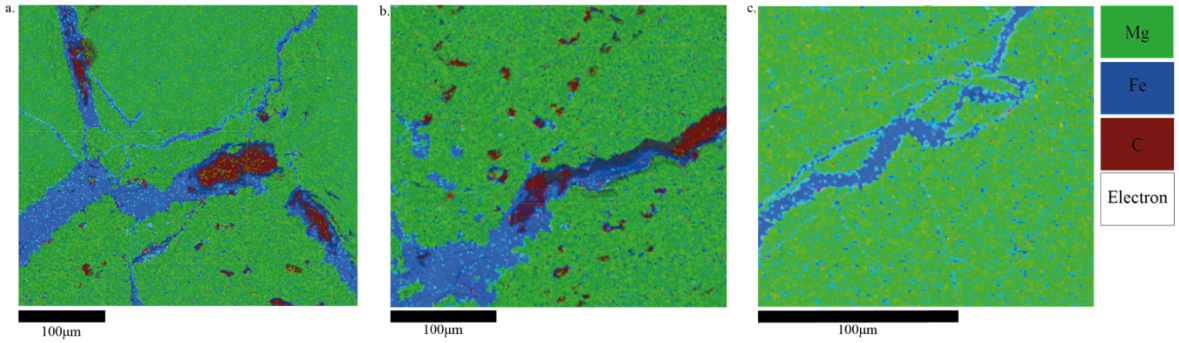

Figure 37: MIL090076. False colour EDS maps, magnesium is green, iron is blue and carbon is red. A vein containing both iron and carbon that has been offset by faulting; b) iron and carbon vein with a boudinage morphology; c. shows an iron vein with a folded morphology.

4.6 Novo Urei

Novo Urei was observed by optical microscopy and was also analysed for EPMA data presented later in this section. This was due to time constraints, and as it displayed similar features to Hajmah, Kenna and MIL090076 ureilite samples.

4.6.1 Optical images

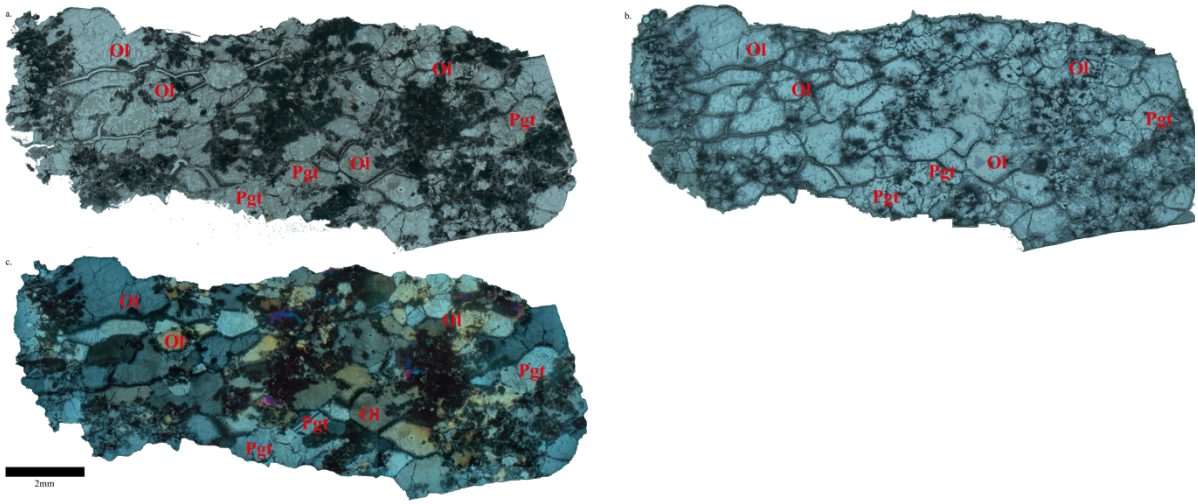

Figure 38: Novo Urei. Optical images; a. Plane polarised transmitted light; b. Reflected light; c. Cross polarised transmitted light. Annotations of the main minerals have been added to the images using approved mineral abbreviations from (Whitney and Evans, 2010), ol is olivine and pgt is pigeonite which is the assumed pyroxene mineral for the ureilites based on review from (Goodrich, 1992).

Novo Urei exhibits a granoblastic texture with 120° triple junction boundaries decorated with a dark interstitial matrix, seen in fig. 38. Pyroxenes in Novo Urei exhibit twinning and cleavage shown in fig. 39.

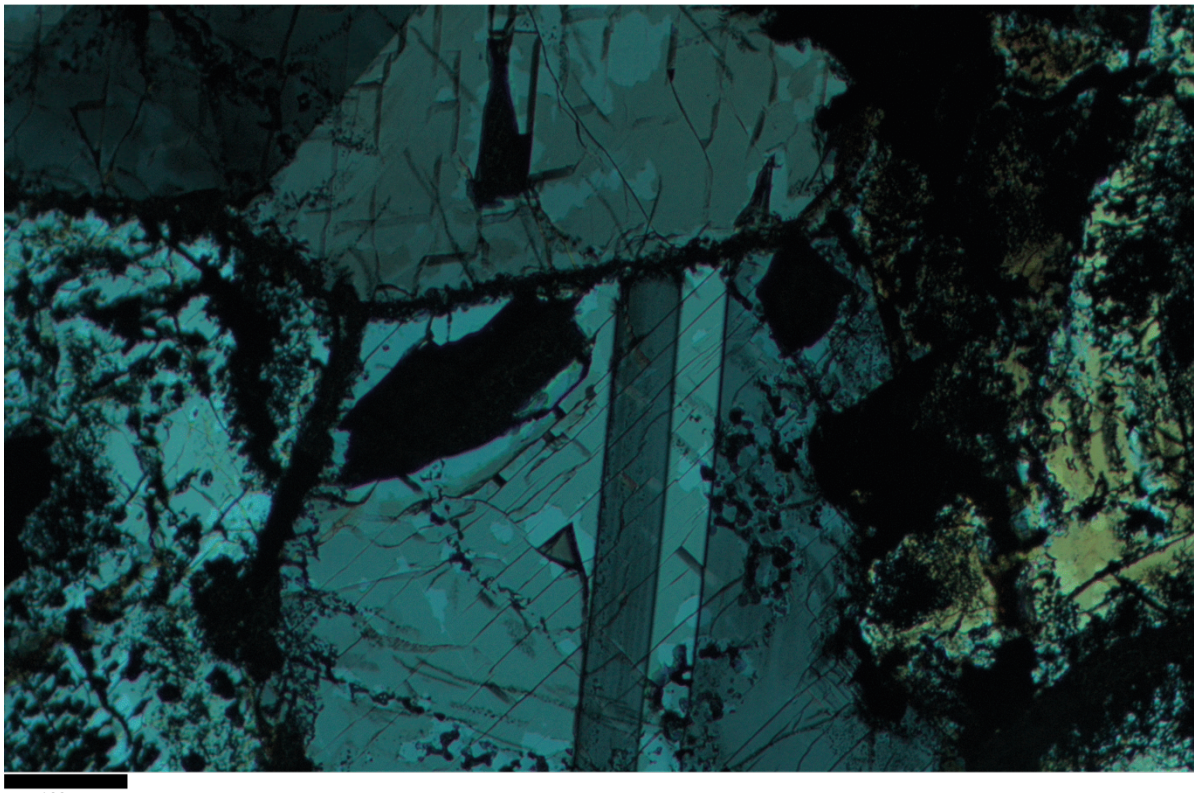

Figure 39: Transmitted cross polarised light image of the area of Novo Urei that displays a twinned pyroxene. Note the cleavage pattern within the pyroxene which is cut by the twin at approximately ~45°.

4.7 EPMA microprobe data (all samples)

Microprobe data of major elements was analysed for samples: Novo Urei, Goalpara, Kenna, MIL090980 and MIL090076. This section has been combined to discuss all samples at once as opposed to the previous structure, this is to avoid repetition and to more easily demonstrate the trends across the suite of samples.

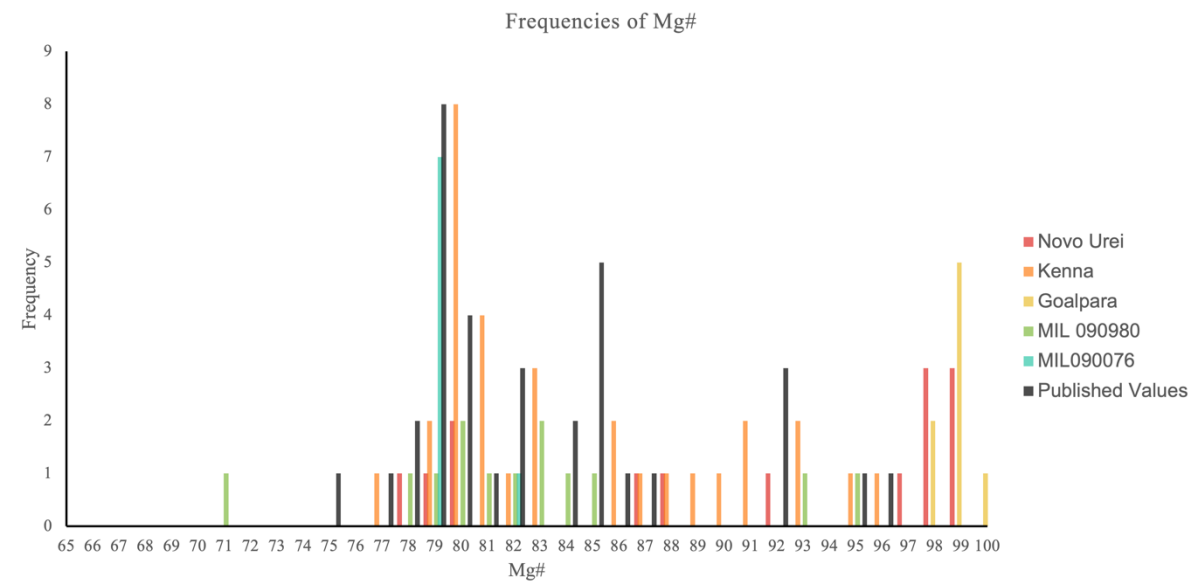

Figure 40: Frequency plot of Mg# ((Mg/Mg+Fe)*100) recorded for each sample using EPMA data. Published values compiled in (Goodrich, 1992) have been plotted to show a comparison with these results and other ureilite results.

The Mg# plot shown in fig. 40 shows Goalpara is the most Mg rich of all the samples whilst MIL090076 is generally the most Fe rich. MIL090980 and Novo Urei have a spread of values from Mg-rich to Fe-rich, with MIL090980 plotting at the most Fe-rich point of the diagram.

Table 6: Summary table showing the average Fo numbers of each sample from the EPMA data. This was calculated using Fo= Mg/(Mg+Fe)*100 in atomic %.

Sample	Fo Number
Novo Urei	90.24
Goalpara	98.44
Kenna	83.87
MIL090980	82.09
MIL090076	78.87

The Fo numbers for each sample are listed in table 6 which matches the same pattern as fig. 40 with Goalpara having the highest Fo number (Fo98) and MIL090076 (Fo78).

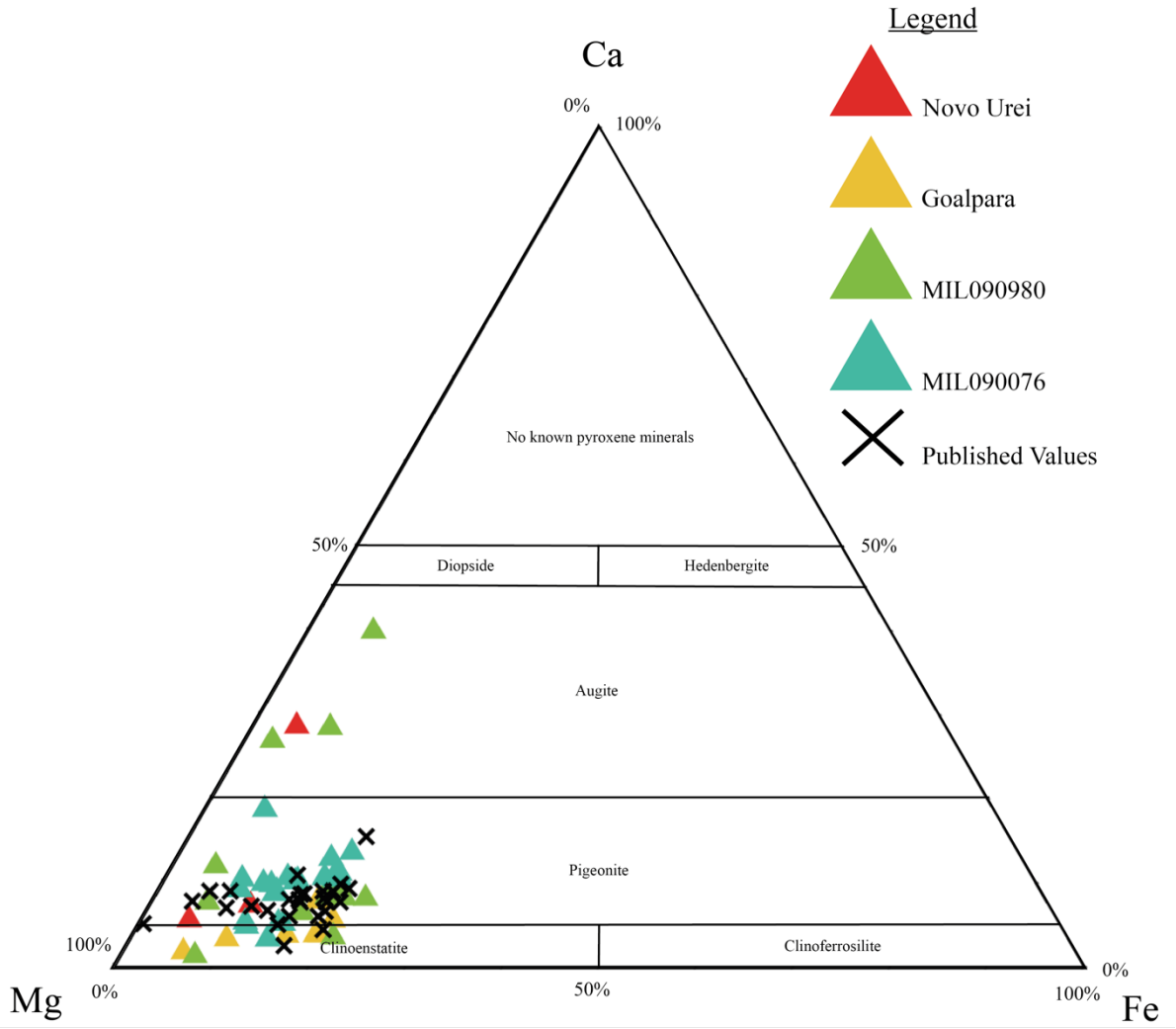

Figure 41: Ternary plot of Ca-Mg-Fe ratio for pyroxenes in four ureilite samples: Novo Urei; Goalpara; MIL090980; and MIL090076. Kenna was not included as no pyroxenes were measured. The data points were plotted using ternaryplotter.com and then overlain above a diagram of accepted nomenclature of pyroxene types adapted from (Morimoto, 1988). This shows the composition of the pyroxene crystals which then determines the subgroup that they are part of. Published values compiled in (Goodrich, 1992) have been plotted to compare results of this study with previous ureilite studies.

The pyroxene compositions shown in the ternary diagram in fig. 41 shows all of the pyroxene is clinopyroxene with the exact composition varying from low (0.695 wt% CaO in MIL090980) to high calcium content (18.359 wt% CaO in MIL 090980). Low Ca pyroxene includes pigeonite and clinoenstatite whereas augite is considered high-Ca pyroxene. Augite is only present in samples MIL090980 and Novo Urei, while Goalpara is predominantly Ca poor clinoenstatite. Fig. 40 shows low values of alkali content ($Na_2O + K_2O$) with no sample plotting above 0.8 wt%.

Summary Tables

Table 7: Summary table of main features observed in EDS maps for each sample studied this way. Average olivine and pyroxene Mg# was calculated using EPMA data.

Sample	Modal Mineralogy	Crystal size	Average Olivine Mg#	Average Pyroxene Mg#
Hajmah	Ol: 62.7% Px: 22.9% C: 7.2% Fe: 7.2%	Up to 4 mm	No EPMA data	No EPMA data
Goalpara	Ol: 72.2% Px: 2.5% C: 12.7% Fe: 12.7%	Up to 1 mm	Fo98	85
Kenna	Ol: 59.6% Px: 25.3% C: 9.1% Fe: 6.1%	Up to 2.5 mm	Fo83	72
MIL090980	Ol: 46.0% Px: 31.6% C: 14.3% Fe: 8.2%	Up to 4 mm	Fo82	86
MIL090076	Ol: 57.1% Px: 17.9% C: 15.5% Fe: 9.5%	Up to 1.5 mm	Fo78	83

Table 8: Summary table of main features observed in EBSD maps for each sample studied this way.

Sample	Lineation/foliation	Average internal misorientation	Maximum internal misorientation	Dominant slip system and dominant rotation axis
Goalpara	Foliation	1.89°	14.16°	(010)[100]
Kenna	See discussion	1.1°	15.88°	(001)[100] or (100)[001]
MIL090980	Weak foliation	1.0°	11.95°	(010)[001]

5.0 Discussion:

The discussion section is split into themes based on key observations instead of individual samples. The topics covered include reaction rims; annealing textures; vein fill; brittle failure; shock; mosaicism; diamonds; shear; phase heritage; and the crystallographic preferred orientations (CPO's) from the EBSD data sets. This is to ensure the discussion section is easy to follow and the same observations and interpretations that may be seen in multiple samples are not repeated.

Topics discussed here were chosen as they help with the main aim of this thesis which is to construct a geological history of the ureilite group. Reaction rims, annealing, vein fill and the diamonds were studied with an aim of constraining the timings of phase formation. Brittle failure, shock, mosaicism, shear, phase heritage and CPO's were studied with the aim of constraining the mechanism through which key stages of ureilite formation occurred.

5.1 Reaction rims

The SEM images of the veins throughout the whole suite of samples but particularly in Hajmah (fig. 14 & 15a-d) and Kenna (fig. 24 & 25a) show reaction rims surrounding the olivine which disperses tiny metallic grains throughout the rim (Rubin, 2006). Some of these grains can be seen as the bright spherule features in the SEM images that are present in the rims but absent in the cores of the crystals (fig, 14 & 24). The EDS images showing the magnesium content, fig. 15i-l of the crystals and veins in Hajmah shows the magnesium content is also lower surrounding the blebs (darker shade of green), which is also due to the reaction between the olivine and the metallic blebs causing the olivine to be reduced. The rims of the crystal seen in fig. 25a & b in Kenna show the reaction between the olivine and the vein material as the iron in particular is 'eating' away at the crystal and intruding into the olivine giving it a ragged texture around the edge. Due to the fact these are only reaction rims and not fully reduced olivine crystals indicates the reaction was not allowed to continue to completion and must have been disturbed or halted at some point in the formation history. The presence of reaction rims also suggests that the olivine crystals first formed in equilibrium and then something happened or was introduced which disturbed the equilibrium triggering a reaction. In this case, the reaction was triggered by the emplacement of the veins causing the olivine and the vein material to react.

Pyroxene grains in previous studies have been reported to show evidence of impact smelting through the inclusions of iron and a 'ragged' texture (Warren and Rubin, 2010). Highly shocked samples, including Goalpara, have been reported previously to contain this texture (Warren and Rubin, 2010). However, for the samples in this study this is not a well-developed or extensive texture, the pyroxene crystals are not porous and do not contain glass they only contain metallic inclusions. In fig. 18 there is evidence of some inclusions within the pyroxenes and colour changes in XPL surrounding fractures however not to the extent that was reported by Warren and Rubin (2010).

5.2 Vein fill

Veining within rocks can be studied to determine stress fields, deformation events and constrain timings of deformation events. The exact stress field can be measured terrestrially when the spatial context is known however this is not possible for meteorites. Veins have therefore been looked at in this study to ascertain how many deformation events involving vein formation were experienced by the UPB and discuss potential contexts of vein formation.

The suite of ureilites used for this study show veining occurring along grain boundaries and infilling fractures, figs. 14, 20, 24, 30 and 37. Veining at grain boundaries has been observed in terrestrial ultramafic mantle xenoliths, but the composition of these veins is largely basaltic and glassy (Wirth, 1996). The mechanism proposed for terrestrial grain boundary veins is that of grain boundary melting due to distortions of the crystal lattice at the grain boundaries (Wirth, 1996). Distortions and defects in the crystal lattice can lower the melting temperature of the crystal (Wirth, 1996). This is possible for the ureilites but unlikely due to the composition of the veins, if olivine or pyroxene was to melt the composition of the veins would not be pure carbon or iron which is what the majority of the observed veins are composed of. Instead, it has been suggested that the veins formed due to reactions between olivine and previously adjacent, or injected carbonaceous phases (Barrat et al., 2017). These

reactions would have been facilitated by application of extra heat and pressure potentially during the break-up of the UPB (Barrat et al., 2017).

Veins form after a crack has been produced in a rock and then a fluid enters this crack or fracture and begins to crystallise or precipitate minerals (Oliver and Bons, 2001). Veins can crystallise in either an antitaxial or syntaxial way. Antitaxial refers to veins that have grown from a central point outward towards the wall rock, these veins are often fairly symmetrical (Oliver and Bons, 2001). Syntaxial veins are the opposite, they start at the wallrock and grow inwards, and thus are usually less symmetrical (Oliver and Bons, 2001). The morphology of the veins can vary depending on the environmental conditions present during vein formation.

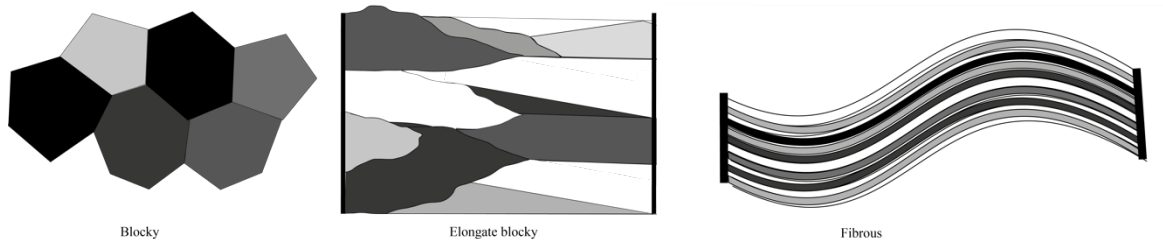

Figure 42: Schematic diagram of main vein crystal morphologies. Adapted from (Fossen, 2016)

Fibrous veins have a high aspect ratio for the individual crystals as they tend to be very elongate, they form in situations where growth is inhibited by either a narrow aperture or low temperatures (Oliver and Bons, 2001). These veins tend to form antitaxially and appear very symmetrical but are typically only found in low grade metamorphic rocks (Oliver and Bons, 2001). Fig. 20a &b shows a carbon rich vein within Goalpara that has a texture that resembles fibrous antitaxial veins seen in fault structures on Earth (Bons et al., 2012), but this texture does not continue throughout the whole vein. This may be due to the crystal having a platy habit, as it is high in carbon this could be a platy graphite that appears fibrous when looking from the angle the sample was cut. Goalpara is also the only sample in this study seen to have experienced extensive fracturing which resulted in veining. In all other samples the veins are restricted to grain boundaries only, with none seen to traverse across the sample or minerals in an aligned fracture set. The veins seen in fig. 20 are present in areas of Goalpara that have been affected by a fracturing event, seen in the parallel fractures affecting the sample (fig. 21a-d).

Crack-seal veins show evidence of growth competition between crystals. They tend to form syntaxially connected to the host rock and get wider in the growth direction as the individual crystals are outgrown by larger neighbours (Oliver and Bons, 2001). They may be asymmetrical and only grow from one side of the host rock until reaching the other wall or running out of fluid to crystallise out from. Crack-seal veins may have inclusion bands parallel to the wall rock which indicate multiple crack and subsequent seal events (Oliver and Bons, 2001).

Stretched crystal veins contain crystals that stretch the whole way from one side of the wall rock to the other, resulting in a stretched appearance (Oliver and Bons, 2001). They are the result of multiple crack-seal events, where the crack plane is not the same one throughout the whole vein formation, so the crack surface can cut through previously precipitated material. The act of cracking a forming vein allows for new material to precipitate causing the vein crystals to appear fibrous or stretched (Oliver and Bons, 2001).

SEM images of the veins within Kenna, fig. 25, show the iron and carbon sections layering and interacting in a way consistent with crack and seal vein formation, particularly in the sense that the ropey texture noted in fig. 25f could be an inclusion band described by (Oliver and Bons, 2001). On Earth this mechanism is usually associated with high-grade metamorphic rocks where the minerals are undergoing chemical transfer and pressure solution (Ramsay, 1980). Multiple cracking events can cause the vein to become a compound vein (Ramsay, 1980), which could explain the veins that have a layered appearance. Banding of the vein parallel to the vein wall, which is seen in the SEM image in fig. 25e, is considered evidence of high fluid pressure at the time of vein formation (Wiltschko & Morse, 2001). Each band is interpreted to represent a different phase of vein opening and infilling (Wiltschko & Morse, 2001). These veins could be shock generated, however shock veins would be expected to resemble pseudotachylite rocks (Kovaleva et al., 2019) and be glassy in texture (Xie et al., 2011) rather than displaying the banding that is seen (fig. 25e). Shock veins represent localised melt pockets generated under the high pressures (Langenhorst et al., 2002). Shear forces or heterogeneous pressure have been proposed for mechanisms that would create localised melting (Langenhorst et al., 2002). The GROD angle map in fig. 26b for Kenna show that there appears to be high levels of deformation across the sample, which could be shock related however no other clear shock evidence has been noted for this sample of Kenna, this will be discussed in more detail in a later section about shock. The disorientation axis plot (fig. 27) for Kenna shows evidence of a shear component due to the point maxima, again this will be discussed in a later section dedicated to shear, which suggests this may have been the mechanism for localised melting that could create the layered veins. However, many previous authors have suggested a carbon-rich impactor introduced the carbon component which may have also provided the fluids required to form these veins (Warren and Kallemeyn, 1992).

GROD angle maps are used as a tool to assess the levels of plastic deformation or bending a sample has undergone (Griffin et al., 2022a). MIL090980 appears to be deformed uniformly in GROD angle EBSD maps (fig. 32c) but displays a preferred orientation of the veins, seen through analysis of the EDS image in imagej software presented in the rose diagram in fig. 30 suggesting the veins were emplaced within the same stress field. Both the veins infilled by carbon and iron rich phases show a similar pattern, there is a strong trend running almost vertical across the sample with a concentration of vein orientations visible in the rose diagram at 340/160 (relative to the xy orientation the EDS map was collected) with a spread of 50 degrees. There is a second smaller, but more defined peak in the rose diagram (fig. 30) at 240/60 degrees indicating the presence of almost horizontal veins relative to the orientation of the EDS map as well. The presence of these veins could indicate one or more stress fields which were responsible for the formation of these textures in the sample. Compressional veins/fractures form at 20-40° to the σ1 stress tensor (Ramsey and Chester, 2004) so depending on the configuration of σ1 it is possible for one stress field to have caused both orientations of vein. However, veins can also form during extension in tension fractures which form perpendicular to σ3. Due to previous discussion around Kenna indicating these veins are likely to be infilling shear fractures this suggests they were under a compressive regime (Ramsey and Chester, 2004). This means both sets of veins could have formed under the same compressive regime, however disorientation axis plots for MIL090980 (fig. 33) show there is a shear component present in this sample but it is not as clear as Kenna which suggests the shear stress on MIL090980 may have been variable. MIL090076 vein morphologies (fig. 37) also heavily suggest shear stresses, include some boudinage and fold morphologies which both indicate alternate stresses.

Fig. 15d shows the veins of Hajmah, some of which exist as rectangular discordant veins (Birtel and Stöckhert, 2008). These have a low aspect ratio (length/width) which indicates they may not have formed as a result of the usual brittle/elastic regime (Birtel and Stöckhert, 2008). Discordant veins on Earth form as they were once part of a pervasive vein fill system that passed through the whole rock creating a widespread region of veining, but due to a ductile component in the fracturing the host rock fails and fills in the cracks, cutting off vein formation and leaving a discordant vein that is not connected to the main vein system (Birtel and Stöckhert, 2008).

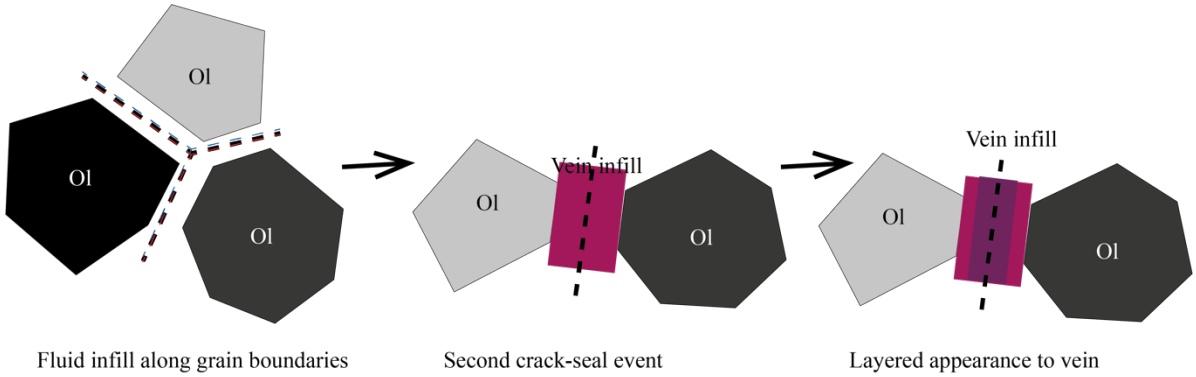

Figure 43: Cartoon schematic of how veins formed in the ureilite group.

5.3 Evidence for brittle failure

Brittle failure is the most common deformation regime in olivine dominated rocks below 600°C (Prieto et al., 2017). Brittle failure encompasses all kinds of fracturing and cracking of rocks, from the microscale all the way up to large fault lines seen on the Earth's surface (Brantut et al., 2014). In dry conditions with rapid loading of stress, the deformation is controlled by the amount of stress applied whereas in wet conditions with slower loading of stress the extent of deformation is largely controlled by the amount of time involved (Brantut et al., 2014).

As discussed in the previous section on veining, there is a crack-seal formation texture in some veins seen which indicates brittle failure prior to vein formation. However, the veins in MIL090980 seen in fig. 29 & 30 are seen to be affected by displacement by micro-faults. Faults represent brittle deformation of the sample; this could be due to shock from impact or shear forces within a brittle zone of the mantle of the UPB. Other meteorites, such as the CM chondrite Murchison have been recorded to contain brittle deformation that has been attributed to impact related events (Hanna et al., 2015). Murchison is seen to have a foliation alongside a rotational non-coaxial shear which has led authors to suggest the brittle deformation is impact related (Hanna et al., 2015). The veins in Murchison formed parallel to the foliation, and some contain a later generation of veins that cross-cut the first which suggests multiple deformation events (Hanna et al., 2015).

In Earth's mantle high temperature shear forces result in large shear zones 2-20 km thick as the degree of localisation of shear deformation decreases with increasing temperature and bulk strain (Drury et al., 1991). Rocks that have been deformed through shear forces usually have well defined foliations, lineations and crystallographic preferred orientations (Drury et al., 1991). Brittle deformation becomes limited at temperatures approaching 910±160°C at the maximum (Drury et al., 1991), with the brittle-ductile transition largely occurring at

approximately 600°C (Prieto et al., 2017). However polyphase rocks that contain 10-20% creep resistant phases (e.g. pyroxene) allows for brittle deformation to occur over a wider range of pressures and temperatures (Drury et al., 1991).

Samples which contain brittle fractures, such as MIL090980 and MIL090076 are unlikely to have formed at great depths within a large parent body, as brittle deformation would not occur at the temperatures of at least 900°C hypothesised by the large parent body theory presented by (Nabiei et al., 2018). Brittle deformation on Earth is restricted to only the top 100 km depth (McKenzie et al., 2005), below this the ductile regime becomes dominant which does result in fracturing. As the ureilites are sampling the mantle of the UPB for brittle failure to have occurred they would have to either be brought up from depth or have formed at shallow enough depths within the UPB for brittle regimes to be active.

However, these microfaults could have formed after exhumation by a previous significant impact that brought this sample up from depth and subsequently subjected it to brittle deformation. Due to the faults cross-cutting the veins, the fault must be related to a later deformation event. This means that the veins must have been emplaced during a previous event, cooled and a second event caused the faults to form. The radar plot based on analysis through ImageJ shown in fig. 30 shows that both carbon and iron rich veins in MIL090980 have similar preferred orientations. The majority are oriented at 340-170° with a smaller secondary peak at 40-220°, which could represent one stress field that changes orientation over time, or multiple stress fields formed the micro-faults. The veins being offset by these micro-faults indicate that a shearing mechanism may have been a component during the formation of these veins (Langenhorst et al., 2002).

5.4.1 Evidence for shock

Shock can be observed in olivine through a variety of features which correspond to different pressures. These levels have been outlined and updated for ordinary chondrites, carbonaceous chondrites and a variety of terrestrial and planetary compositions (Stöffler et al., 2018, 1991). Table 9 below outlines the main features observed in olivine at each stage and the corresponding pressure and temperature conditions.

Planar fractures are a feature observed in rocks classified at shock stage S3 and above by the system described by (Stöffler et al., 1991). They are parallel fractures within a single crystal with a spacing of up to tens of micrometres (Stöffler et al., 1991). Planar fracturing across olivine crystals in MIL090980, seen in fig. 32a-c is evidence that this sample has been shocked to at least shock stage S3 at some stage.

Novo Urei contains a twinned crystal of pyroxene, seen in fig. 39. This could be example of simple twinning, which in other non-ureilite samples has been considered a contributing factor to plastic deformation (Leroux et al., 2004). Twinning of clinopyroxenes is also considered characteristic of shock deformation (Müller, 1993). Mechanical twinning of Ca-rich clinopyroxene has been attributed to shock stage S4-S5 (Rubin, 2004). This suggests that Novo Urei may be more highly shocked than the other “typical (Goodrich, 1992)” ureilites: Kenna, Hajmah and MIL090076. EBSD analysis would be required to confirm either way.

Table 9: A summary of the different shock stages, the observed features in olivine at each stage and the estimated pressure/temperature conditions (Stöffler et al., 2018, 1991).

Shock Stage	Observed features	Pressure and temperature conditions
S1 (Unshocked)	Sharp optical extinction and irregular fractures.	<4-5 GPa and 20-50°C
S2 (Very weakly shocked)	Undulatory extinction and irregular fractures.	~5-10 GPa and 50-100°C
S3 (Weakly shocked)	Planar fractures, undulatory extinction and irregular fractures.	~15 GPa and 100-150°C
S4 (Moderately shocked)	Weak mosaicism and planar fractures.	~28-30 GPa and 250-300°C
S5 (Strongly shocked)	Strong mosaicism, planar fractures and planar deformation features.	~50-55 GPa and 650-850°C
S6 (Very strongly shocked)	Solid state recrystallisation and staining, melting and formation of Ringwoodite.	~60-70 GPa and 1500-1700°C
S7	Whole rock melt	

Table 10: Each of the samples used for this study with their assigned shock stage based on the classification system (Stöffler et al., 2018, 1991) and the features observed, listed in order of low to high shock.

Studied Sample	Shock stage	Observed features
MIL 090076	Low, no classification assigned.	No shock features observed.
Kenna	S2-S4	Pressures of 50-250kbar reported (Berkley et al., 1976).
Hajmah	Up to S3	Reported as highly shocked (Goodrich, 1992), however no shock features were discovered in the sample used in this study.
MIL 090980	At least S3	Planar Fractures.
Novo Urei	S4-S5	Twinned clinopyroxene.
Goalpara	S5-S6	Mosaicism of olivine.

5.4.2 Mosaicism

The IPF map of Goalpara seen in fig. 21 c & d shows the orientation of each crystal in the sample, this also highlights all the small subgrains that have different colours in the IPF map correlating to different crystallographic orientations. These subgrains can also be picked out in the cross polarised optical light image of Goalpara seen in fig. 17 which shows variable birefringence colours in distinct domains. These observations of Goalpara strongly match those features usually attributed to mosaicism.

Mosaicism is a texture where a single crystal is composed of multiple smaller crystallites whose crystal lattices are misoriented to each other (French and Koeberl, 2010), these

misorientations could be as high as 20° (Wang et al., 2018). Mosaicism specifically refers to solid state recrystallisation based on essentially shattering the crystal. The precise mechanism of mosaicism has not yet been constrained but it may be due to intense fracturing and plastic flow at the crystal structure scale (Wang et al., 2018). The domains of impact mosaicism may be plastic polygonization characterised by kink bands, slip bands and deformation lamellae; dynamic crystallisation characterised by subgrain rotation and dislocation glide; or static recrystallisation characterised by uniform grain sizes and grain boundaries of 120° (Wang et al., 2018).

The distinct subgrains and recrystallisation of the olivine crystals that are common features of mosaicism present throughout Goalpara indicates that this sample experienced the highest shock pressures out of the samples studied. Mosaicism of olivine would represent shock pressures of 15-65 GPa (Stöffler et al., 2018), however the pyroxene crystals do not show any evidence of mosaicism. The pyroxene crystals show more internal deformation within a single crystal in the GROD angle maps (fig. 21b) indicating they have not recrystallised and split into subgrains like the olivine but instead preserved the deformation that the original crystals experienced. Pyroxene mosaicises at ~20-70 GPa (Stöffler et al., 2018) so these two minerals in combination constrains the peak pressure of the impact to 15-~20GPa.

5.5 Annealing textures

Annealing is a process where a crystal lattice can 'repair' itself following a deformation event, such as shock. During deformation a crystal lattice and grain boundaries can be broken or defected, during annealing the atoms can migrate along lattice planes or via grain boundaries to allow for grains to grow again and increase in size (Karato, 1989).

The development of triple boundaries (seen in Hajmah in fig. 15b &c, Kenna in fig. 25a & b, MIL090076 in fig. 36 and Novo Urei in fig. 38) at ~120° indicates a high temperature event that was maintained for a long enough time to allow for textural equilibrium to be reached as his is the preferred texture of olivine crystals minimising the interfacial energy (Li et al., 2021). This would also allow for annealing to occur if the crystals previously suffered damage, annealing is the process where crystal lattices can begin to 'repair' themselves following shock deformation (Rubin, 2006, 2004). As the veins are emplaced along the boundaries of the olivine crystals this suggests the olivine had formed and reached equilbrium prior to emplacement of the veins. This is also shown in the relationships between the olivine crystals and the veins, the veins caused the olivine to reduce forming the rims however this reaction did not reach equilibrium as the olivine crystals are not uniform.

Ureilite olivines that have been described as mosaicised and annealed contained coarse aggregates with subgrains 10-20 μm across that join at triple boundaries of 120° (Rubin, 2006). The mosaicised olivine seen in Goalpara in this study seen in fig. 23 shows the triple boundaries but none of the subgrains approach the coarse sizes of 10-20 μm observed in other samples of goalpara by previous studies (Rubin, 2006). The formation of triple boundaries at 120° is evidence of annealing as this is the result of grain boundary migration and growth towards textural equilibirum (Ragan, 1969). The olivine mosaicism seen in Goalpara therefore likely occurred at a high enough temperature for the crystals to subsequently anneal or approach textural equilibrium.

5.6 Diamonds

Carbon in MIL090980 is present as both graphite and diamond. Graphite can be recognised by Raman spectroscopy through a peak at ~1580 cm^{-1} which is known as the G peak and a second peak may be present at 1350 cm^{-1} which is known as the D peak (Ferrari, 2007). A third peak at 1060 cm^{-1} can be seen if the graphite is amorphous (Ferrari, 2007) but this was not observed during this study. The higher the intensity of the D peak the more disordered and defected the graphite is considered to be (Ferrari, 2007). For good quality single crystals of graphite, no D peak would be observed (Pócsik et al., 1998; Jakubowski et al., 2011) and thus the ratio of D band intensity (I_d) over G band intensity (I_g) would be 0. Fig. 35a-c shows the Raman maps studied with the I_d/I_g value overlain. The average across all the graphite is 0.42 This means this sample does not contain perfectly crystalline graphite.

MIL090980 also contains diamonds as seen in the Raman spectroscopy data. Diamonds are hypothesised to be either grown at depth similar to Earth (Nabiei et al., 2018) or through shock transformation of graphite (Nestola et al., 2020). The FWHM of diamond has been studied for ureilites and other diamond containing meteorites previously. The lower the FWHM value the more crystalline the diamond is considered to be (Miyamoto et al., 1993).

A comparison of the spectra of diamonds formed by CVD processes, lab static growth and also those from the Canyon Diablo impact crater which are interpreted as shock diamonds has been reported (Miyamoto et al., 1993). Raman spectra has also been previously studied to suggest the grain sizes with an indication that the higher the intensity, and the closer the Raman shift is to 1332 cm^{-1} the larger the grain size (Namba et al., 1992). The scattering around 1332 cm^{-1} could represent the presence of nanodiamond, as spectra is known to shift when grain sizes get smaller and the FWHM value also tends to get larger (Miyamoto et al., 1993). Nanodiamonds studied across a variety of meteoritic and terrestrial samples show a Raman shift at 1325cm^{-1} and a FWHM of 10 cm^{-1} (Prawer et al., 2000) which represents a downward shift of 7cm^{-1} from the expected result for standard diamonds at 1332cm^{-1}. This shift is consistent with the experiemntally produced shift expected for particles that are around 5 nm in size (Prawer et al., 2000). Very small diamond crystals may indicate fragmented diamond, Almahata Sitta MS-170 has been reported to contain fragmented diamond with similar crystallographic orientations (Miyahara et al., 2015). This has been interpreted as representing a former large diamond crystal which became fragmented during impact (Miyahara et al., 2015). Almahata Sitta MS-170 is considered a lower shocked ureilite (S3 (Bischoff et al., 2010; Miyahara et al., 2015)) so the large diamonds may be unlikely to have formed through shock if the max shock pressures the sample experienced were ~15GPa (Stöffler et al., 2018). However, it is important to consider the discussion around catalysis (Nestola et al., 2020)which could potentially reduce the pressures required to form diamond and has also been reported to allow for nitrogen zoning without a sluggish growth rate (zonation was formed in 15-20s in lab conditions (Nestola et al., 2020)).

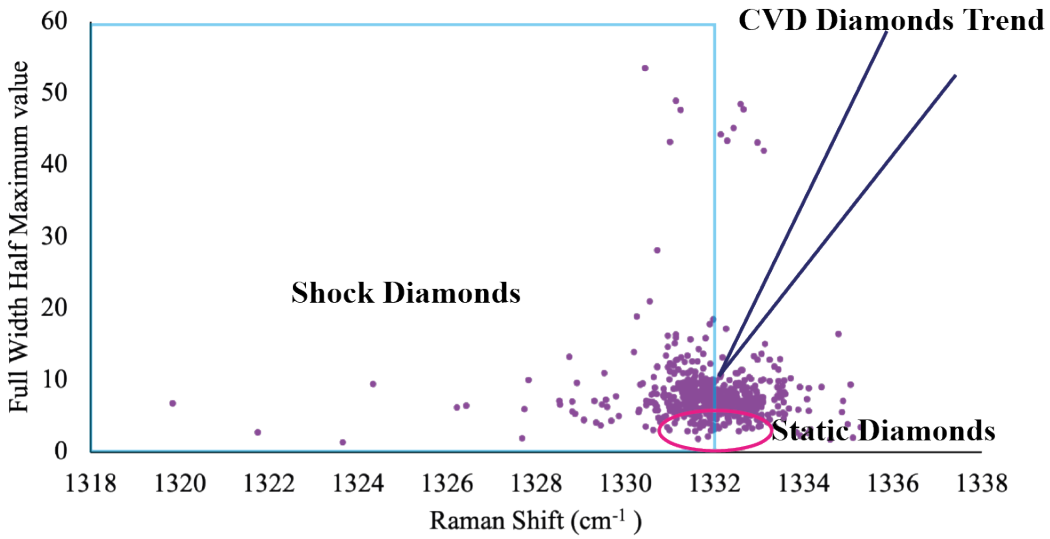

Figure 44: Summary diagram of all the FWHM data collected from any Raman peak identified as a diamond signal. Overlain is the areas where diamonds were measured to plot when formed through experimental CVD, terrestrial growth diamonds (Static diamonds) and known shock produced diamonds from Miyamoto et al., 1993. Please note the shock field is likely to extend to higher Raman shifts, however the paper this figure is based on only showed them up to 1332 cm^{-1}.

Diamonds formed in Earths mantle show a Raman peak at 1332 cm^{-1} and have a FWHM value of 2-4.5 cm^{-1} (Goresy et al., 2001; Miyamoto et al., 1993). CVD diamonds tend to have a larger FWHM value of ~10-20 cm^{-1} (Goresy et al., 2001). The diamonds in this study have FWHM values higher than 5 cm^{-1},seen in fig, 35 & 44, in the majority of data points, suggesting they are not formed from high static pressures. They are also unlikely to be CVD related as the FWHM is not high enough.

The results of the Raman study of diamond show clear evidence that the majority of diamonds in MIL090980 did not form through static high pressures similar to those on Earth. This is due to the very well constrained window of FWHM vs Raman shift plots that terrestrial diamonds plot at, which very few of the ureilite diamonds from this study plot within. The presence of diamonds that have Raman features consistent with shock alongside brittle deformation seen in the microfaults affecting the veins strongly suggests a shock origin for the brittle fractures. This does not completely disprove the theory that the UPB was a large planetesimal, as MIL090980 could be sampling a shallow portion of the UPB mantle.

The presence of some diamonds from this study plotting within the expected range for static high pressure diamonds means we cannot conclusively say none of these diamonds are from high pressure and instead are all produced by shock. It could be concluded that the UPB and MIL090980 contained both static high pressure diamonds at great depth but also produced diamonds during a large shock event. Prevoius studies of diamonds within ureilites, particularly Almahata Sitta MS-170, have shown zoning of nitrogen zoning within the diamonds (Miyahara et al., 2015) . This chemical zoning indicates sluggish growth of the diamonds, this feature is seen in terrestrial static diamonds but is otherwise not reported in shock produced diamonds (Miyahara et al., 2015). If MIL090980 was a sample originating at shallower depths of the UPB it would make sense that the majority of the diamonds would be

the ones produced during shock, with only a small percentage of the diamonds grown at depth.

5.7 Evidence for shear

The grains within Kenna (fig. 24) have curved boundaries that are similar to those seen in mylonitic rocks on Earth, MIL090076 (fig. 36) also has crystals with curved boundaries like Kenna, which suggests a shear component was present during the growth of these rocks. The Kenna ureilite has been reported to contain equigranular olivine and pyroxene, which show a preferred orientation along the long shape axis representing a strong lineation and when seen in 3D is a weakly defined foliation (Berkley et al., 1976). Novo Urei, Haverö and Dylapur have also been reported to contain this same preferred mineral orientation (Berkley et al., 1980). Studies of the lineation of Dyalpur (Berkley et al., 1980) parallels a separate study of Kenna (Berkley et al., 1976) which strongly indicate the foliation runs along the (100) crystal face of the olivine and the lineation is along the crystallographic c-axis (Berkley et al., 1980), this is also observed in the sample Dingo Pup Donga (Berkley et al., 1980).

The IPF map of Kenna (fig. 26c) shows lots of crystals in purple and green which suggests the crystals all preferentially lining up in preferred orientations thus having the same orientation relative to the sample surface. The disorientation axes plot in sample co-ordinate space for Kenna (fig. 27) and Goalpara (fig. 22) have a point maxima which is indicative of a cumulate or shear component (Griffin et al., 2022a) present for the formation of this rock. This feature is also seen in disorientation axis plots for MIL090980, fig. 33, however it is much weaker as there is no red seen in the point maxima.

Kenna also displays the poikilitic texture of pyroxene enclosing the olivine, this is seen best in fig. 26a where a large (~2 mm) pyroxene grain is completely surrounding a fine (<0.5 mm) olivine crystal. This textural relationship was originally interpreted as olivine forming first as a cumulus mineral and the pyroxene forming later as a post-cumulus mineral (Berkley et al., 1976). Later evaluation indicates that solid state boundary adjustments through recrystallisation could produce ‘bulges’ of one mineral inside another and appear similar to a poikilitic texture (Berkley et al., 1980; Berkley, 1986).

5.8 Phase Heritage

Phase heritage is a concept based on certain minerals converting to their high-pressure polymorphs during a high-pressure event e.g. shock (White et al., 2018)and then reverting back during decompression but retaining textures and features of the polymorph, particularly noticeable in CPO’s from EBSD analysis (Cayron et al., 2006; Timms et al., 2017).

The contoured pole figures for grains within Goalpara (fig. 23b) show a 4-point cruciform pattern could be representative of a high-pressure phase transition (Timms et al., 2017) from ringwoodite (cubic) to olivine (orthorhombic) with olivine being the current phase. If this is the case that would mean the UPB would have to be sizeable enough for a mantle transition zone to occur which has the optimal pressures and stability for ringwoodite formation, on Earth this is below ~660 km (Katsura and Ito, 1989; Suzuki et al., 2000). Goalpara is the only sample in this suite to show this texture however so not all ureilites would be sampling this zone. This is then unusual as to why all samples share so many characteristics (e.g. mineralogy, reaction rims, triple boundaries and carbon content), this is especially detrimental to the theories whereby all ureilites are sourced from the same region of their

parent body. If this scenario is true then the carbon material causing the reaction rims would have to be synonymous with disruption as the crystals would have to be brought up from depth, the drop in pressure then causing a phase transition to olivine which then are exposed to the carbon and form reaction rims.

This opens up further questions into the impactor, if the impactor was carbonaceous chondrite material as previously suggested (Goodrich et al., 2004; van Kooten et al., 2017; Warren and Kallemeyn, 1989) then this is unlikely to have completely destroyed such a large planestimal. Carbonaceous chondrite parent bodies have been calculated based on fluid pore pressure studies to be ~20-120 km diameter (Young, 2001; Young et al., 2003) which would be very unlikely to destroy a planet large enough to have internal conditions that are favourable for ringwoodite formation.

Alternatively, there could have been a transition from olivine → ringwoodite → olivine during and immediately after an impact. If this is the case the shock pressure would be up to ~25 GPa for ringwoodite formation at peak pressure (Okuchi et al., 2021). However with such a large impact more shock evidence would be expected such as vast quantities of shock melt and for the pyroxene grains to have recrystallised (Stöffler et al., 2018, 1991). The pyroxene grains show no evidence of recrystallisation as they have retained the evidence of plastic deformation seen in the GROD angle maps (fig. 13).

However, the plotted data that creates the contoured pole figure (fig. 45) shows that instead of 4 distinct points, it is in fact more of a donut shape. This shape may represent a series of symmetrical rotations which would be indicative of shock processes (Timms et al., 2017) or complex shear (Warren et al., 2008) in that portion of the UPB. Again, this raises the same issue of why only this one sample is representing a complex shear zone in this pattern whilst all the others do not. Shear features have been recognised in the disorientation axis plots (fig. 22) as discussed above.

Alternatively, these rotations could be due to the shattered olivine crystal going through a process of annealing. Annealing has been discussed above and does appear to have occurred in the shattered crystals of Goalpara as the subgrains are joined at triple junctions approaching 120° (fig. 23ai). Assuming the simplest explanation is usually true, this cruciform pattern would be formed through shock processes causing shattering of the crystals and subsequent annealing creating the symmetrical rotations. Goalpara is known as a highly shocked ureilite and this particular sample exhibits shock stages of at least shock stage S4 if not S5 (Stöffler et al., 2018, 1991).

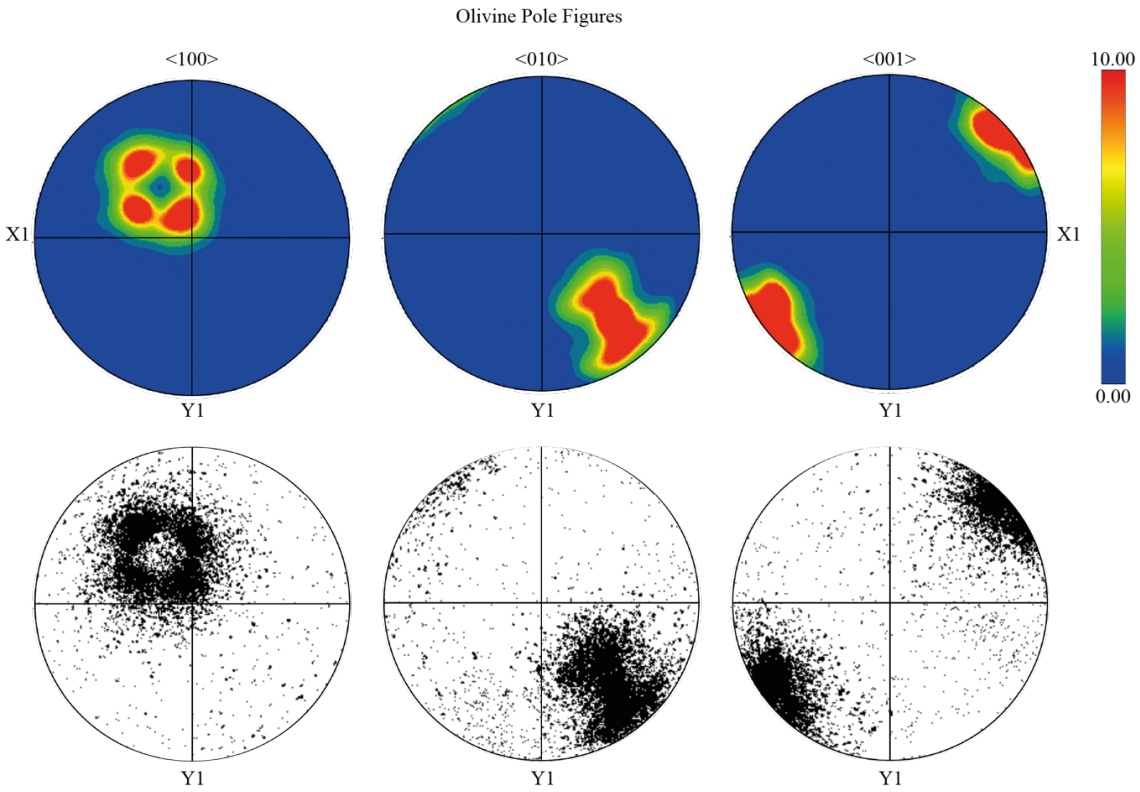

Figure 45: Combination image showing the same contoured pole figures presented in fig. 23 with the scattered plots below showing the locations of the data points.

5.9 Crystallographic preferred orientations

Pole figures can be generated for EBSD data sets that can show whether there is random texture, a foliation fabric or lineation throughout the sample, and crystal rotation axis diagrams can be generated to determine the slip systems that may have been active during deformation events. A lineation is expressed in a CPO pole figure as a point maxima whilst a foliation appears as a girdle.

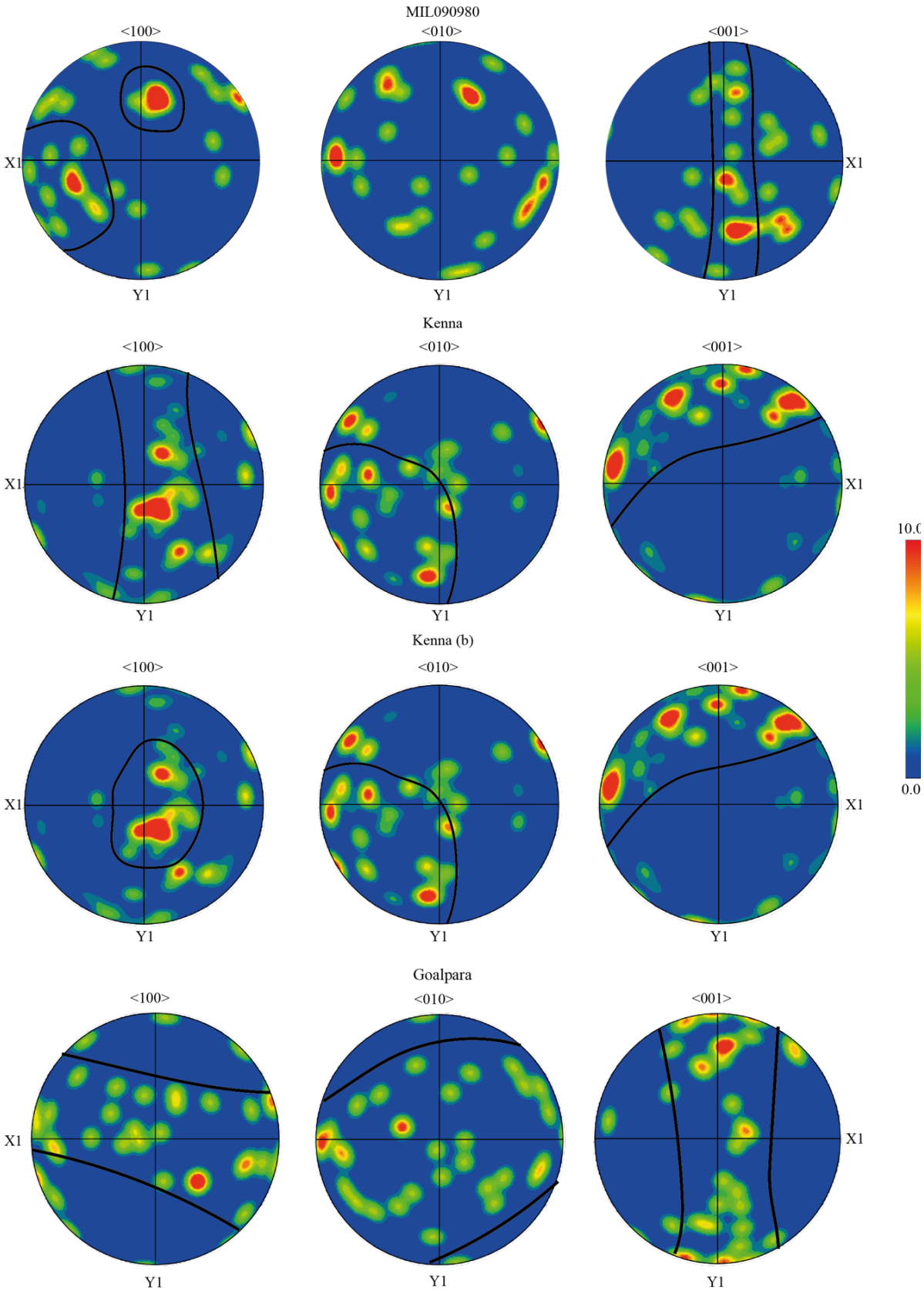

Figure 46: Combination of one point per grain CPO's for each sample seen previously in the results section (fig. 22, 27 & 33) with annotations highlighting where there is a girdle (lines) and where there is a point maxima (circles).

The CPO fabrics shown in fig. 22, 27 & 33 vary between lineation and foliation. Goalpara (fig. 22 & 47) shows a girdle in all three miller indices which indicates a strong foliation present throughout this sample. Kenna could be interpreted in several ways, there is a girdle in <001> and a diffuse point maxima in <010> but the position of the points in <100> could be interpreted as a diffuse point maxima also (fig. 46 Kenna b), or as a weak girdle (fig. 46 Kenna). MIL090980 (fig. 33 & 46) shows two point maximas in <100>, a completely random pattern in <010> and a girdle in <001>. This also indicates a foliation is present within MIL090980, foliations tend to represent pure shear and compaction processes occurring within the sample (Griffin et al., 2022a). However, MIL090980 is complicated as the point maxima in <100> is indicative of a lineation and simple shear gravitationally driven crystal settling (Griffin et al., 2022a).

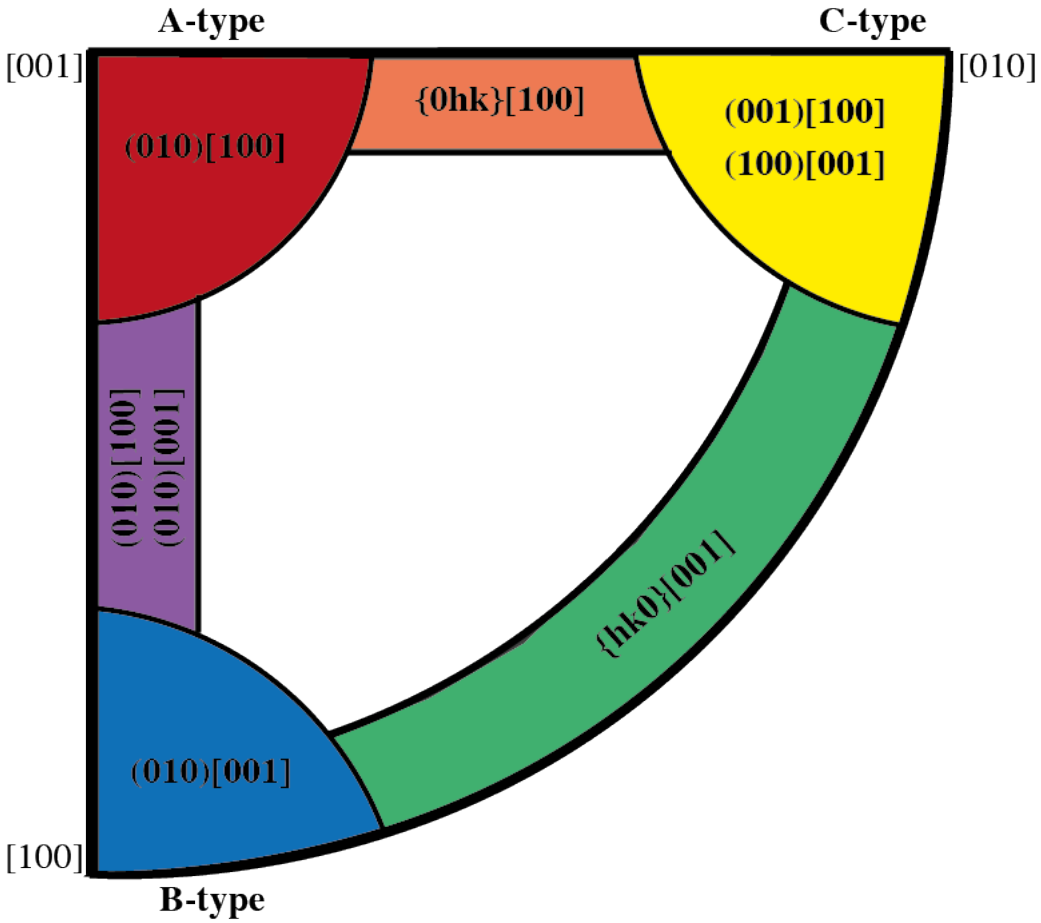

Figure 47: Summary of olivine slip systems and their associated environments that can be identified using crystal rotation axis plots the colours are related to the temperature that the slip system is active where warmer colours reflect higher temperatures. Figure adapted from (Ruzicka and Hugo, 2018) using information found in (Griffin et al., 2022b; Karato et al., 2008).

Different slip systems in olivine can be activated during deformation and the fabrics that each slip system is associated with, which correspond to different modes of deformation e.g. shear. Fig. 47 summarises the slip systems in olivine that can be activated during deformation, and what fabrics they are associated with. These slip systems are with regards to common Miller indices within olivine crystals. Miller Indices identify parallel planes within a crystal lattice

and are represented by the information contained within round brackets e.g. (001) (Ashworth and Barber, 1975). Information contained within curly brackets, e.g {hk0}, represents the plane plus those that are equivalent by symmetry (Ashworth and Barber, 1975). Information in square brackets, e.g. [001], represents the lattice vector or direction of the slip system (Ashworth and Barber, 1975).

A-type slip is predominant in Earth's lithosphere where there is low water content with moderate stress (~50-350 MPa (Karato et al., 2008)) and moderate temperatures (Karato et al., 2008) above ~700°C (Ruzicka and Hugo, 2018). B-type fabrics are characterised by an α-axis oriented in the direction perpendicular to flow, and on Earth are typically found in mantle wedge environments where there is an abundance of water (Tasaka et al., 2008). B-type deformation typically occurs under high stress (~400 MPa) and a water content of ~1500-3000 ppm(H/Si) (Bernard et al., 2019) however it should be noted that previous deformation events and original rock texture can also influence which slip system is activated (Bernard et al., 2019). Some experiments have shown B-type slip can occur under high pressure, lower temperature and grain boundary sliding (Bernard et al., 2019). In asthenospheric conditions (low (<600 °C (Ruzicka and Hugo, 2018)) temperature and low stress, with an increase in water content compared to A-type) the dominant slip system is C-type (Karato et al., 2008).

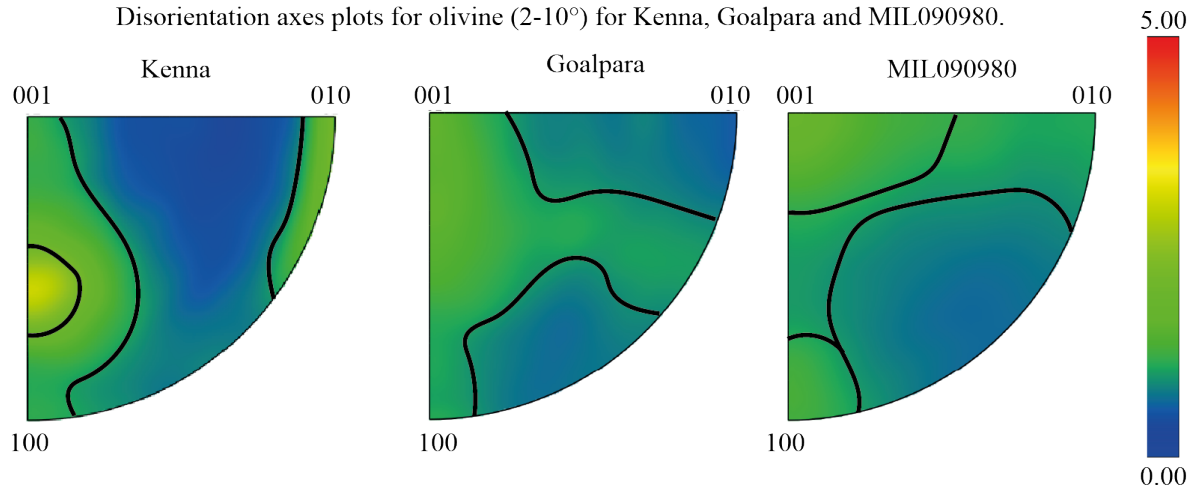

Figure 48: Figure showing the disorientation axis plots in crystal co-ordinates for olivine showing disorientation of 2-10°. These individual axes plots are seen previously in the results section (fig. 22, 27 & 33); however, the three samples have been combined here for ease of comparison. Annotations have been added to highlight the regions which show the most activity.

The pole figures for Kenna shown in fig. 27 & 48 show movement between A-type and B-type demonstrated in the whole left hand side of the disorientation axis in green. There is a bulge slightly above the corner corresponding to B-type slip and the green colour can also be seen in the region corresponding to C-type slip. The green colour appearing in these regions indicate an active slip system in (010)[100] or (010)[001] as demonstrated by the large point maxima in the area corresponding to this slip system in fig. 47 as well as in the (001)[100] or (100)[001]. A slip system in (010)[100]/(010)[001] indicates a transition between A-type and B-type slip, likely during an event where the pressure gets increased causing this transition to begin. The other slip system present ((001[100] or (100)[001]) is indicative of C-type slip suggesting an initial low temperature (below 700°C (Ruzicka and Hugo, 2018)) and low pressure deformation event (Ruzicka and Hugo, 2018), however this point in the deformation

axis is spreading down and curving towards {hk0} slip which happens as temperatures start to increase. A-type slip starts to occur at temperatures above 700°C and becomes the dominant slip system at 900-1000°C (Ruzicka and Hugo, 2018). The A-type slip shows the weakest green colour it does not appear to have been an extensive system which suggests Kenna did not reach the peak A-type slip temperatures of 900-1000°C. However, the temperatures at which different slip systems get activated is dependent on factors other than temperature, for example the transition between C-type and A-type slip can occur at lower temperatures if the pressure is increased and at higher temperatures if the strain rate is increased (Ruzicka and Hugo, 2018). C-type slip is also prominent in environments where there is a high water content, regardless of the temperatures (Karato et al., 2008; Ruzicka and Hugo, 2018), although this is not hugely relevant for the ureilites as they are water depleted compared to Earth (Peterson et al., 2022) so it is unlikely the water content played a huge role in the activation of slip systems. The deformation event that caused the B-type deformation is likely overprinting these previous fabrics, and as it is a high pressure slip system this could have been a shock event. The C-type slip shown in Kenna appears to be more prominent for crystal co-ordinates between 5-10° shown as the distinct red region in fig. 27.

Goalpara disorientation axes (fig. 22) shows a predominant slip system in (010)[100] which is consistent with A-type slip, however this point is also creeping towards B-type slip and there is also some colour in the region indicating {hk0}[001]. These microstructures reflect a transition from a moderate stress and moderate temperature deformation to a high-pressure deformation (Griffin et al., 2022a; Ruzicka and Hugo, 2018), this could also be a shock related overprinting fabric like that seen in Kenna. There is a lack of any colour in the top right-hand corner (fig. 22) indicating no C-type slip present in Goalpara. This is a clear difference between Goalpara and the other samples as they both show clear evidence of C-type slip (fig. 47). The lack of any C-type slip present in Goalpara suggests this sample did not experience low stress deformation (Karato et al., 2008), this would be consistent with other observations for Goalpara including the high shock stage and mosaicism observed (fig. 21) which indicate this sample experienced very high pressures. This would also explain why there is a trend from A-type towards B-type slip. The transition between C-type slip towards {hk0}[001] occurs at less than 11 GPa (Mainprice et al., 2005) this constrains the minimum pressure that Goalpara experienced.

Disorientation axes for MIL090980 show an active slip system in the regions for A-type, B-type and C-type. A-type and C-type appear to be connected, shown in fig. 33 as the green colour continues across the top of that axis between the two so this could be a transitional texture showing a deformation event that increases in temperature with a decrease in pressure moving from A-type to C-type. The B-type deformation event may be separate from these as this is seen as a separate point on the axis. The B-type slip appears to be occurring strongest in the crystal co-ordinates between 5-10° show by the yellow region in the disorientation axis in fig. 33. B-type slip is also high pressure so may represent a shock overprinting which is separate from the A and C-type slip representing gradual increases in temperature.

Table 11: Summary table displaying key EBSD results and shock stages for the samples studied.

Sample	Shock Stage (using (Stöffler et al., 2018) classification)	Olivine Slip System	Deformation Type	Average internal misorientation	Maximum internal misorientation
Hajmah	Up to S3	No EBSD	No EBSD	No EBSD	No EBSD
Goalpara	S5-S6	(010)[100]	A and B	1.89°	14.16°
Kenna	S2-S4	(001)[100] or (100)[001]	A, B and C	1.1°	15.88°
MIL 090980	At least S3	(010)[001]	A, B and C	1.0°	11.95°
MIL 090076	Low, no classification assigned	No EBSD	No EBSD	No EBSD	No EBSD
Novo Urei	S4-S5	No EBSD	No EBSD	No EBSD	No EBSD

6.0 Conclusion

In summary of the various avenues of ureilite petrogenesis explored through this thesis the following geological history is suggested.

Firstly the ureilites formed as a mantle restite (Bischoff et al., 2014; Broadley et al., 2020) of a planetesimal accreting during the early Solar System, this work has not explored either the age of accretion/disruption nor the size of the UPB however previous research presented earlier in this thesis indicates a strong consensus amongst the ureilite community that initial formation occurred at 4.5-4.6 Ga (Takahashi and Masuda, 1990) or ~1.6 Myr after CAI formation (Budde et al., 2015). Later impact or igneous events have been dated at 4.1Ga (Takahashi and Masuda, 1990) and 3.74 Ga (Goodrich et al., 1991). Due to oxygen fugacity calculations, again from previous authors work presented in the introduction to this thesis the minimum size requirement for the UPB is ~125km (Goodrich et al., 2004) diameter with many theories suggesting much larger parent bodies up to the size of Mercury-Mars (Nabiei et al., 2018).

It is possible that at this stage the ureilites experienced the shear forces that are seen in the disorientation axis plots (fig. 22, 27 & 33) as they could be due to internal forces as the planetesimal is forming, however the timing of this is unconstrained and could also be shock related.

Following initial formation, the UPB did not survive as a planetesimal and was catastrophically disrupted (Goodrich et al., 2015). Brittle failure would occur at this stage creating cracks in certain samples for vein formation across samples and surrounding silicate crystal grains, this means a fluid and a carbon component would have to be either added or mobilised at this stage leading to the formation of reaction rims on the olivine (fig. 15 & 25).

Original graphite crystals would also undergo a phase transformation to diamond at this point demonstrated by the Raman data indicating shock origin for the majority of the diamonds found within MIL090980 (fig. 44). Due to the overlap of the Raman data collected and the static diamond data presented for comparison it cannot be ruled out that some diamonds may have already been present and formed at high static pressures at depth within the UPB. If this is the case, then MIL090980 would initially have sampled this deeper region before being excavated during impact. This catastrophic impact would also cause the mosaicism of the olivine grains in Goalpara (fig. 21 & 23) and cause the rotations seen in olivine grains in EBSD pole figures (fig. 22), the fact that Goalpara shows features of at least shock stage S5 (table 9 (Stöffler et al., 2018)) whilst all other samples studied cannot be higher than shock stage S3 (table 9 (Stöffler et al., 2018)) (due to lack of mosaicism (Stöffler et al., 2018)) indicates Goalpara samples a region of the UPB that was much closer to the impact site than the others.

Following disruption, the olivine crystals must have remained at high temperatures for long enough to display some annealing. The timing of this is constrained by the mosaicisied grains in Goalpara also showing evidence of annealing (triple boundaries, fig. 23ai) which means the mosaicism must have occurred prior to the sustained high temperatures in order to allow the conditions for which annealing can occur. This is also consistent with the crystal rotation axis data (fig. 22) indicating high temperature deformation. Following this there would have been a period of cooling to the stage where the veins are fully crystallised then there must have been at least one smaller impact causing the brittle failure observed in MIL090980 where the veins are offset and demonstrating micro-faults. This feature is not observed in all the samples studied which suggests it is a local feature dependent on which daughter asteroid the samples re-accreted into following UPB breakup.

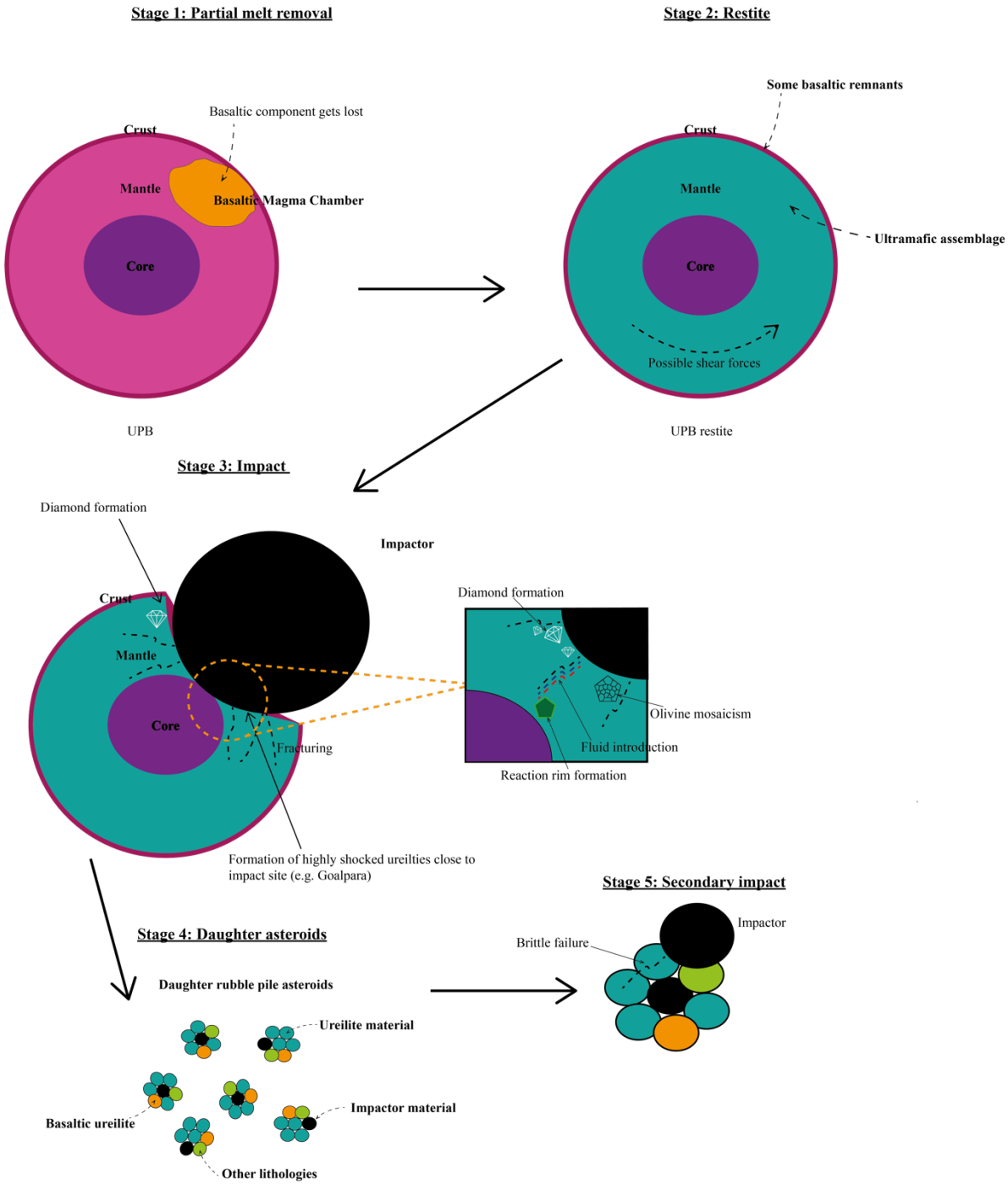

Figure 49: Cartoon schematic of key stages of ureilite formation.

6.1 Follow up work

The work presented in this thesis provides a baseline for further study, particularly in the areas of characterising the mosaicism in Goalpara and the diamonds in MIL090980. For both areas a larger sample size would benefit the results and enhance the interpretation of the features, especially for mosaicism as this is not a common feature across ureilites.

More work can be done on observing the mosaicism through EBSD and gaining higher resolution EBSD data for the grains that demonstrate potential phase transition between ringwoodite and olivine. If this phase transition did in fact take place in the ureilite group this

would be incredibly beneficial to constraining either the size of the UPB, and thus be useful in the diamond discussion also, or the conditions of catastrophic impact.

More work could also be done on the diamond question, only a small sample size was used for thus study due to timing constraints however a much more thorough Raman analysis combined with high resolution SEM imaging to see the shapes of the diamonds could provide much more conclusive evidence for how the diamonds formed in this sample.

7.0 Acknowledgments

The author would like to acknowledge the following people and institutions for their assistance in the research presented for this thesis.

Thanks to the supervisory team consisting of Dr Luke Daly and Prof. Martin Lee at the University of Glasgow for supervising and supporting this piece of work.

Thanks to the Natural History Museum in London, NASA and the Smithsonian Museum for loaning the samples used in this study.

Thanks to Dr John Faithfull and the Hunterian Museum for allowing the use of their optical microscope for imaging used in this study.

Thanks to Mr Peter Chung, Dr Liene Spruženiece and the ISAAC facility at the University of Glasgow for allowing the use of the machinery and assistance with SEM, EDS, EBSD and Raman data collection.

Thanks to Mr Cameron Floyd for training on how to collect and analyse Raman data.

Thanks to Dr Annemarie Pickersgill for assistance with optical microscopy data collection.

Bibliography:

Ashworth, J.R., Barber, D.J., 1975. Electron petrography of shock-deformed olivine in stony meteorites. *Earth Planet Sci Lett* 27, 43–50. https://doi.org/10.1016/0012-821X(75)90158-2

Barbaro, A., Domeneghetti, M., Goodrich, C., Meneghetti, M., Litti, L., Fioretti, A., Jenniskens, P., Shaddad, M., Nestola, F., 2020. Graphite-Based Geothermometry on Almahata Sitta Ureilitic Meteorites. *Minerals* 10, 1005. https://doi.org/10.3390/min10111005

Barbaro, A., Nestola, F., Pittarello, L., Ferrière, L., Murri, M., Litasov, K.D., Christ, O., Alvaro, M., Domeneghetti, M.C., 2022. Characterization of carbon phases in Yamato 74123 ureilite to constrain the meteorite shock history. *American Mineralogist* 107, 377–384. https://doi.org/10.2138/am-2021-7856

Barrat, J.-A., Jambon, A., Yamaguchi, A., Bischoff, A., Rouget, M.-L., Liorzou, C., 2016. Partial melting of a C-rich asteroid: Lithophile trace elements in ureilites. *Geochim Cosmochim Acta* 194, 163–178. https://doi.org/10.1016/j.gca.2016.08.042

Barrat, J.-A., Sansjofre, P., Yamaguchi, A., Greenwood, R.C., Gillet, P., 2017. Carbon isotopic variation in ureilites: Evidence for an early, volatile-rich Inner Solar System. *Earth Planet Sci Lett* 478, 143–149. https://doi.org/10.1016/j.epsl.2017.08.039

Berkley, J.L., Brown, H.G., Keil, K., Carter, N.L., Mercier, J.-C.C., Huss, G., 1976. The Kenna ureilite: an ultramafic rock with evidence for igneous, metamorphic, and shock origin. *Geochim Cosmochim Acta* 40, 1429–1437. https://doi.org/10.1016/0016-7037(76)90079-X

Berkley, J.L., Jones, J.H., 1982. Primary igneous carbon in ureilites: Petrological implications. *J Geophys Res* 87, A353. https://doi.org/10.1029/JB087iS01p0A353

Berkley, J.L., Taylor, G.J., Keil, K., Harlow, G.E., Prinz, M., 1980. The nature and origin of ureilites. *Geochim Cosmochim Acta* 44, 1579–1597. https://doi.org/10.1016/0016-7037(80)90119-2

Bernard, R.E., Behr, W.M., Becker, T.W., Young, D.J., 2019. Relationships Between Olivine CPO and Deformation Parameters in Naturally Deformed Rocks and Implications for Mantle Seismic Anisotropy. *Geochemistry, Geophysics, Geosystems* 20, 3469–3494. https://doi.org/10.1029/2019GC008289

Bhandari, N., Shah, V.G., Graham, A., 1981. THE LAHRAULI UREILITE. *Meteoritics* 16, 185–191. https://doi.org/10.1111/j.1945-5100.1981.tb00542.x

Birtel, S., Stöckhert, B., 2008. Quartz veins record earthquake-related brittle failure and short term ductile flow in the deep crust. *Tectonophysics* 457, 53–63. https://doi.org/10.1016/j.tecto.2008.05.018

Bischoff, A., Goodrich, C.A., Grund, T., 1999. Shock-Induced Origin Of Diamonds In Ureilites, in: Lunar and Planetary Science Conference. p. 1100.

Bischoff, A., Horstmann, M., Barrat, J.-A., Chaussidon, M., Pack, A., Herwartz, D., Ward, D., Vollmer, C., Decker, S., 2014. Trachyandesitic volcanism in the early Solar System. *Proceedings of the National Academy of Sciences* 111, 12689–12692. https://doi.org/10.1073/pnas.1404799111

Bischoff, A., Horstmann, M., Pack, A., Laubenstein, M., Haberer, S., 2010. Asteroid 2008 TC3-Almahata Sitta: A spectacular breccia containing many different ureilitic and chondritic lithologies. *Meteorit Planet Sci* 45, 1638–1656. https://doi.org/10.1111/j.1945-5100.2010.01108.x

Bons, P.D., Elburg, M.A., Gomez-Rivas, E., 2012. A review of the formation of tectonic veins and their microstructures. *J Struct Geol* 43, 33–62. https://doi.org/10.1016/j.jsg.2012.07.005

Bouvier, A., Wadhwa, M., 2010. The age of the Solar System redefined by the oldest Pb–Pb age of a meteoritic inclusion. *Nat Geosci* 3, 637–641. https://doi.org/10.1038/ngeo941

Boynton, W.V., Starzyk, P.M., Schmitt, R.A., 1976. Chemical evidence for the genesis of the ureilites, the achondrite Chassigny and the nakhlites. *Geochim Cosmochim Acta* 40, 1439–1447. https://doi.org/10.1016/0016-7037(76)90080-6

Brantut, N., Heap, M.J., Baud, P., Meredith, P.G., 2014. Rate- and strain-dependent brittle deformation of rocks. *J Geophys Res Solid Earth* 119, 1818–1836. https://doi.org/10.1002/2013JB010448

Broadley, M.W., Bekaert, D. v., Marty, B., Yamaguchi, A., Barrat, J.-A., 2020. Noble gas variations in ureilites and their implications for ureilite parent body formation. *Geochim Cosmochim Acta* 270, 325–337. https://doi.org/10.1016/j.gca.2019.11.032

Brownlee, D., 2014. The Stardust Mission: Analyzing Samples from the Edge of the Solar System. *Annu Rev Earth Planet Sci* 42, 179–205. https://doi.org/10.1146/annurev-earth-050212-124203

Brownlee, D.E., 2003. Stardust: Comet and interstellar dust sample return mission. *J Geophys Res* 108, 8111. https://doi.org/10.1029/2003JE002087

Bryson, J.F.J., Nichols, C.I.O., Herrero-Albillos, J., Kronast, F., Kasama, T., Alimadadi, H., van der Laan, G., Nimmo, F., Harrison, R.J., 2015. Long-lived magnetism from

solidification-driven convection on the pallasite parent body. *Nature* 517, 472–475. https://doi.org/10.1038/nature14114
Budde, G., Kruijer, T.S., Fischer-Gödde, M., Irving, A.J., Kleine, T., 2015. Planetesimal differentiation revealed by the Hf–W systematics of ureilites. *Earth Planet Sci Lett* 430, 316–325. https://doi.org/10.1016/j.epsl.2015.08.034
Buening, D.K., Buseck, P.R., 1973. Fe-Mg lattice diffusion in olivine. *J Geophys Res* 78, 6852–6862. https://doi.org/10.1029/JB078i029p06852
Carter, N.L., Raleigh, C.B., DeCarli, P.S., 1968. Deformation of olivine in stony meteorites. *J Geophys Res* 73, 5439–5461. https://doi.org/10.1029/JB073i016p05439
Cayron, C., Artaud, B., Briottet, L., 2006. Reconstruction of parent grains from EBSD data. *Mater Charact* 57, 386–401. https://doi.org/10.1016/j.matchar.2006.03.008
Chen, L., Xu, J., Chen, J., 2015. Applications of scanning electron microscopy in earth sciences. *Sci China Earth Sci* 58, 1768–1778. https://doi.org/10.1007/s11430-015-5172-9
Clark, B.E., Ockert-Bell, M.E., Cloutis, E.A., Nesvorny, D., Mothé-Diniz, T., Bus, S.J., 2009. Spectroscopy of K-complex asteroids: Parent bodies of carbonaceous meteorites? *Icarus* 202, 119–133. https://doi.org/10.1016/j.icarus.2009.02.027
Clayton, R.N., Mayeda, T.K., 1996. Oxygen isotope studies of achondrites. *Geochim Cosmochim Acta* 60, 1999–2017. https://doi.org/10.1016/0016-7037(96)00074-9
Clayton, R.N., Mayeda, T.K., 1988. Formation of ureilites by nebular processes. *Geochim Cosmochim Acta* 52, 1313–1318. https://doi.org/10.1016/0016-7037(88)90286-4
Clayton, R.N., Mayeda, T.K., Goswami, J.N., Olsen, E.J., 1991. Oxygen isotope studies of ordinary chondrites. *Geochim Cosmochim Acta* 55, 2317–2337. https://doi.org/10.1016/0016-7037(91)90107-G
Collinet, M., Grove, T.L., 2020a. Formation of primitive achondrites by partial melting of alkali-undepleted planetesimals in the inner solar system. *Geochim Cosmochim Acta* 277, 358–376. https://doi.org/10.1016/j.gca.2020.03.004
Collinet, M., Grove, T.L., 2020b. Incremental melting in the ureilite parent body: Initial composition, melting temperatures, and melt compositions. *Meteorit Planet Sci* 55, 832–856. https://doi.org/10.1111/maps.13471
Colpan, C.O., Nalbant, Y., Ercelik, M., 2018. 4.28 Fundamentals of Fuel Cell Technologies, in: Comprehensive Energy Systems. Elsevier, pp. 1107–1130. https://doi.org/10.1016/B978-0-12-809597-3.00446-6
Daly, L., Lee, M.R., Piazolo, S., Griffin, S., Bazargan, M., Campanale, F., Chung, P., Cohen, B.E., Pickersgill, A.E., Hallis, L.J., Trimby, P.W., Baumgartner, R., Forman, L. v., Benedix, G.K., 2019. Boom boom pow: Shock-facilitated aqueous alteration and evidence for two shock events in the Martian nakhlite meteorites. *Sci Adv* 5. https://doi.org/10.1126/sciadv.aaw5549
Das, R.S., Agrawal, Y.K., 2011. Raman spectroscopy: Recent advancements, techniques and applications. *Vib Spectrosc* 57, 163–176. https://doi.org/10.1016/j.vibspec.2011.08.003
Day, J.M.D., Corder, C.A., Cartigny, P., Steele, A., Assayag, N., Rumble, D., Taylor, L.A., 2017. A carbon-rich region in Miller Range 091004 and implications for ureilite petrogenesis. *Geochim Cosmochim Acta* 198, 379–395. https://doi.org/10.1016/j.gca.2016.11.026
de Hoog, J.C.M., Gall, L., Cornell, D.H., 2010. Trace-element geochemistry of mantle olivine and application to mantle petrogenesis and geothermobarometry. *Chem Geol* 270, 196–215. https://doi.org/10.1016/j.chemgeo.2009.11.017
Delaney, J.S., Takeda, H., Prinz, M., Nehru, C.E., Harlow, G.E., 1983. THE NOMENCLATURE OF POLYMICT BASALTIC ACHONDRITES. *Meteoritics* 18, 103–111. https://doi.org/10.1111/j.1945-5100.1983.tb00581.x

Downes, H., Mittlefehldt, D.W., Kita, N.T., Valley, J.W., 2008. Evidence from polymict ureilite meteorites for a disrupted and re-accreted single ureilite parent asteroid gardened by several distinct impactors. *Geochim Cosmochim Acta* 72, 4825–4844. https://doi.org/10.1016/j.gca.2008.06.028

Drury, M.R., Vissers, R.L.M., van der Wal, D., Hoogerduijn Strating, E.H., 1991. Shear localisation in upper mantle peridotites. *Pure Appl Geophys* 137, 439–460. https://doi.org/10.1007/BF00879044

Dupuy, C., Dostal, J., Dautria, J.M., Girod, M., 1986. Geochemistry of spinel peridotite inclusions in basalts from Hoggar, Algeria. *Journal of African Earth Sciences (1983)* 5, 209–215. https://doi.org/10.1016/0899-5362(86)90012-6

Ebnesajjad, S., 2014. Surface and Material Characterization Techniques, in: Surface Treatment of Materials for Adhesive Bonding. Elsevier, pp. 39–75. https://doi.org/10.1016/B978-0-323-26435-8.00004-6

Erskine, D.J., Nellis, W.J., 1991. Shock-induced martensitic phase transformation of oriented graphite to diamond. *Nature* 349, 317–319. https://doi.org/10.1038/349317a0

Evensen, N.M., Hamilton, P.J., O'Nions, R.K., 1978. Rare-earth abundances in chondritic meteorites. *Geochim Cosmochim Acta* 42, 1199–1212. https://doi.org/10.1016/0016-7037(78)90114-X

Farsang, S., Franchi, I.A., Zhao, X., Raub, T.D., Redfern, S.A.T., Grady, M.M., Zolensky, M., 2021. Carbonate assemblages in Cold Bokkeveld CM chondrite reveal complex parent body evolution. *Meteorit Planet Sci* 56, 723–741. https://doi.org/10.1111/maps.13647

Ferrari, A.C., 2007. Raman spectroscopy of graphene and graphite: Disorder, electron–phonon coupling, doping and nonadiabatic effects. *Solid State Commun* 143, 47–57. https://doi.org/10.1016/j.ssc.2007.03.052

Fossen, H., 2016. Structural Geology. Cambridge University Press. https://doi.org/10.1017/9781107415096

French, B.M., Koeberl, C., 2010. The convincing identification of terrestrial meteorite impact structures: What works, what doesn't, and why. *Earth Sci Rev* 98, 123–170. https://doi.org/10.1016/j.earscirev.2009.10.009

Friel, J.J., Lyman, C.E., 2006. Tutorial Review: X-ray Mapping in Electron-Beam Instruments. *Microscopy and Microanalysis* 12, 2–25. https://doi.org/10.1017/S1431927606060211

Fukunaga, K., Matsuda, J., Nagao, K., Miyamoto, M., Ito, K., 1987. Noble-gas enrichment in vapour-growth diamonds and the origin of diamonds in ureilites. *Nature* 328, 141–143. https://doi.org/10.1038/328141a0

Gaffey, M.J., Bell, J.F., Brown, R.H., Burbine, T.H., Piatek, J.L., Reed, K.L., Chaky, D.A., 1993. Mineralogical Variations within the S-Type Asteroid Class. *Icarus* 106, 573–602. https://doi.org/10.1006/icar.1993.1194

Gaul, O., 2000. Mapping olivine composition in the lithospheric mantle. *Earth Planet Sci Lett* 182, 223–235. https://doi.org/10.1016/S0012-821X(00)00243-0

GLAVIN, D.P., CALLAHAN, M.P., DWORKIN, J.P., ELSILA, J.E., 2010. The effects of parent body processes on amino acids in carbonaceous chondrites. *Meteorit Planet Sci* 45, 1948–1972. https://doi.org/10.1111/j.1945-5100.2010.01132.x

Goodhew, P.J., Humphreys, J., Beanland, R., 2000. Electron microscopy and analysis. CRC press.

Goodrich, C.A., 1992. Ureilites: A critical review. *Meteoritics* 27, 327–352. https://doi.org/10.1111/j.1945-5100.1992.tb00215.x

Goodrich, C.A., Fioretti, A.M., Tribaudino, M., Molin, G., 2001. Primary trapped melt inclusions in olivine in the olivine-augite-orthopyroxene ureilite Hughes 009. *Geochim Cosmochim Acta* 65, 621–652. https://doi.org/10.1016/S0016-7037(00)00521-4
Goodrich, C.A., Harlow, G.E., 2001. Knorringite-Uvarovite Garnet And Cr-Eskola Pyroxene In Ureilite LEW 88774, in: Meteoritics and Planetary Science Supplement. p. A68.
Goodrich, C.A., Hartmann, W.K., O'Brien, D.P., Weidenschilling, S.J., Wilson, L., Michel, P., Jutzi, M., 2015. Origin and history of ureilitic material in the solar system: The view from asteroid 2008 TC3 and the Almahata Sitta meteorite. *Meteorit Planet Sci* 50, 782–809. https://doi.org/10.1111/maps.12401
Goodrich, C.A., Jones, J.H., Berkley, J.L., 1987a. Origin and evolution of the ureilite parent magmas: Multi-stage igneous activity on a large parent body. *Geochim Cosmochim Acta* 51, 2255–2273. https://doi.org/10.1016/0016-7037(87)90279-1
Goodrich, C.A., Jones, J.H., Spitz, A.H., 1987b. Siderophile Element Tests of Ureilite Petrogenesis Models. *Meteoritics* 22, 392.
Goodrich, C.A., Lugmair, G.W., 1995. Stalking the LREE-enriched component in ureilites. *Geochim Cosmochim Acta* 59, 2609–2620. https://doi.org/10.1016/0016-7037(95)00153-0
Goodrich, C.A., Patchett, P.J., Lugmair, G.W., Drake, M.J., 1991. Sm-Nd and Rb-Sr isotopic systematics of ureilites. *Geochim Cosmochim Acta* 55, 829–848. https://doi.org/10.1016/0016-7037(91)90345-6
Goodrich, C.A., Scott, E.R.D., Fioretti, A.M., 2004. Ureilitic breccias: clues to the petrologic structure and impact disruption of the ureilite parent asteroid. *Geochemistry* 64, 283–327. https://doi.org/10.1016/j.chemer.2004.08.001
Goodrich, C.A., van Orman, J.A., Wilson, L., 2007. Fractional melting and smelting on the ureilite parent body. *Geochim Cosmochim Acta* 71, 2876–2895. https://doi.org/10.1016/j.gca.2007.03.023
Goresy, A. el, Gillet, P., Chen, M., Künstler, F., Graup, G., Stähle, V., 2001. In situ discovery of shock-induced graphite-diamond phase transition in gneisses from the Ries Crater, Germany. *American Mineralogist* 86, 611–621. https://doi.org/10.2138/am-2001-5-603
Grady, M.M., Wright, I.P., Swart, P.K., Pillinger, C.T., 1985. The carbon and nitrogen isotopic composition of ureilites: Implications for their genesis. *Geochim Cosmochim Acta* 49, 903–915. https://doi.org/10.1016/0016-7037(85)90306-0
Graham, A. ~L., 1978. Meteoritical Bulletin, No. 55. *Meteoritics* 13, 327–352.
Greenwood, R.C., Franchi, I.A., Gibson, J.M., Benedix, G.K., 2012a. Oxygen isotope variation in primitive achondrites: The influence of primordial, asteroidal and terrestrial processes. *Geochim Cosmochim Acta* 94, 146–163. https://doi.org/10.1016/j.gca.2012.06.025
Greenwood, R.C., Franchi, I.A., Gibson, J.M., Benedix, G.K., 2012b. Oxygen isotope variation in primitive achondrites: The influence of primordial, asteroidal and terrestrial processes. *Geochim Cosmochim Acta* 94, 146–163. https://doi.org/10.1016/j.gca.2012.06.025
Gribble, C.D., Hall, A.J., 1985. A Practical Introduction to Optical Mineralogy. Springer Netherlands, Dordrecht. https://doi.org/10.1007/978-94-011-7804-4
Griffin, S., Daly, L., Keller, T., Piazolo, S., Forman, L. v., Lee, M.R., Baumgartner, R.J., Trimby, P.W., Benedix, G.K., Irving, A.J., Hoefnagels, B., 2022a. Constraints on the Emplacement of Martian Nakhlite Igneous Rocks and Their Source Volcano From Advanced Micro-Petrofabric Analysis. *J Geophys Res Planets* 127. https://doi.org/10.1029/2021JE007080
Griffin, S., Daly, L., Piazolo, S., Forman, L. v., Cohen, B.E., Lee, M.R., Trimby, P.W., Baumgartner, R.J., Benedix, G.K., Hoefnagels, B., 2022b. Can the Magmatic Conditions

of the Martian Nakhlites be Discerned via Investigation of Clinopyroxene and Olivine Intracrystalline Misorientations? *J Geophys Res Planets* 127. https://doi.org/10.1029/2021JE007082
Grund, T., Bischoff, A., 1999. Cathodoluminescence properties of diamonds in ureilites: Further evidence for a shock-induced origin. *Meteoritics and Planetary Science Supplement* 34, A48.
Gunter, M.E., 2004. The Polarized Light Microscope: Should We Teach the use of a 19th Century Instrument in the 21st Century? *Journal of Geoscience Education* 52, 34–44. https://doi.org/10.5408/1089-9995-52.1.34
Halfpenny, A., 2010. Some important practical issues for the collection and manipulation of Electron Backscatter Diffraction (EBSD) data from geological samples. *Journal of the Virtual Explorer* 35. https://doi.org/10.3809/jvirtex.2011.00272
Hanna, R.D., Ketcham, R.A., Zolensky, M., Behr, W.M., 2015. Impact-induced brittle deformation, porosity loss, and aqueous alteration in the Murchison CM chondrite. *Geochim Cosmochim Acta* 171, 256–282. https://doi.org/10.1016/j.gca.2015.09.005
Hellmann, J.L., Hopp, T., Burkhardt, C., Kleine, T., 2020. Origin of volatile element depletion among carbonaceous chondrites. *Earth Planet Sci Lett* 549, 116508. https://doi.org/10.1016/j.epsl.2020.116508
Hiroi, T., Pieters, C.M., Zolensky, M.E., Lipschutz, M.E., 1993. Evidence of Thermal Metamorphism on the C, G, B, and F Asteroids. *Science (1979)* 261, 1016–1018. https://doi.org/10.1126/science.261.5124.1016
Hiroshi Takeda, 1989. Mineralogy of coexisting pyroxenes in magnesian ureilites and their formation conditions. *Earth Planet Sci Lett* 93, 181–194. https://doi.org/10.1016/0012-821X(89)90067-8
Hirschmann, M.M., 2021. Iron-wüstite revisited: A revised calibration accounting for variable stoichiometry and the effects of pressure. *Geochim Cosmochim Acta* 313, 74–84. https://doi.org/10.1016/j.gca.2021.08.039
Hough, R.M., Gilmour, I., Pillinger, C.T., Arden, J.W., Gilkess, K.W.R., Yuan, J., Milledge, H.J., 1995. Diamond and silicon carbide in impact melt rock from the Ries impact crater. *Nature* 378, 41–44. https://doi.org/10.1038/378041a0
Hunter, R.H., 1996. Texture Development in Cumulate Rocks. pp. 77–101. https://doi.org/10.1016/S0167-2894(96)80005-4
Isobe, F., Ohfuji, H., Sumiya, H., Irifune, T., 2013. Nanolayered Diamond Sintered Compact Obtained by Direct Conversion from Highly Oriented Graphite under High Pressure and High Temperature. *J Nanomater* 2013, 1–6. https://doi.org/10.1155/2013/380165
Jenniskens, P., Shaddad, M.H., Numan, D., Elsir, S., Kudoda, A.M., Zolensky, M.E., Le, L., Robinson, G.A., Friedrich, J.M., Rumble, D., Steele, A., Chesley, S.R., Fitzsimmons, A., Duddy, S., Hsieh, H.H., Ramsay, G., Brown, P.G., Edwards, W.N., Tagliaferri, E., Boslough, M.B., Spalding, R.E., Dantowitz, R., Kozubal, M., Pravec, P., Borovicka, J., Charvat, Z., Vaubaillon, J., Kuiper, J., Albers, J., Bishop, J.L., Mancinelli, R.L., Sandford, S.A., Milam, S.N., Nuevo, M., Worden, S.P., 2009. The impact and recovery of asteroid 2008 TC3. *Nature* 458, 485–488. https://doi.org/10.1038/nature07920
Jenniskens, P., Vaubaillon, J., Binzel, R.P., DeMeo, F.E., Nesvorný, D., Bottke, W.F., Fitzsimmons, A., Hiroi, T., Marchis, F., Bishop, J.L., Vernazza, P., Zolensky, M.E., Herrin, J.S., Welten, K.C., Meier, M.M.M., Shaddad, M.H., 2010. Almahata Sitta (=asteroid 2008 TC3) and the search for the ureilite parent body. *Meteorit Planet Sci* 45, 1590–1617. https://doi.org/10.1111/j.1945-5100.2010.01153.x
Jerofeev, M. v., Lachinov, P.A., 1888. Description of Novo Urei meteorite. Petersburg.
Jochum, K.P., Seufert, H.M., Spettel, B., Palme, H., 1986. The solar-system abundances of Nb, Ta, and Y, and the relative abundances of refractory lithophile elements in

differentiated planetary bodies. *Geochim Cosmochim Acta* 50, 1173–1183. https://doi.org/10.1016/0016-7037(86)90400-X
Kaminsky, F. v., Khachatryan, G.K., 2004. The relationship between the distribution of nitrogen impurity centres in diamond crystals and their internal structure and mechanism of growth. *Lithos* 77, 255–271. https://doi.org/10.1016/j.lithos.2004.04.035
Karato, S., 1989. Grain growth kinetics in olivine aggregates. *Tectonophysics* 168, 255–273. https://doi.org/10.1016/0040-1951(89)90221-7
Karato, S., Jung, H., Katayama, I., Skemer, P., 2008. Geodynamic Significance of Seismic Anisotropy of the Upper Mantle: New Insights from Laboratory Studies. *Annu Rev Earth Planet Sci* 36, 59–95. https://doi.org/10.1146/annurev.earth.36.031207.124120
Katsura, T., Ito, E., 1989. The system Mg2SiO4 -Fe2SiO4 at high pressures and temperatures: Precise determination of stabilities of olivine, modified spinel, and spinel. *J Geophys Res Solid Earth* 94, 15663–15670. https://doi.org/10.1029/JB094iB11p15663
Keil, K., 2010. Enstatite achondrite meteorites (aubrites) and the histories of their asteroidal parent bodies. *Geochemistry* 70, 295–317. https://doi.org/10.1016/j.chemer.2010.02.002
Keil, K., Bischoff, A., 2008. Northwest Africa 2526: A partial melt residue of enstatite chondrite parentage. *Meteorit Planet Sci* 43, 1233–1240. https://doi.org/10.1111/j.1945-5100.2008.tb01125.x
Kenkmann, T., Hornemann, U., Stöffler, D., 2005. Experimental shock synthesis of diamonds in a graphite gneiss. *Meteorit Planet Sci* 40, 1299–1310. https://doi.org/10.1111/j.1945-5100.2005.tb00402.x
Korsakov, A. v., Zhimulev, E.I., Mikhailenko, D.S., Demin, S.P., Kozmenko, O.A., 2015. Graphite pseudomorphs after diamonds: An experimental study of graphite morphology and the role of H2O in the graphitisation process. *Lithos* 236–237, 16–26. https://doi.org/10.1016/j.lithos.2015.08.012
Krot, A.N., 2019. Refractory inclusions in carbonaceous chondrites: Records of early solar system processes. *Meteorit Planet Sci* 54, 1647–1691. https://doi.org/10.1111/maps.13350
Kruijer, T.S., Touboul, M., Fischer-Gödde, M., Bermingham, K.R., Walker, R.J., Kleine, T., 2014. Protracted core formation and rapid accretion of protoplanets. *Science (1979)* 344, 1150–1154. https://doi.org/10.1126/science.1251766
Kurat, G., 1988. Primitive meteorites: an attempt towards unification. *Philosophical Transactions of the Royal Society of London. Series A, Mathematical and Physical Sciences* 325, 459–482. https://doi.org/10.1098/rsta.1988.0061
Langenhorst, F., Poirier, J.-P., Deutsch, A., Hornemann, U., 2002. Experimental approach to generate shock veins in single crystal olivine by shear melting. *Meteorit Planet Sci* 37, 1541–1553. https://doi.org/10.1111/j.1945-5100.2002.tb00809.x
Langenhorst, F., Shafranovsky, G., Masaitis, V.L., 1998. A comparative study of impact diamonds from the Popigai, Ries, Sudbury, and Lappajarvi craters. *Meteoritics and Planetary Science Supplement* 33, A90.
Larkin, P., 2011. Introduction, in: Infrared and Raman Spectroscopy. Elsevier, pp. 1–5. https://doi.org/10.1016/B978-0-12-386984-5.10001-1
Lauretta, D.S., Balram-Knutson, S.S., Beshore, E., Boynton, W. v., Drouet d'Aubigny, C., DellaGiustina, D.N., Enos, H.L., Golish, D.R., Hergenrother, C.W., Howell, E.S., Bennett, C.A., Morton, E.T., Nolan, M.C., Rizk, B., Roper, H.L., Bartels, A.E., Bos, B.J., Dworkin, J.P., Highsmith, D.E., Lorenz, D.A., Lim, L.F., Mink, R., Moreau, M.C., Nuth, J.A., Reuter, D.C., Simon, A.A., Bierhaus, E.B., Bryan, B.H., Ballouz, R., Barnouin, O.S., Binzel, R.P., Bottke, W.F., Hamilton, V.E., Walsh, K.J., Chesley, S.R., Christensen, P.R., Clark, B.E., Connolly, H.C., Crombie, M.K., Daly, M.G., Emery, J.P., McCoy, T.J., McMahon, J.W., Scheeres, D.J., Messenger, S., Nakamura-Messenger, K.,

Righter, K., Sandford, S.A., 2017. OSIRIS-REx: Sample Return from Asteroid (101955) Bennu. *Space Sci Rev* 212, 925–984. https://doi.org/10.1007/s11214-017-0405-1
Leroux, H., Devouard, B., Cordier, P., Guyot, F., 2004. Pyroxene microstructure in the Northwest Africa 856 martian meteorite. *Meteorit Planet Sci* 39, 711–722. https://doi.org/10.1111/j.1945-5100.2004.tb00114.x
Li, Y., McCausland, P.J.A., Flemming, R.L., Yamaguchi, A., 2021. Quantitative shock measurement of olivine in ureilite meteorites. *Meteorit Planet Sci* 56, 1422–1439. https://doi.org/10.1111/maps.13706
Lipschutz, M.E., 1964. Origin of Diamonds in the Ureilites. *Science (1979)* 143, 1431–1434. https://doi.org/10.1126/science.143.3613.1431.b
Lipschutz, M.E., Schultz, L., 2014. Meteorites, in: Encyclopedia of the Solar System. Elsevier, pp. 625–655. https://doi.org/10.1016/B978-0-12-415845-0.00028-1
Lisse, C.M., Wyatt, M.C., Chen, C.H., Morlok, A., Watson, D.M., Manoj, P., Sheehan, P., Currie, T.M., Thebault, P., Sitko, M.L., 2012. SPITZER EVIDENCE FOR A LATE-HEAVY BOMBARDMENT AND THE FORMATION OF UREILITES IN η CORVI At ∼1 Gyr. *Astrophys J* 747, 93. https://doi.org/10.1088/0004-637X/747/2/93
Litasov, K., Teplyakova, S., Shatskiy, A., Kuper, K., 2019. Fe-Ni-P-S Melt Pockets in Elga IIE Iron Meteorite: Evidence for the Origin at High-Pressures Up to 20 GPa. *Minerals* 9, 616. https://doi.org/10.3390/min9100616
Lodders, K., 2003. Solar System Abundances and Condensation Temperatures of the Elements. *Astrophys J* 591, 1220–1247. https://doi.org/10.1086/375492
MacPherson, G.J., Kita, N.T., Ushikubo, T., Bullock, E.S., Davis, A.M., 2012. Well-resolved variations in the formation ages for Ca–Al-rich inclusions in the early Solar System. *Earth Planet Sci Lett* 331–332, 43–54. https://doi.org/10.1016/j.epsl.2012.03.010
Mainprice, D., Tommasi, A., Couvy, H., Cordier, P., Frost, D.J., 2005. Pressure sensitivity of olivine slip systems and seismic anisotropy of Earth's upper mantle. *Nature* 433, 731–733. https://doi.org/10.1038/nature03266
Masaitis, V.L., 1998. Popigai crater: Origin and distribution of diamond-bearing impactites. *Meteorit Planet Sci* 33, 349–359. https://doi.org/10.1111/j.1945-5100.1998.tb01639.x
Mason, B., 1963. The carbonaceous chondrites. *Space Sci Rev* 1, 621–646. https://doi.org/10.1007/BF00212446
McKenzie, D., Jackson, J., Priestley, K., 2005. Thermal structure of oceanic and continental lithosphere. *Earth Planet Sci Lett* 233, 337–349. https://doi.org/10.1016/j.epsl.2005.02.005
McSween, H.Y., Binzel, R.P., de Sanctis, M.C., Ammannito, E., Prettyman, T.H., Beck, A.W., Reddy, V., le Corre, L., Gaffey, M.J., McCord, T.B., Raymond, C.A., Russell, C.T., 2013. Dawn; the Vesta-HED connection; and the geologic context for eucrites, diogenites, and howardites. *Meteorit Planet Sci* 48, 2090–2104. https://doi.org/10.1111/maps.12108
Michikami, T., Honda, C., Miyamoto, H., Hirabayashi, M., Hagermann, A., Irie, T., Nomura, K., Ernst, C.M., Kawamura, M., Sugimoto, K., Tatsumi, E., Morota, T., Hirata, Naru, Noguchi, T., Cho, Y., Kameda, S., Kouyama, T., Yokota, Y., Noguchi, R., Hayakawa, M., Hirata, Naoyuki, Honda, R., Matsuoka, M., Sakatani, N., Suzuki, H., Yamada, M., Yoshioka, K., Sawada, H., Hemmi, R., Kikuchi, H., Ogawa, K., Watanabe, S., Tanaka, S., Yoshikawa, M., Tsuda, Y., Sugita, S., 2019. Boulder size and shape distributions on asteroid Ryugu. *Icarus* 331, 179–191. https://doi.org/10.1016/j.icarus.2019.05.019
Mikouchi, T., Zolensky, M.E., Ohnishi, I., Suzuki, T., Takeda, H., Jenniskens, P., Shaddad, M.H., 2010. Electron microscopy of pyroxene in the Almahata Sitta ureilite. *Meteorit Planet Sci* 45, 1812–1820. https://doi.org/10.1111/j.1945-5100.2010.01111.x

Miyahara, M., Ohtani, E., El Goresy, A., Lin, Y., Feng, L., Zhang, J.-C., Gillet, P., Nagase, T., Muto, J., Nishijima, M., 2015. Unique large diamonds in a ureilite from Almahata Sitta 2008 TC3 asteroid. *Geochim Cosmochim Acta* 163, 14–26. https://doi.org/10.1016/j.gca.2015.04.035

Miyamoto, M., Takase, T., Mitsuda, Y., 1993. Raman spectra of various diamonds. *Mineralogical Journal* 16, 246–257. https://doi.org/10.2465/minerj.16.246

Miyamoto, M., Takeda, H., Toyoda, H., 1985. Cooling history of some Antarctic ureilites. *J Geophys Res* 90, 116. https://doi.org/10.1029/JB090iS01p00116

Morimoto, N., 1988. Nomenclature of Pyroxenes. *Mineral Petrol* 39, 55–76. https://doi.org/10.1007/BF01226262

Mueller, G., 1969. Genetical Interrelations Between Ureilites and Carbonaceous Chondrites. pp. 505–517. https://doi.org/10.1007/978-94-010-3411-1_42

Mueller, G., 1966. Significance of Inclusions in Carbonaceous Meteorites. *Nature* 210, 151–155. https://doi.org/10.1038/210151a0

Müller, W.F., 1993. Thermal and deformation history of the Shergotty meteorite deduced from clinopyroxene microstructure. *Geochim Cosmochim Acta* 57, 4311–4322. https://doi.org/10.1016/0016-7037(93)90325-Q

Nabiei, F., Badro, J., Dennenwaldt, T., Oveisi, E., Cantoni, M., Hébert, C., El Goresy, A., Barrat, J.-A., Gillet, P., 2018. A large planetary body inferred from diamond inclusions in a ureilite meteorite. *Nat Commun* 9, 1327. https://doi.org/10.1038/s41467-018-03808-6

Németh, P., Garvie, L.A.J., Aoki, T., Dubrovinskaia, N., Dubrovinsky, L., Buseck, P.R., 2014. Lonsdaleite is faulted and twinned cubic diamond and does not exist as a discrete material. *Nat Commun* 5, 5447. https://doi.org/10.1038/ncomms6447

Nestola, F., Goodrich, C.A., Morana, M., Barbaro, A., Jakubek, R.S., Christ, O., Brenker, F.E., Domeneghetti, M.C., Dalconi, M.C., Alvaro, M., Fioretti, A.M., Litasov, K.D., Fries, M.D., Leoni, M., Casati, N.P.M., Jenniskens, P., Shaddad, M.H., 2020. Impact shock origin of diamonds in ureilite meteorites. *Proceedings of the National Academy of Sciences* 117, 25310–25318. https://doi.org/10.1073/pnas.1919067117

Nesvorný, D., Vokrouhlický, D., Morbidelli, A., Bottke, W.F., 2009. Asteroidal source of L chondrite meteorites. *Icarus* 200, 698–701. https://doi.org/10.1016/j.icarus.2008.12.016

Nolze, G., Geist, V., Neumann, R.S., Buchheim, M., 2005. Investigation of orientation relationships by EBSD and EDS on the example of the Watson iron meteorite. *Crystal Research and Technology* 40, 791–804. https://doi.org/10.1002/crat.200410434

Ogata, H., Takeda, H., 1991. Mineralogy of interstitial rim materials of the Y74123 and Y790981 ureilites and their origin. *Meteoritics* 26, 195–201. https://doi.org/10.1111/j.1945-5100.1991.tb01039.x

Okazaki, R., Sawada, H., Yamanouchi, S., Tachibana, S., Miura, Y.N., Sakamoto, K., Takano, Y., Abe, M., Itoh, S., Yamada, K., Yabuta, H., Okamoto, C., Yano, H., Noguchi, T., Nakamura, T., Nagao, K., 2017. Hayabusa2 Sample Catcher and Container: Metal-Seal System for Vacuum Encapsulation of Returned Samples with Volatiles and Organic Compounds Recovered from C-Type Asteroid Ryugu. *Space Sci Rev* 208, 107–124. https://doi.org/10.1007/s11214-016-0289-5

Oliver, N.H.S., Bons, P.D., 2001. Mechanisms of fluid flow and fluid-rock interaction in fossil metamorphic hydrothermal systems inferred from vein-wallrock patterns, geometry and microstructure. *Geofluids* 1, 137–162. https://doi.org/10.1046/j.1468-8123.2001.00013.x

Ott, U., 2014. Planetary and pre-solar noble gases in meteorites. *Geochemistry* 74, 519–544. https://doi.org/10.1016/j.chemer.2014.01.003

Peterson, L.D., Newcombe, M.E., M. O'D. Alexander, C., Wang, J., Sarafian, A.R., Bischoff, A., Nielsen, S.G., 2022. The H2O content of the ureilite parent body. *Geochim Cosmochim Acta*. https://doi.org/10.1016/j.gca.2022.10.036
Pitcher, W.S., 1997. The evidence for restite: unmixing as an alternative hypothesis, in: The Nature and Origin of Granite. Springer Netherlands, Dordrecht, pp. 125–143. https://doi.org/10.1007/978-94-011-5832-9_8
Potin, S., Beck, P., Usui, F., Bonal, L., Vernazza, P., Schmitt, B., 2020. Style and intensity of hydration among C-complex asteroids: A comparison to desiccated carbonaceous chondrites. *Icarus* 348, 113826. https://doi.org/10.1016/j.icarus.2020.113826
Prieto, G.A., Froment, B., Yu, C., Poli, P., Abercrombie, R., 2017. Earthquake rupture below the brittle-ductile transition in continental lithospheric mantle. *Sci Adv* 3. https://doi.org/10.1126/sciadv.1602642
Prior, D.J., Mariani, E., Wheeler, J., 2009. EBSD in the Earth Sciences: Applications, Common Practice, and Challenges, in: Electron Backscatter Diffraction in Materials Science. Springer US, Boston, MA, pp. 345–360. https://doi.org/10.1007/978-0-387-88136-2_26
Ragan, D.M., 1969. Olivine recrystallization textures. *Mineral Mag* 37, 238–240. https://doi.org/10.1180/minmag.1969.037.286.11
Rai, N., Downes, H., Smith, C., 2020. Ureilite meteorites provide a new model of early planetesimal formation and destruction. *Geochem Perspect Lett* 20–25. https://doi.org/10.7185/geochemlet.2018
Ramsay, J.G., 1980. The crack–seal mechanism of rock deformation. *Nature* 284, 135–139. https://doi.org/10.1038/284135a0
Ramsey, J.M., Chester, F.M., 2004. Hybrid fracture and the transition from extension fracture to shear fracture. *Nature* 428, 63–66. https://doi.org/10.1038/nature02333
Rauf, K.M., Hossieni, H., Arkan, Z., Sarkawt, D., 2015. Distribution of Moons in the Solar System. *Journal of Astrophysics & Aerospace Technology* 03. https://doi.org/10.4172/2329-6542.1000120
Reed, S.J.B., 2005. Electron_Microprobe_Analysis_and_Scannin.
Rinaldi, R., Llovet, X., 2015. Electron Probe Microanalysis: A Review of the Past, Present, and Future. *Microscopy and Microanalysis* 21, 1053–1069. https://doi.org/10.1017/S1431927615000409
Ringwood, A. ~E., Essene, E., 1970. Petrogenesis of Apollo 11 basalts, internal constitution and origin of the moon. *Geochimica et Cosmochimica Acta Supplement* 1, 769.
Ross, A.J., Steele, A., Fries, M.D., Kater, L., Downes, H., Jones, A.P., Smith, C.L., Jenniskens, P.M., Zolensky, M.E., Shaddad, M.H., 2011. MicroRaman spectroscopy of diamond and graphite in Almahata Sitta and comparison with other ureilites. *Meteorit Planet Sci* 46, 364–378. https://doi.org/10.1111/j.1945-5100.2010.01157.x
Rubin, A.E., 2006. Shock, post-shock annealing, and post-annealing shock in ureilites. *Meteorit Planet Sci* 41, 125–133. https://doi.org/10.1111/j.1945-5100.2006.tb00197.x
Rubin, A.E., 2004. Postshock annealing and postannealing shock in equilibrated ordinary chondrites: implications for the thermal and shock histories of chondritic asteroids. *Geochim Cosmochim Acta* 68, 673–689. https://doi.org/10.1016/S0016-7037(03)00452-6
Rubin, A.E., 1997. Mineralogy of meteorite groups. *Meteorit Planet Sci* 32, 231–247. https://doi.org/10.1111/j.1945-5100.1997.tb01262.x
Rubin, A.E., 1992. A shock-metamorphic model for silicate darkening and compositionally variable plagioclase in CK and ordinary chondrites. *Geochim Cosmochim Acta* 56, 1705–1714. https://doi.org/10.1016/0016-7037(92)90236-C

Rubin, A.E., 1988. Formation of Ureilites by Impact-Melting of Carbonaceous Chondritic Material. *Meteoritics* 23, 333–337. https://doi.org/10.1111/j.1945-5100.1988.tb00918.x
Rubin, A.E., Grossman, J.N., 2010. Meteorite and meteoroid: new comprehensive definitions. *Meteorit Planet Sci*. https://doi.org/10.1111/j.1945-5100.2009.01009.x
Ruzicka, A., Snyder, G.A., Taylor, L.A., 1997. Vesta as the howardite, eucrite and diogenite parent body: Implications for the size of a core and for large-scale differentiation. *Meteorit Planet Sci* 32, 825–840. https://doi.org/10.1111/j.1945-5100.1997.tb01573.x
Ruzicka, A.M., Hugo, R.C., 2018. Electron backscatter diffraction (EBSD) study of seven heavily metamorphosed chondrites: Deformation systematics and variations in pre-shock temperature and post-shock annealing. *Geochim Cosmochim Acta* 234, 115–147. https://doi.org/10.1016/j.gca.2018.05.014
Salman Ali, A., 2020. Application of Nanomaterials in Environmental Improvement, in: Nanotechnology and the Environment. IntechOpen. https://doi.org/10.5772/intechopen.91438
Sanders, I.S., Scott, E.R.D., Delaney, J.S., 2017. Origin of mass-independent oxygen isotope variation among ureilites: Clues from chondrites and primitive achondrites. *Meteorit Planet Sci* 52, 690–708. https://doi.org/10.1111/maps.12820
Schiller, M., Paton, C., Bizzarro, M., 2015. Evidence for nucleosynthetic enrichment of the protosolar molecular cloud core by multiple supernova events. *Geochim Cosmochim Acta* 149, 88–102. https://doi.org/10.1016/j.gca.2014.11.005
Schrader, D.L., McCoy, T.J., Gardner-Vandy, K., 2017. Relict chondrules in primitive achondrites: Remnants from their precursor parent bodies. *Geochim Cosmochim Acta* 205, 295–312. https://doi.org/10.1016/j.gca.2017.02.012
Scott, E.R.D., Krot, A.N., 2007. Chondrites and Their Components, in: Treatise on Geochemistry. Elsevier, pp. 1–72. https://doi.org/10.1016/B0-08-043751-6/01145-2
Scott, E.R.D., Taylor, G.J., Keil, K., 1993. Origin of ureilite meteorites and implications for planetary accretion. *Geophys Res Lett* 20, 415–418. https://doi.org/10.1029/93GL00474
Scott, E.R.D., Wasson, J.T., 1975. Classification and properties of iron meteorites. *Reviews of Geophysics* 13, 527. https://doi.org/10.1029/RG013i004p00527
Seiler, H., 1983. Secondary electron emission in the scanning electron microscope. *J Appl Phys* 54, R1–R18. https://doi.org/10.1063/1.332840
Sikirdji, M., Warren, P.H., 2001. NORTHWEST AFRICA 766: A NEW FERROAN UREILITE WITH Cr-SPINEL, Cr-RICH GARNET (?) AND ASSOCIATED Si, Al-Rich Glasses, in: Meteoritics and Planetary Science Supplement. p. A189.
Singletary, S., Grove, T.L., 2006. Experimental constraints on ureilite petrogenesis. *Geochim Cosmochim Acta* 70, 1291–1308. https://doi.org/10.1016/j.gca.2005.10.034
Singletary, S.J., Grove, T.L., 2003. Early petrologic processes on the ureilite parent body. *Meteorit Planet Sci* 38, 95–108. https://doi.org/10.1111/j.1945-5100.2003.tb01048.x
Sobolev, N. v., Shatsky, V.S., 1990. Diamond inclusions in garnets from metamorphic rocks: a new environment for diamond formation. *Nature* 343, 742–746. https://doi.org/10.1038/343742a0
Spitz, A.H., Boynton, W. v, 1991. Trace element analysis of ureilites: New constraints on their petrogenesis. *Geochim Cosmochim Acta* 55, 3417–3430. https://doi.org/10.1016/0016-7037(91)90500-5
Stachel, T., Harris, J.W., 2009. Formation of diamond in the Earth's mantle. *Journal of Physics: Condensed Matter* 21, 364206. https://doi.org/10.1088/0953-8984/21/36/364206
Stöffler, D., Hamann, C., Metzler, K., 2018. Shock metamorphism of planetary silicate rocks and sediments: Proposal for an updated classification system. *Meteorit Planet Sci* 53, 5–49. https://doi.org/10.1111/maps.12912

Stöffler, D., Keil, K., Edward R.D, S., 1991. Shock metamorphism of ordinary chondrites. *Geochim Cosmochim Acta* 55, 3845–3867. https://doi.org/10.1016/0016-7037(91)90078-J

Stosch, H.-G., Seck, H.A., 1980. Geochemistry and mineralogy of two spinel peridotite suites from Dreiser Weiher, West Germany. *Geochim Cosmochim Acta* 44, 457–470. https://doi.org/10.1016/0016-7037(80)90044-7

Suzuki, A., Ohtani, E., Morishima, H., Kubo, T., Kanbe, Y., Kondo, T., Okada, T., Terasaki, H., Kato, T., Kikegawa, T., 2000. In situ determination of the phase boundary between Wadsleyite and Ringwoodite in Mg2SiO4. *Geophys Res Lett* 27, 803–806. https://doi.org/10.1029/1999GL008425

Takahashi, K., Masuda, A., 1990. The Rb-Sr and Sm-Nd dating and REE measurements of ureilites. *Meteoritics* 25, 413.

Takeda, H., 1987. Mineralogy of Antarctic ureilites and a working hypothesis for their origin and evolution. *Earth Planet Sci Lett* 81, 358–370. https://doi.org/10.1016/0012-821X(87)90123-3

Takeda, H., Mori, H., Ogata, H., 1988. On the pairing of Antarctic ureilites with reference to their parent body. *Antarctic Meteorite Research* 1, 145.

Tarduno, J.A., Cottrell, R.D., Nimmo, F., Hopkins, J., Voronov, J., Erickson, A., Blackman, E., Scott, E.R.D., McKinley, R., 2012. Evidence for a Dynamo in the Main Group Pallasite Parent Body. *Science (1979)* 338, 939–942. https://doi.org/10.1126/science.1223932

Tasaka, M., Michibayashi, K., Mainprice, D., 2008. B-type olivine fabrics developed in the fore-arc side of the mantle wedge along a subducting slab. *Earth Planet Sci Lett* 272, 747–757. https://doi.org/10.1016/j.epsl.2008.06.014

Taylor, G.J., 1992. Core formation in asteroids. *J Geophys Res* 97, 14717. https://doi.org/10.1029/92JE01501

Timms, N.E., Erickson, T.M., Pearce, M.A., Cavosie, A.J., Schmieder, M., Tohver, E., Reddy, S.M., Zanetti, M.R., Nemchin, A.A., Wittmann, A., 2017. A pressure-temperature phase diagram for zircon at extreme conditions. *Earth Sci Rev* 165, 185–202. https://doi.org/10.1016/j.earscirev.2016.12.008

Torigoye-Kita, N., Misawa, K., Tatsumoto, M., 1995. U□Th□Pb and Sm□Nd isotopic systematics of the Goalpara ureilite: Resolution of terrestrial contamination. *Geochim Cosmochim Acta* 59, 381–390. https://doi.org/10.1016/0016-7037(95)00279-9

Treiman, A.H., Berkley, J.L., 1994. Igneous petrology of the new ureilites Nova 001 and Nullarbor 010. *Meteoritics* 29, 843–848. https://doi.org/10.1111/j.1945-5100.1994.tb01097.x

Tsuchiyama, A., Uesugi, M., Matsushima, T., Michikami, T., Kadono, T., Nakamura, T., Uesugi, K., Nakano, T., Sandford, S.A., Noguchi, R., Matsumoto, T., Matsuno, J., Nagano, T., Imai, Y., Takeuchi, A., Suzuki, Y., Ogami, T., Katagiri, J., Ebihara, M., Ireland, T.R., Kitajima, F., Nagao, K., Naraoka, H., Noguchi, T., Okazaki, R., Yurimoto, H., Zolensky, M.E., Mukai, T., Abe, M., Yada, T., Fujimura, A., Yoshikawa, M., Kawaguchi, J., 2011. Three-Dimensional Structure of Hayabusa Samples: Origin and Evolution of Itokawa Regolith. *Science (1979)* 333, 1125–1128. https://doi.org/10.1126/science.1207807

van Kooten, E.M.M.E., Schiller, M., Bizzarro, M., 2017. Magnesium and chromium isotope evidence for initial melting by radioactive decay of 26Al and late stage impact-melting of the ureilite parent body. *Geochim Cosmochim Acta* 208, 1–23. https://doi.org/10.1016/j.gca.2017.03.033

van Schmus, W.R., Wood, J.A., 1967. A chemical-petrologic classification for the chondritic meteorites. *Geochim Cosmochim Acta* 31, 747–765. https://doi.org/10.1016/S0016-7037(67)80030-9
Vdovykin, G.P., 1970. Ureilites. *Space Sci Rev* 10. https://doi.org/10.1007/BF00172536
Wager, L.R., Brown, G.M., Wadsworth, W.J., 1960. Types of Igneous Cumulates. *Journal of Petrology* 1, 73–85. https://doi.org/10.1093/petrology/1.1.73
Walker, D., Agee, C.B., 1988. Ureilite Compaction. *Meteoritics* 23, 81–91. https://doi.org/10.1111/j.1945-5100.1988.tb00899.x
Wallis, D., Hansen, L.N., Britton, T.B., Wilkinson, A.J., 2019. High-Angular Resolution Electron Backscatter Diffraction as a New Tool for Mapping Lattice Distortion in Geological Minerals. *J Geophys Res Solid Earth* 124, 6337–6358. https://doi.org/10.1029/2019JB017867
Walters, A.S., Goodenough, K.M., Hughes, H.S.R., Roberts, N.M.W., Gunn, A.G., Rushton, J., Lacinska, A., 2013. Enrichment of Rare Earth Elements during magmatic and post-magmatic processes: a case study from the Loch Loyal Syenite Complex, northern Scotland. *Contributions to Mineralogy and Petrology* 166, 1177–1202. https://doi.org/10.1007/s00410-013-0916-z
Wang, Y., Lesher, C.M., Lightfoot, P.C., Pattison, E.F., Golightly, J.P., 2018. Shock metamorphic features in mafic and ultramafic inclusions in the Sudbury Igneous Complex: Implications for their origin and impact excavation. *Geology* 46, 443–446. https://doi.org/10.1130/G39913.1
Wänke, H., Baddenhausen, H., Spettel, B., Teschke, F., Quijano-Rico, M., Dreibus, G., Palme, H., 1972. THE CHEMISTRY OF HAVERÖ UREILITE. *Meteoritics* 7, 579–590. https://doi.org/10.1111/j.1945-5100.1972.tb00140.x
Warren, J.M., Hirth, G., Kelemen, P.B., 2008. Evolution of olivine lattice preferred orientation during simple shear in the mantle. *Earth Planet Sci Lett* 272, 501–512. https://doi.org/10.1016/j.epsl.2008.03.063
Warren, P.H., 2012. Parent body depth-pressure-temperature relationships and the style of the ureilite anatexis. *Meteorit Planet Sci* 47, 209–227. https://doi.org/10.1111/j.1945-5100.2011.01320.x
Warren, P.H., Kallemeyn, G.W., 1992. Explosive volcanism and the graphite-oxygen fugacity buffer on the parent asteroid(s) of the ureilite meteorites. *Icarus* 100, 110–126. https://doi.org/10.1016/0019-1035(92)90022-Y
Warren, P.H., Kallemeyn, G.W., 1989. Geochemistry of polymict ureilite EET83309, and a partially-disruptive impact model for ureilite origin. *Meteoritics* 24, 233–246. https://doi.org/10.1111/j.1945-5100.1989.tb00698.x
Warren, P.H., Rubin, A.E., 2010. Pyroxene-selective impact smelting in ureilites. *Geochim Cosmochim Acta* 74, 5109–5133. https://doi.org/10.1016/j.gca.2010.05.026
Warren, P.H., Ulff-Møller, F., Huber, H., Kallemeyn, G.W., 2006. Siderophile geochemistry of ureilites: A record of early stages of planetesimal core formation. *Geochim Cosmochim Acta* 70, 2104–2126. https://doi.org/10.1016/j.gca.2005.12.026
Wasson, J.T., Chou, C.-L., Bild, R.W., Baedecker, P.A., 1976. Classification of and elemental fractionation among ureilites. *Geochim Cosmochim Acta* 40, 1449–1458. https://doi.org/10.1016/0016-7037(76)90081-8
Weisberg, M.K., McCoy, T.J., Krot, A.N., 2006. Systematics and evaluation of meteorite classification. , 19, pp.19-52., in: Meteorites and the Early Solar System II. pp. 19–52.
Weiss, B.P., Elkins-Tanton, L.T., 2013. Differentiated Planetesimals and the Parent Bodies of Chondrites. *Annu Rev Earth Planet Sci* 41, 529–560. https://doi.org/10.1146/annurev-earth-040610-133520

Weiss, Y., Griffin, W., Elhlou, S., Navon, O., 2008. Comparison between LA-ICP-MS and EPMA analysis of trace elements in diamonds. *Chem Geol* 252, 158–168. https://doi.org/10.1016/j.chemgeo.2008.02.008

White, L.F., Darling, J.R., Moser, D.E., Cayron, C., Barker, I., Dunlop, J., Tait, K.T., 2018. Baddeleyite as a widespread and sensitive indicator of meteorite bombardment in planetary crusts. *Geology* 46, 719–722. https://doi.org/10.1130/G45008.1

Whitney, D.L., Evans, B.W., 2010. Abbreviations for names of rock-forming minerals. *American Mineralogist* 95, 185–187. https://doi.org/10.2138/am.2010.3371

Wilkinson, A.J., Britton, T.Ben., 2012. Strains, planes, and EBSD in materials science. *Materials Today* 15, 366–376. https://doi.org/10.1016/S1369-7021(12)70163-3

Winkelmann, A., Cios, G., Tokarski, T., Nolze, G., Hielscher, R., Kozieł, T., 2020. EBSD orientation analysis based on experimental Kikuchi reference patterns. *Acta Mater* 188, 376–385. https://doi.org/10.1016/j.actamat.2020.01.053

Wirth, R., 1996. Thin amorphous films (1-2 nm) at olivine grain boundaries in mantle xenoliths from San Carlos, Arizona. *Contributions to Mineralogy and Petrology* 124, 44–54. https://doi.org/10.1007/s004100050172

Wlotzka, F., 1972. HAVERÖ UREILITE: EVIDENCE FOR RECRYSTALLIZATION AND PARTIAL REDUCTION. *Meteoritics* 7, 591–600. https://doi.org/10.1111/j.1945-5100.1972.tb00141.x

Wood, J.A., 2004. Formation of chondritic refractory inclusions: The astrophysical setting. *Geochim Cosmochim Acta* 68, 4007–4021. https://doi.org/10.1016/j.gca.2004.04.003

Xie, Z., Sharp, T.G., 2004. High-pressure phases in shock-induced melt veins of the Umbarger L6 chondrite: Constraints of shock pressure. *Meteorit Planet Sci* 39, 2043–2054. https://doi.org/10.1111/j.1945-5100.2004.tb00095.x

Yang, J., Goldstein, J.I., Scott, E.R.D., 2007. Iron meteorite evidence for early formation and catastrophic disruption of protoplanets. *Nature* 446, 888–891. https://doi.org/10.1038/nature05735

Young, E.D., 2001. The hydrology of carbonaceous chondrite parent bodies and the evolution of planet progenitors. *Philosophical Transactions of the Royal Society of London. Series A: Mathematical, Physical and Engineering Sciences* 359, 2095–2110. https://doi.org/10.1098/rsta.2001.0900

Young, E.D., Zhang, K.K., Schubert, G., 2003. Conditions for pore water convection within carbonaceous chondrite parent bodies – implications for planetesimal size and heat production. *Earth Planet Sci Lett* 213, 249–259. https://doi.org/10.1016/S0012-821X(03)00345-5

Appendices

Appendix 1: Sample list

- Kenna
- Goalpara (x2)
- Novo-Urei
- Almahata Sitta
- MIL090980 (x2)
- MIL090076
- Hajmah

Appendix 2: Raw EPMA data

novo urei	71.8464	56.0794	79.8988	74.7094	70.9374	151.9902	60.0848	101.9613	61.97894	40.3044	80.0582	141.9945	94.1954		
Line	FeO	CaO	TiO2	NiO	MnO	Cr2O3	SiO2	Al2O3	Na2O	MgO	SO3	P2O5	K2O	O	Total
80 G	11.013	4.742	0.108	0.026	0.435	1.263	53.43	1.022	0.141	25.532	0.018	0.02	0.032	0	97.781
81 G	1.733	1.794	0.228	0.004	0.375	0.607	57.421	0.728	0.022	36.729	0.012	0	0.027	0	99.68
82 G	130.764	0.088	0	4.756	0.033	0.395	0.112	0.198	0.021	0.017	0.041	0.456	0.047	0	136.927
83 G	3.9	0.334	0.012	0.007	0.499	0.573	40.761	0.022	0.014	52.799	0.011	0.043	0.032	0	99.007
84 G	8.091	0.378	0	0.014	0.589	0.745	39.995	0.035	0.02	49.114	0	0.039	0.02	0	99.04
85 G	18.936	0.375	0.002	0	0.423	0.661	37.921	0.021	0.016	40.119	0	0.021	0.046	0	98.541
86 G	18.014	0.35	0.036	0.011	0.42	0.559	37.742	0.023	0.025	40.218	0	0.034	0.02	0	97.452
87 G	16.872	0.378	0	0.008	0.478	0.672	37.992	0.02	0.013	41.042	0.03	0.041	0.041	0	97.585
88 G	14.804	0.389	0.004	0	0.395	0.665	38.43	0.02	0.014	42.995	0.022	0	0.021	0	97.759
89 G	13.324	0.169	0.051	0.001	0.484	0.564	37.34	0.057	0.003	47.27	0.012	0.016	0.051	0	99.34
90 G	9.058	0.291	0.012	0.027	0.488	0.554	39.366	0.068	0.009	47.713	0	0.009	0.016	0	97.612
91 G	12.066	0.398	0	0	0.435	0.671	38.912	0.022	0.009	45.421	0.025	0.002	0.028	0	97.989
92 G	13.265	0.376	0.004	0.011	0.458	0.63	38.538	0.022	0.015	44.269	0.049	0.032	0.029	0	97.699
93 G	13.344	0.362	0.036	0.016	0.489	0.658	38.549	0.03	0.023	44.412	0	0.023	0.042	0	97.983
94 G	11.209	0.331	0	0.004	0.479	0.654	38.969	0.034	0.026	46.097	0	0.032	0.033	0	97.869
95 G	131.404	0.042	0.032	0.247	0.009	0.188	2.288	0.108	0.035	4.822	0.033	0.084	0.035	0	139.327
96 G	11.785	0.335	0	0.016	0.444	0.574	38.746	0.017	0.463	45.79	0.028	0.021	0.338	0	98.559
97 G	15.891	0.358	0	0	0.452	0.626	38.016	0.017	0.016	42.259	0	0.009	0.025	0	97.669
98 G	17.544	0.371	0.016	0.002	0.438	0.669	37.629	0.025	0.091	40.6	0.03	0.057	0.12	0	97.591
99 G	19.356	0.329	0	0.096	0.384	0.702	37.321	0.046	0.039	39.254	0	0.025	0.029	0	97.58
100 G	2.046	0.274	0.013	0	0.549	0.589	41.568	0.013	0	54.83	0.003	0.014	0.031	0	99.931
101 G	2.724	0.327	0	0.019	0.547	0.653	41.853	0.05	0	55.662	0.003	0.034	0.044	0	101.917
102 G	2.344	0.29	0	0.004	0.537	0.555	41.525	0.067	0.016	54.423	0.006	0.033	0.012	0	99.811
103 G	2.949	0.198	0.027	0	0.574	0.635	42.442	0.039	0	54.014	0	0.096	0.044	0	101.018
104 G	3.417	0.348	0.029	0.035	0.457	0.36	41.392	0.228	0.022	51.131	0.062	0.069	0.043	0	97.591
105 G	1.947	0.162	0.025	0	0.529	0.418	42.079	0.088	0.016	55.989	0.005	0.018	0.027	0	101.303
106 G	1.518	0.328	0.042	0	0.532	0.467	43.427	0.08	0	53.145	0.021	0.06	0.038	0	99.656
107 G	1.538	0.19	0	0.009	0.495	0.482	41.457	0.066	0.007	54.739	0	0.004	0.037	0	99.023
108 G	3.301	2.926	0.118	0.021	0.664	1.444	54.158	0.776	0.037	33.843	2.494	0	0.041	0	99.823
109 G	6.589	0.2	0.012	0.022	0.472	0.34	38.898	0.059	0.004	51.776	0.024	0	0.029	0	98.426
110 G	128.755	0.039	0	4.845	0.003	0.558	0.121	0.286	0.032	0.049	0.024	0.341	0.072	0	135.124
111 G	19.053	0.332	0	0.006	0.496	0.586	37.77	0.017	0.029	39.824	0.033	0	0.029	0	98.173
112 G	19.291	0.325	0.018	0.036	0.427	0.587	38.041	0.026	0.013	39.916	0.013	0.037	0.033	0	98.763
113 G	18.859	0.315	0	0	0.441	0.612	38.172	0.032	0.003	40.032	0.003	0.025	0.025	0	98.519
114 G	20.717	0.346	0.046	0.034	0.429	0.675	37.896	0.025	0.016	40.536	0.003	0.011	0.019	0	100.753
115 G	10.888	4.719	0.059	0	0.414	1.27	53.459	0.926	0.105	25.867	0	0.005	0.042	0	97.755
116 G	10.661	5.045	0.098	0	0.4	1.191	52.724	1.065	0.128	25.124	0.009	0.016	0.019	0	96.48
117 G	10.534	4.917	0.086	0	0.442	1.247	53.684	0.855	0.09	25.941	0	0.016	0.025	0	97.838
118 G	9.05	5.808	0.103	0	0.387	1.347	53.466	1.112	0.1	25.648	0	0.027	0.045	0	97.092
119 G	2.778	13.982	0.231	0	0.424	1.05	55.962	2.115	0.38	23.463	0.003	0	0.04	0	100.428
120 G	4.759	5.754	0.1	0	0.466	1.133	55.142	0.687	0.076	29.254	0.027	0.038	0.042	0	97.477
121 G	6.879	3.806	0.058	0.002	0.466	1.29	56.038	0.449	0.04	30.723	0.015	0.014	0.032	0	99.813
122 G	10.571	4.675	0.084	0	0.414	1.248	53.663	0.874	0.084	26.064	0.018	0.004	0.028	0	97.725
123 G	10.965	4.68	0.072	0	0.432	1.231	53.248	0.913	0.104	25.905	0.024	0	0.046	0	97.622
124 G	10.979	4.763	0.109	0	0.392	1.133	53.259	0.894	0.102	25.627	0.001	0.021	0.045	0	97.325

kenna	71.8464	56.0794	79.8988	74.7094	70.9374	151.9902	60.0848	101.9613	61.97894	40.3044	80.0582	141.9945	94.1954		
Line	FeO	CaO	TiO2	NiO	MnO	Cr2O3	SiO2	Al2O3	Na2O	MgO	SO3	P2O5	K2O	O	Total
125 G	19.063	0.395	0.026	0.009	0.399	0.701	38.189	0.02	0	40.5	0.018	0.019	0.038	0	99.377
126 G	116.232	0.056	0.005	1.53	0.016	0.118	2.317	0.047	0.016	3.125	0.175	0.385	0.049	0	124.07
127 G	13.723	0.138	0.012	0.12	0.485	0.422	37.167	0.011	0.006	46.275	0.145	0.057	0.026	0	98.587
128 G	8.965	0.154	0	0.06	0.524	0.56	39.954	0.019	0.009	49.493	0.063	0.088	0.046	0	99.935
129 G	13.033	0.373	0	0.03	0.511	0.665	39.545	0.03	0.04	44.017	0.049	0.002	0.072	0	98.368
130 G	18.746	0.393	0	0.006	0.432	0.816	38.414	0.006	0.028	40.96	0	0.028	0.052	0	99.883
131 G	13.484	0.406	0.024	0	0.513	0.781	39.467	0.029	0.017	45.08	0.009	0.007	0.047	0	99.864
132 G	18.14	0.429	0.002	0	0.455	0.74	38.351	0.018	0.029	41.239	0.019	0.053	0.053	0	99.528
133 G	17.306	0.403	0	0.016	0.415	0.64	37.619	0.023	0.084	41.396	0.037	0.057	0.177	0	98.172
134 G	18.675	0.403	0	0	0.414	0.746	38.666	0.009	0.023	40.633	0.016	0.027	0.058	0	99.668
135 G	18.9	0.404	0.016	0	0.417	0.624	38.288	0.013	0.021	40.811	0	0.06	0.035	0	99.589
136 G	5.112	0.252	0.004	0.005	0.543	0.799	41.15	0.02	0.001	52.849	0	0.022	0.025	0	100.782
137 G	16.929	0.447	0.008	0.003	0.182	0.406	43.852	0.039	0.011	25.18	0.115	0.025	0.055	0	87.251
138 G	16.252	0.216	0	0.027	0.499	0.449	37.488	0.008	0.003	42.919	0.021	0.005	0.022	0	97.908
139 G	18.734	0.443	0.02	0	0.412	0.78	38.394	0.041	0.03	40.223	0.052	0.03	0.034	0	99.194
140 G	22.013	0.268	0	0.082	0.39	0.364	35.281	0.016	0.014	38.911	0.066	0.005	0.035	0	97.448
141 G	20.957	0.382	0.042	0	0.446	0.669	36.826	0.008	0.025	38.686	0.05	0.007	0.064	0	98.163
142 G	19.323	0.394	0	0	0.426	0.78	38.26	0	0.019	40.17	0.006	0.023	0.043	0	99.446
143 G	19.106	0.408	0	0.015	0.481	0.744	38.173	0.015	0.007	40.409	0.01	0.021	0.028	0	99.417
144 G	18.073	0.416	0	0.009	0.413	0.689	38.321	0.011	0.023	41.178	0.015	0.048	0.037	0	99.233
145 G	15.91	0.382	0.016	0.018	0.447	0.711	38.78	0.015	0.011	42.909	0.015	0.005	0.035	0	99.253
146 G	13.384	0.28	0.002	0.029	0.502	0.451	39.766	0.02	0.023	46.411	0.01	0	0.027	0	100.904
147 G	9.224	1.051	0	0.021	0.41	0.843	47.416	0.549	0.04	41.202	0.081	0.011	0.028	0	100.877
148 G	82.454	0.045	0	1.807	0.013	0.07	0.457	0.001	0	0.113	0.341	0.72	0.026	0	86.047
149 G	7.493	0.264	0.008	0	0.433	0.706	40.041	0.023	0.012	50.937	0.039	0.022	0.044	0	100.022
150 G	12.321	0.413	0.028	0.01	0.509	0.743	39.535	0.014	0.019	46.342	0.007	0.021	0.051	0	100.015
151 G	16.265	0.417	0	0.014	0.47	0.801	38.775	0.011	0.015	42.842	0	0.023	0.035	0	99.669
152 G	17.954	0.399	0	0	0.45	0.839	38.522	0.01	0.021	41.131	0.001	0.019	0.035	0	99.381
153 G	18.812	0.402	0.016	0.037	0.42	0.787	38.203	0.007	0.022	40.03	0.009	0.03	0.038	0	98.813
154 G	19.097	0.375	0.036	0	0.441	0.686	38.348	0.003	0.02	40.183	0.021	0.012	0.044	0	99.265
155 G	67.496	0.088	0	1.921	0.051	0	1.504	0	0.018	1.273	0.397	0.255	0.059	0	73.063
156 G	18.848	0.408	0.054	0	0.402	0.758	38.211	0.02	0.002	40.785	0	0.019	0.036	0	99.542
157 G	133.211	0.049	0	0.103	0	0.211	0.526	0.754	0.071	0.88	0.048	0	0.087	0	135.941
158 G	87.798	0.008	0	0.024	0.016	0.064	0.459	0	0.023	0.028	0.335	0.065	0.036	0	88.856
159 G	130.591	0.044	0	3.158	0.046	0.082	0.726	0	0.016	0.263	0.036	0.756	0.061	0	135.781
160 G	4.507	0.319	0	0.047	0.615	0.712	41.272	0.02	0.013	53.382	0	0.038	0.019	0	100.946
161 G	7.081	0.433	0	0.004	0.522	0.877	40.845	0.02	0.014	50.789	0.011	0.041	0.023	0	100.658
162 G	35.56	0.113	0	5.96	0.292	0.235	24.579	0.019	0.217	31.495	0.36	0.25	0.306	0	99.388
163 G	8.804	0.404	0.018	0.009	0.506	0.706	40.694	0.009	0.006	49.247	0	0	0.048	0	100.453
164 G	9.946	0.415	0	0	0.416	0.703	40.557	0.021	0.019	48.663	0.049	0.009	0.059	0	100.856
165 G	15.565	0.37	0.012	0.001	0.463	0.793	38.803	0.013	0.004	42.38	0.031	0.034	0.054	0	98.524
166 G	17.352	0.411	0.026	0.026	0.421	0.816	38.688	0.02	0.036	41.426	0.028	0.012	0.068	0	99.331

Goalpara	71.8464	56.0794	79.8988	74.7094	70.9374	151.9902	60.0848	101.9613	61.97894	40.3044	80.0582	141.9945	94.1954		
Line	FeO	CaO	TiO2	NiO	MnO	Cr2O3	SiO2	Al2O3	Na2O	MgO	SO3	P2O5	K2O	O	Total
167 G	1.449	0.216	0.002	0	0.544	0.644	42.056	0.004	0	56.941	0.023	0.007	0.01	0	101.896
168 G	136.357	0.004	0.013	0.299	0.061	0.16	0.076	0.059	0.004	0.088	0	0.157	0.049	0	137.328
169 G	134.951	0.012	0.018	0.29	0.061	0.161	1.941	0	0.016	4.776	0.003	0.144	0.06	0	142.433
170 G	2.415	0.254	0	0.034	0.489	0.864	41.698	0.014	0.003	55.357	0	0.032	0.031	0	101.19
171 G	1.802	0.312	0	0.019	0.624	0.684	41.99	0.017	0.009	56.404	0.017	0.043	0.031	0	101.952
172 G	1.531	0.179	0.023	0	0.415	0.552	41.719	0.03	0	57.337	0	0.04	0.025	0	101.851
173 G	0.899	0.178	0.04	0	0.325	0.277	42.384	0.022	0.009	58.474	0.006	0.02	0.016	0	102.651
174 G	1.256	0.767	0.008	0.005	0.241	0.211	72.615	5.469	0.095	21.459	0.123	0.002	0.061	0	102.313
175 G	0.919	0.227	0.008	0	0.432	0.489	42.737	0.098	0	56.573	0.026	0.034	0.022	0	101.567
176 G	1.498	0.386	0	0.01	0.477	0.59	42.744	0.059	0	54.977	0	0.024	0.006	0	100.77
177 G	1.211	0.234	0.002	0	0.454	0.471	42.783	0.035	0.005	56.699	0.003	0.02	0.032	0	101.949
178 G	1.688	1.43	0.052	0	0.546	0.718	53.821	0.371	0.009	41.836	0.002	0.004	0.048	0	100.525
179 G	9.25	3	0.061	0.055	0.581	2.054	47.379	0.589	0.013	25.019	6.459	0.018	0.044	0	94.522
180 G	8.093	1.598	0.049	0.032	0.562	1.718	46.317	0.789	0.028	37.895	12.386	0	0.043	0	109.511
181 G	1.106	0.178	0.008	0	0.447	0.4	41.999	0	0	57.461	0.021	0.009	0.039	0	101.669
182 G	1.197	0.542	0	0	0.435	0.385	46.4	0.193	0	51.891	0.015	0.009	0.026	0	101.094
183 G	135.221	0.063	0.017	0.638	0	0.28	0.603	0.013	0	0.722	0.292	0.131	0.052	0	138.032
184 G	4.3	0.963	0.004	0.001	0.488	0.971	57.644	0.118	0.013	35.948	0.012	0	0.027	0	100.49
185 G	7.026	1.848	0.016	0.012	0.547	0.949	55.231	0.16	0.031	34.67	0.193	0.022	0.032	0	100.738
186 G	1.369	0.189	0	0.027	0.422	0.634	41.898	0.033	0	56.671	0.014	0.063	0.022	0	101.343
187 G	1.38	0.176	0	0	0.437	0.486	42.318	0.014	0	56.778	0	0.047	0.015	0	101.651
188 G	3.579	3.399	0.027	0.051	0.59	0.971	58.825	0.326	0.039	34.397	0.011	0.004	0.04	0	102.258
189 G	134.675	0.061	0	1.631	0.01	0.189	0.07	0.325	0.01	0.04	0.033	0.167	0.051	0	137.262
190 G	12.598	1.941	0.053	0	0.384	1.038	54.572	0.233	0.033	28.164	0.007	0	0.036	0	99.059
191 G	86.17	0.148	0.013	0.459	0.105	0.632	1.749	0.077	0	1.147	85.439	0.426	0.051	0	176.416
192 G	12.77	2.791	0.02	0.004	0.404	1.071	53.963	0.309	0.049	27.106	0	0	0.025	0	98.512
193 G	12.174	1.917	0.071	0.008	0.386	0.993	54.645	0.249	0.073	28.087	0	0	0.023	0	98.625
194 G	128.151	0.058	0	4.084	0.012	0.167	0.12	0.002	0	0.03	0.023	0.044	0.041	0	132.73
195 G	72.135	0.284	0	0.032	0.022	0.226	9.382	6.88	0.133	6.287	0.34	0.02	0.053	0	95.793
196 G	2.848	0.054	0.059	0.063	0	0.04	76.857	1.026	0.305	0.109	2.157	0.026	0.034	0	83.576
197 G	81.27	0.133	0.01	0.108	0.036	0.184	13.571	0.935	0.116	0.112	0.4	0.308	0.053	0	97.236
198 G	2.242	0.107	0.04	0.021	0.018	0.053	88.861	0.918	0.241	0.473	0.776	0.052	0.025	0	93.827
199 G	10.465	1.938	0.014	0	0.442	1.081	55.165	0.119	0.024	29.835	0	0	0.029	0	99.112
200 G	132.25	0.013	0.028	0.018	0.367	0.099	4.463	0	0.009	0.011	0.007	0.214	0.038	0	137.516
201 G	0.988	0.108	0	0.025	0.205	0.169	41.979	0.002	0	57.894	0.021	0.038	0.025	0	101.455
202 G	133.053	0.014	0	2.854	0.014	0.254	0.627	0	0	0.002	0.017	0.291	0.038	0	137.165
203 G	2.522	0.213	0	0	0.149	0.612	44.312	0.016	0	53.252	3.026	0.036	0.017	0	104.155
204 G	1.757	0.361	0.002	0.017	0.535	0.728	41.418	0.016	0	56.003	0	0.038	0.026	0	100.9
205 G	3.991	0.367	0	0	0.534	0.882	40.978	0.024	0	54.851	0	0.036	0.025	0	101.688
206 G	12.46	1.9	0.047	0.027	0.376	1.133	53.684	0.279	0.034	27.911	0.004	0	0.046	0	97.901
207 G	12.145	1.782	0.016	0.005	0.371	1.012	53.894	0.251	0.039	28.218	0	0.014	0.031	0	97.779
208 G	11.636	1.909	0.016	0.009	0.408	1.14	54	0.237	0.038	28.493	0.006	0	0.024	0	97.916
209 G	9.957	3.56	0.133	0	0.386	1.045	56.224	3.421	0.388	24.654	0.007	0	0.047	0	99.823
210 G	1.871	4.662	0.438	0	0.071	0.105	68.429	14.048	1.363	2.949	0.024	0.022	0.025	0	94.007
211 G	3.177	4.871	0.449	0	0.135	0.427	62.414	10.107	0.639	6.363	0.021	0.004	0.021	0	88.628
212 G	11.862	2.385	0	0.014	0.366	1.031	53.707	0.209	0.027	27.916	0	0.013	0.029	0	97.558
213 G	12.361	2.61	0.045	0	0.426	1.134	53.619	0.256	0.023	27.516	0.004	0.02	0.036	0	98.052
214 G	12.201	2.687	0.004	0	0.441	1.176	53.578	0.285	0.053	27.677	0	0.021	0.036	0	98.16
215 G	129.984	0.005	0.023	0.239	0.09	0.196	3.392	0.023	0.037	8.014	0	0.129	0.053	0	142.185
216 G	2.183	0.29	0.006	0.004	0.487	0.864	40.996	0.018	0.009	55.827	0	0.011	0.002	0	100.697
217 G	136.685	0.005	0.01	0.25	0.034	0.154	0.059	0	0.011	0.032	0.016	0.066	0.052	0	137.373

MIL 090980	71.8464	56.0794	79.8988	74.7094	70.9374	151.9902	60.0848	101.9613	61.97894	40.3044	80.0582	141.9945	94.1954		
Line	FeO	CaO	TiO2	NiO	MnO	Cr2O3	SiO2	Al2O3	Na2O	MgO	SO3	P2O5	K2O	O	Total
218 G	20.117	0.334	0.062	0.018	0.43	0.58	38.329	0.006	0.023	39.943	0.007	0.039	0.045	0	99.933
219 G	20.025	0.318	0.048	0.052	0.4	0.586	38.432	0.013	0.023	40.265	0	0	0.044	0	100.206
220 G	26.971	0.294	0	0.416	0.424	0.505	34.195	0.018	0	35.675	0.161	0.033	0.017	0	98.71
221 G	66.803	0.084	0	2.852	0.052	0.088	4.453	0.087	0.019	2.79	1.737	0.148	0.018	0	79.131
222 G	15.587	0.284	0.038	0.039	0.446	0.542	39.616	0.053	0.019	43.998	0	0	0.032	0	100.653
223 G	16.148	0.3	0	0.325	0.438	0.466	36.661	0.023	0.002	44.214	0.14	0.007	0.016	0	98.74
224 G	7.766	0.287	0.012	0.002	0.51	0.5	40.875	0.05	0.011	50.554	0.012	0.018	0.035	0	100.632
225 G	5.49	0.282	0.037	0.028	0.431	0.462	41.572	0.037	0.004	53.036	0.038	0.023	0.02	0	101.461
226 G	67.28	0.11	0	3.651	0.063	0.116	2.525	0.101	0.07	0.08	1.678	0.626	0.06	0	76.362
227 G	8.652	0.27	0.014	0.302	0.008	0.064	0.93	0.054	0.04	0.172	1.12	0.221	0.046	0	11.892
228 G	5.499	0.224	0	0.091	0	0.271	2.419	0.329	0.036	0	0.414	0.507	0.043	0	9.833
229 G	18.99	0.58	0	0.33	0.046	0.229	28.52	0.963	0.115	0.071	0.78	0.192	0.079	0	50.896
230 G	5.116	0.695	0.089	0.082	0.455	1.057	56.399	0.554	0.041	34.374	0.082	0.036	0.037	0	99.017
231 G	12.556	4.14	0.063	0.056	0.41	1.068	53.532	0.956	0.127	26.32	0.019	0	0.025	0	99.272
232 G	11.544	4.159	0.02	0.007	0.432	1.111	54.194	1.006	0.153	26.491	0.025	0.023	0.02	0	99.186
233 G	11.789	4.176	0.059	0.012	0.479	1.11	54.266	0.956	0.14	26.492	0.007	0.007	0.042	0	99.537
234 G	11.541	4.187	0.059	0.032	0.339	1.111	54.386	0.955	0.123	26.517	0.01	0	0.042	0	99.302
235 G	11.303	5.036	0.051	0.011	0.415	1.146	53.829	1.168	0.094	26.492	0	0.034	0.039	0	99.619
236 G	2.402	1.618	0.058	0.029	0.402	0.668	57.816	0.642	0.046	35.157	0.047	0.011	0.032	0	98.928
237 G	13.967	4.077	0.049	0.097	0.406	1.176	52.627	0.959	0.089	25.174	0.091	0.053	0.031	0	98.795
238 G	12.124	4.199	0.078	0	0.412	1.106	53.989	0.966	0.132	26.113	0.013	0.007	0.044	0	99.183
239 G	12.488	4.178	0.088	0.013	0.4	1.084	53.538	0.963	0.11	25.967	0.049	0	0.03	0	98.906
240 G	67.366	0.544	0	3.427	0.082	0.23	9.237	0.09	0.046	3.583	1.413	0.052	0.03	0	86.099
241 G	1.468	0.869	0.038	0.034	0.242	0.438	58.385	0.433	0.004	37.493	0.029	0	0.025	0	99.458
242 G	1.874	14.148	0.175	0.035	0.347	0.84	54.803	1.529	0.12	26.514	0.027	0.005	0.038	0	100.453
243 G	2.502	0.876	0.096	0.019	0.329	0.717	57.097	0.569	0.085	36.742	0.056	0	0.037	0	99.124
244 G	7.502	0.794	0.055	0.386	0.08	0.112	48.862	4.688	0.982	15.789	0.804	0.027	0.185	0	80.265
245 G	1.872	0.656	0.113	0.033	0.283	0.598	58.306	1.162	0.168	35.102	0.069	0.027	0.076	0	98.466
246 G	11.431	4.221	0.07	0.033	0.441	1.078	54.598	1.047	0.122	26.694	0	0.013	0.02	0	99.767
247 G	77.006	0.057	0.288	0.268	0.397	5.491	1.073	0.103	0.095	0.029	83.402	0.034	0.072	0	168.313
248 G	61.33	0.092	0.13	1.496	0.069	2.693	8.07	0.16	0.145	0.045	5.684	0.834	0.102	0	80.85
249 G	60.819	0.051	0.026	1.976	0.047	0.811	6.573	0.11	0.073	0.208	5.508	0.935	0.066	0	77.202
250 G	2.916	6.188	0.148	0.052	0.336	0.451	57.46	1.26	0.221	30.987	0.119	0	0.034	0	100.174
251 G	80.778	0.027	0.323	0.277	0.491	5.814	0.02	0	0	0.013	93.759	0	0.007	0	181.508
252 G	10.576	3.28	0.037	0.017	0.42	0.978	55.302	0.66	0.079	28.429	0.03	0.018	0.033	0	99.86
253 G	5.084	14.199	0.209	0.041	0.468	1.214	52.923	2.015	0.166	22.753	0.058	0.025	0.036	0	99.189
254 G	14.123	1.886	0.03	0.303	0.381	0.872	52.4	0.346	0.025	28.904	0.205	0.075	0.012	0	99.563
255 G	69.707	0.07	0.005	2.774	0.023	0.081	2.439	0.028	0.04	0.075	1.011	0.444	0.062	0	76.758
256 G	82.184	0.038	0.186	0.193	0.466	3.933	0.024	0	0.005	0.015	92.812	0.013	0.046	0	179.916
257 G	65.373	0.085	0	2.486	0.079	0.142	5.902	0.067	0	7.268	1.551	0.102	0.046	0	83.101
258 G	17.958	0.336	0.028	0.006	0.43	0.519	38.832	0.011	0.004	41.911	0.01	0.03	0.014	0	100.089
259 G	18.59	0.38	0.008	0.035	0.413	0.635	38.768	0.028	0	40.968	0.052	0.004	0.016	0	99.897
260 G	37.195	1.155	0.046	1.106	0.295	6.605	27.188	0.642	0.062	30.171	0.17	0.034	0.047	0	104.715
261 G	21.218	0.167	0.009	0.246	0.073	0.315	3.624	0.161	0.08	0.147	13.099	0.401	0.053	0	39.594
262 G	17.369	0.335	0	0.019	0.399	0.553	38.872	0.009	0.008	42.265	0	0.039	0.047	0	99.915
263 G	19.042	0.321	0.002	0.006	0.391	0.603	38.886	0.02	0.011	41.112	0.006	0.034	0.047	0	100.479
264 G	68.757	0.084	0.024	2.582	0.057	0.626	6.038	0.204	0.046	2.395	1.393	0.088	0.041	0	82.333
265 G	14.817	0.33	0.079	0.011	0.47	0.448	39.5	0.032	0.015	44.883	0	0	0.024	0	100.61
266 G	16.341	0.306	0	0.011	0.43	0.59	38.947	0.065	0.01	43.241	0.018	0.023	0.023	0	100.005
267 G	95.192	0.065	0.056	3.779	0.067	1.476	0.095	0	0	0.032	73.098	0.021	0.01	0	173.892
268 G	0.637	0.878	0.313	0	0.026	0.029	74.077	14.665	3.179	0.437	0.102	0.054	0.492	0	94.889
269 G	3.792	3.977	0.15	0.03	0.468	0.636	57.15	1.346	0.158	32.219	0.062	0.022	0.068	0	100.079
270 G	3.951	18.359	0.884	0.014	0.433	1.991	50.175	6.003	0.29	17.617	0	0.007	0.019	0	99.743

MIL 090076	71.8464	56.0794	79.8988	74.7094	70.9374	151.9902	60.0848	101.9613	61.97894	40.3044	80.0582	141.9945	94.1954		
Line	FeO	CaO	TiO2	NiO	MnO	Cr2O3	SiO2	Al2O3	Na2O	MgO	SO3	P2O5	K2O	O	Total
271 G	7.458	5.059	0.054	0	0.467	1.228	55.314	0.17	0.024	29.366	0.034	0	0.018	0	99.192
272 G	7.95	2.96	0.181	0	0.354	0.993	58.496	4.758	0.881	23.532	0.992	0	0.033	0	101.13
273 G	11.232	5.341	0.076	0.057	0.435	1.267	54.305	0.903	0.076	25.841	0.033	0.004	0.029	0	99.598
274 G	52.655	2.857	0.021	0.737	0.19	0.844	25.798	0.989	0.078	11.938	35.215	0.027	0.035	0	131.383
275 G	19.582	0.342	0	0.018	0.422	0.585	38.45	0.024	0.002	40.564	0.03	0.005	0.043	0	100.068
276 G	11.082	5.272	0.088	0	0.442	1.338	53.93	0.97	0.11	25.754	0	0.018	0.037	0	99.041
277 G	78.331	0.032	0.108	0.13	0.539	8.617	0.022	0	0	0.045	95.431	0	0.025	0	183.28
278 G	77.497	0.037	0.061	0.2	0.542	8.355	0.027	0	0.026	0.048	93.57	0	0.053	0	180.417
279 G	76.382	0.057	0.143	0.163	0.58	8.467	0.078	0	0	0.038	94.909	0.025	0.047	0	180.889
280 G	7.394	2.474	0.054	0.014	0.414	1.05	55.63	0.733	0.011	31.173	0.065	0.004	0.033	0	99.048
281 G	9.341	1.705	0.031	0.043	0.351	1.001	55.251	0.109	0.018	30.649	0.015	0.016	0.026	0	98.555
282 G	4.095	9.776	0.111	0.028	0.517	1.092	55.774	0.347	0.053	28.212	0.004	0.007	0.015	0	100.031
283 G	3.855	6.391	0.042	0.029	0.497	1.075	56.003	0.123	0.024	29.24	0.003	0.005	0.025	0	97.313
284 G	8.301	2.453	0.051	0	0.381	1.129	55.238	0.142	0.026	29.457	0	0.011	0.034	0	97.224
285 G	7.204	2.75	0.041	0	0.46	1.145	56	0.328	0.035	31.336	0.011	0.009	0.04	0	99.36
286 G	0.761	4.638	0.216	0	0.189	0.262	66.981	13.403	1.722	8.608	0.02	0.002	0.058	0	96.858
287 G	5.812	4.986	0.048	0	0.482	1.105	55.849	0.127	0.031	32.21	0	0.022	0.056	0	100.727
288 G	10.486	5.376	0.064	0	0.423	1.298	53.833	0.853	0.083	25.962	0.013	0.029	0.018	0	98.436
289 G	10.54	6.524	0.094	0.007	0.439	0.986	53.653	0.906	0.115	24.432	0.033	0.011	0.017	0	97.758
290 G	10.983	5.482	0.086	0.002	0.432	1.284	53.824	0.861	0.088	25.649	0.037	0.007	0.028	0	98.762
291 G	10.389	6.582	0.15	0	0.433	1.2	53.106	0.932	0.105	26.132	0.012	0.014	0.024	0	99.079
292 G	11.117	5.298	0.108	0	0.361	1.327	53.697	0.867	0.088	25.908	0.039	0	0.028	0	98.837
293 G	5.322	5.466	0.025	0.018	0.489	1.115	55.571	0.157	0.033	30.723	0.018	0.009	0.025	0	98.97
294 G	6.822	5.345	0.085	0	0.501	1.271	54.911	0.425	0.035	29.017	0.03	0.013	0.023	0	98.478
295 G	11.298	5.281	0.082	0.048	0.41	1.254	53.628	0.879	0.086	25.842	0.034	0	0.02	0	98.86
296 G	11.382	6.859	0.117	0.022	0.384	1.265	53.351	1.218	0.096	24.855	0.025	0.02	0.037	0	99.629
297 G	5.425	4.836	0.046	0.012	0.441	1.085	56.133	0.113	0.029	30.81	0.164	0.007	0.033	0	99.135
298 G	11.051	5.368	0.102	0.044	0.426	1.286	53.725	0.867	0.065	25.512	0.028	0.021	0.02	0	98.517
299 G	30.006	0.865	0	0.36	0.071	0.56	58.397	2.504	0.072	5.171	30.517	0.025	0.032	0	128.581
300 G	2.24	0.673	0.052	0.121	0.037	0.037	92.941	1.389	0.092	0.054	0.085	0.043	0.035	0	97.801
301 G	16.925	0.397	0.018	0.005	0.431	0.724	38.616	0.016	0.015	42.282	0	0.012	0.02	0	99.461
302 G	19.441	0.367	0	0.013	0.43	0.736	38.132	0.015	0.015	40.277	0.071	0.005	0.028	0	99.531
303 G	11.079	5.36	0.07	0	0.389	1.343	52.965	0.858	0.081	25.665	0.03	0.012	0.026	0	97.88
304 G	8.603	5.065	0.027	0	0.471	1.251	54.108	0.162	0.054	27.981	0.159	0.016	0.038	0	97.932
305 G	11.137	5.224	0.078	0.003	0.388	1.258	53.357	0.969	0.107	25.514	0.016	0	0.024	0	98.076
306 G	11.176	5.21	0.084	0	0.404	1.31	52.956	0.86	0.098	25.597	0.069	0	0.049	0	97.813
307 G	7.936	4.461	0	0.025	0.468	1.241	54.477	0.164	0.04	29.135	0.045	0.005	0.032	0	98.029
308 G	19.704	0.29	0.034	0.025	0.416	0.638	37.61	0.029	0.013	40.119	0.025	0.028	0.027	0	98.957
309 G	19.535	0.427	0.008	0.021	0.455	0.707	37.7	0.012	0.013	40.057	0.075	0.034	0.034	0	99.078
310 G	19.635	0.292	0.014	0.025	0.452	0.602	37.5	0.019	0.006	40.08	0.087	0.028	0.044	0	98.784
311 G	19.672	0.33	0	0.018	0.437	0.602	37.769	0.002	0	40.359	0.033	0.018	0.027	0	99.267
312 G	19.693	0.398	0.026	0.005	0.423	0.727	38.218	0.005	0	39.904	0.019	0	0.048	0	99.467
313 G	10.574	5.371	0.084	0.011	0.425	1.23	54.148	0.704	0.08	26.511	0.039	0.018	0.024	0	99.219
314 G	114.698	0.046	0	15.789	0.017	0.053	0.052	0	0	0.078	0.392	7.211	0.055	0	138.392
315 G	122.987	0.122	0.01	2.83	0	0.18	0.077	0	0.001	0.012	0.058	0.025	0.028	0	126.331
316 G	11.093	5.718	0.172	0.046	0.465	1.395	53.052	1.564	0.139	24.253	0	0.02	0.017	0	97.933
317 G	11.219	5.5	0.088	0	0.459	1.238	54.175	1.022	0.148	25.401	0.001	0	0.037	0	99.288
318 G	9.355	2.669	0.057	0.02	0.475	1.257	55.573	0.212	0.01	29.644	0	0	0.016	0	99.289
319 G	8.877	5.169	0.031	0	0.46	1.268	55.219	0.244	0.044	28.019	0.018	0	0.037	0	99.387
320 G	8.042	4.613	0.023	0.043	0.455	1.213	55.572	0.163	0.031	29.106	0.003	0.022	0.02	0	99.304
321 G	9.262	5.13	0.368	0.021	0.407	1.336	58.426	3.874	1.083	23.055	0.07	0.021	0.025	0	103.079
322 G	8.215	5.432	0.068	0	0.429	1.325	55.037	0.248	0.037	28.249	0.075	0.005	0.023	0	99.143
323 G	9.899	2.68	0.004	0.073	0.386	1.244	55.443	0.191	0.008	30.028	0.03	0.009	0.039	0	100.032
324 G	6.939	5.184	0.012	0.032	0.476	1.218	56.173	0.141	0.038	29.877	0.073	0	0.02	0	100.184
325 G	11.228	5.206	0.082	0.008	0.453	1.302	54.094	0.953	0.1	25.856	0.043	0.027	0.031	0	99.382
326 G	79.438	0.107	0	1.255	0.005	0.263	1.352	0.011	0.057	0.518	0.655	0.14	0.068	0	83.868
327 G	69.493	0.156	0	1.244	0.01	0.095	1.208	0	0.067	0.81	2.168	0	0.044	0	75.296
328 G	11.19	5.412	0.084	0.026	0.436	1.322	54.02	0.921	0.093	25.805	0.013	0	0.036	0	99.36
329 G	11.364	5.371	0.084	0	0.419	1.406	54.315	0.932	0.117	25.712	0.092	0.002	0.024	0	99.839
330 G	11.106	5.405	0.065	0.012	0.406	1.328	54.08	0.97	0.112	25.854	0.067	0.012	0.037	0	99.457
331 G	4.697	9.965	0.763	0.012	0.315	1.329	58.107	8.985	1.696	10.659	0.048	0.016	0.038	0	96.632
332 G	9.022	5.259	0.021	0	0.455	1.242	55.553	0.19	0.028	27.987	0.165	0	0.025	0	99.945
333 G	2.55	5.963	0.036	0	0.194	0.622	66.732	0.708	5.935	9.464	0.163	0.014	0.123	0	92.506
334 G	11.439	5.257	0.061	0.043	0.423	1.359	54.276	0.9	0.089	25.855	0.003	0.011	0.032	0	99.749
335 G	19.608	0.354	0	0.017	0.4	0.598	38.319	0.016	0.022	40.278	0.417	0.048	0.028	0	100.106